

The Chemistry of Interstellar OH⁺, H₂O⁺, and H₃O⁺: Inferring the Cosmic Ray Ionization Rates from Observations of Molecular Ions

David Hollenbach¹, M. J. Kaufman², D. Neufeld³, M. Wolfire⁴, and J. R. Goicoechea⁵

¹*SETI Institute, Mountain View, CA, 94043-5203*

²*Department of Physics & Astronomy, San Jose State University, San Jose, CA 95192-0106*

³*Department of Physics and Astronomy, The Johns Hopkins University, Baltimore, MD, 21218*

⁴*Department of Astronomy, University of Maryland, College Park, MD, 20742*

⁵*Departamento de Astrofísica, Centro de Astrobiología (CSIC-INTA), 28850, Madrid, Spain*

ABSTRACT

We model the production of OH⁺, H₂O⁺, and H₃O⁺ in interstellar clouds, using a steady state photodissociation region code that treats the freeze-out of gas species, grain surface chemistry, and desorption of ices from grains. The code includes PAHs, which have important effects on the chemistry. All three ions generally have two peaks in abundance as a function of depth into the cloud, one at $A_V \lesssim 1$ and one at $A_V \sim 3 - 8$, the exact values depending on the ratio of incident ultraviolet flux to gas density. For relatively low values of the incident far ultraviolet flux on the cloud ($\chi \lesssim 1000$; $\chi = 1 =$ local interstellar value), the columns of OH⁺ and H₂O⁺ scale roughly as the cosmic ray primary ionization rate ζ_{crp} divided by the hydrogen nucleus density n . The H₃O⁺ column is dominated by the second peak, and we show that if PAHs are present, $N(\text{H}_3\text{O}^+) \sim 4 \times 10^{13} \text{ cm}^{-2}$ independent of ζ_{crp} or n . If there are no PAHs or very small grains at the second peak, $N(\text{H}_3\text{O}^+)$ can attain such columns only if low ionization potential metals are heavily depleted. We also model diffuse and translucent clouds in the interstellar medium, and show how observations of $N(\text{OH}^+)/N(\text{H})$ and $N(\text{OH}^+)/N(\text{H}_2\text{O}^+)$ can be used to estimate ζ_{crp}/n , χ/n and A_V in them. We compare our models to *Herschel* observations of these two ions, and estimate $\zeta_{crp} \sim 4 - 6 \times 10^{-16} (n/100 \text{ cm}^{-3}) \text{ s}^{-1}$ and $\chi/n = 0.03 \text{ cm}^3$ for diffuse foreground clouds towards W49N.

Subject headings: astrochemistry, ISM: cosmic rays, ISM: molecules, ISM: clouds, galaxies: ISM, submillimeter

1. INTRODUCTION

The OH⁺, H₂O⁺, and H₃O⁺ ions form the backbone of interstellar chemistry and are important probes of the cosmic ray ionization rates in diffuse clouds, on the surfaces ($A_V < 1$) of molecular

clouds, and (with less reliability as we will discuss in this paper) in the interiors ($A_V \sim 4 - 8$) of molecular clouds. They are the backbone of chemistry because once H_2 forms, cosmic ray ionization of H or H_2 leads to the formation of these ions, and H_3O^+ recombination with electrons leads to OH and H_2O . Reaction of OH with C or C^+ leads to CO.¹ Once these basic molecules are formed, many of the other polyatomic and rare species follow.

The pathway of cosmic ray ionization of hydrogen to these molecular ions follows two routes (see Figure 1). In gas with significant H atoms the ionization of H leads to H^+ that then proceeds via a series of reactions (see Figure 1 top) to OH^+ , H_2O^+ and H_3O^+ ions. We note that the charge exchange of O with H^+ is slightly endothermic, so the reaction rate is proportional to $\exp(-230 \text{ K}/T)$; this means that this reaction slows down at cooler temperatures, and a greater fraction of the cosmic ray ionizations of H are followed by recombination of H^+ with neutral or negatively charged polycyclic aromatic hydrocarbons (PAHs or PAH^-) or electrons rather than proceeding to form O^+ and then OH^+ . It is this atomic route to OH^+ which is primarily important in diffuse clouds and in the $A_V \lesssim 2$ surfaces of molecular clouds. A second route dominates deeper in the opaque interiors of molecular clouds. Here the ionization of H_2 leads to H_2^+ , which then proceeds via a series of reactions (see Figure 1 bottom) to OH^+ , H_2O^+ and H_3O^+ . A key competitor here to the formation of OH^+ is the dissociative recombination of H_3^+ with electrons, which has a high rate coefficient compared to the reaction of H_3^+ with O. In addition, the reaction of H_3^+ with CO dominates that with O when the CO abundance exceeds that of O. Therefore, low electron abundances and high O abundances are needed to ensure that a large fraction of cosmic ray ionizations of H_2 eventually produces OH^+ .

As we shall show in this paper, these two routes lead generally to two peaks in the abundances of OH^+ , H_2O^+ , and H_3O^+ as a function of depth or A_V into a cloud. The first peak (at $A_V \sim 0.01 - 1$ depending on the ratio of the incident FUV flux to the gas density) occurs in atomic gas where the cosmic ray ionization of H begins the chemical chain.² The second peak (at $A_V \sim 3 - 8$, again dependent on the FUV flux/gas density ratio) occurs in molecular gas where the cosmic ray ionization of H_2 begins the chemical chain. Deeper in the cloud the gas phase oxygen freezes out as water ice on grain surfaces (e.g., Hollenbach et al 2009, hereafter H09), and the gas phase abundances of the three ions drop. Whereas significant columns of OH^+ and H_2O^+ are produced in the first peak, most of the H_3O^+ column arises in the second peak.

In warm ($T > 300 \text{ K}$) neutral gas with significant abundances of H_2 there are other dominant pathways to form OH^+ , H_2O^+ , and H_3O^+ ions than the two paths initiated by cosmic rays and shown in Figure 1. One of the goals of this paper is to show under what conditions (e.g., FUV flux, gas density, cosmic ray ionization rate) cosmic rays initiate the formation of the OH^+ , H_2O^+ , and H_3O^+ ions, and under what conditions other chemical routes dominate.

¹CO also has another route initiated by the production of the CH^+ ion, which we do not discuss in detail in this paper although it is included in our models.

²FUV is defined as photons in the range $6\text{eV} < h\nu < 13.6 \text{ eV}$.

If cosmic rays dominate, then the observed columns of OH^+ , H_2O^+ , and H_3O^+ serve as a probe of the cosmic ray ionization rate. The major goal of this paper is to show how these columns depend on the cosmic ray ionization rate, the gas density, the FUV flux, the total column or optical extinction A_{V_t} through the cloud, and the molecular hydrogen abundance. Comparison with our models allow the cosmic ray ionization rate to be estimated from these ion columns and the atomic H column.

Our method of estimating cosmic ray ionization rates from the abundance of eventual products of this ionization dates back to the 1970's, when Black & Dalgarno (1973) pointed out the sensitivity of the OH and HD abundances to cosmic ray ionization rates. A later comprehensive paper by van Dishoeck & Black (1986) showed how the abundance of OH in diffuse or translucent clouds could be used to estimate the cosmic ray rate. One advantage of using OH^+ or H_2O^+ to probe cosmic ray ionization rates over using OH is that OH is produced after a series of reactions following the formation of OH^+ (see Figure 1). This makes the inference of cosmic ray ionization rate dependent on knowledge of the rate coefficients of these additional reactions.

Recent observations strongly motivate the theoretical study of the OH^+ , H_2O^+ , and H_3O^+ molecular ions. Prior to 2010, the only observations of these three ions within the interstellar medium³ consisted of a few detections of H_3O^+ in rich interstellar sources of submillimeter line emission and absorption (Wootten et al 1991; Phillips, van Dishoeck & Keene 1992, hereafter PvDK92; Goicoechea & Cernicharo 2001; van der Tak et al 2006). Thanks largely to absorption-line spectroscopy with the HIFI instrument on the *Herschel Space Observatory*, together with additional ground-based detections of OH^+ obtained with the APEX telescope (submillimeter rotational transition) and the ESO Paranal observatory (near-UV electronic transition), the observational picture has improved radically over the past two years. All three molecular ions have now been detected in both the diffuse and dense Galactic interstellar medium (Gerin et al. 2010; Ossenkopf et al. 2010; Wyrowski et al. 2010; Neufeld et al. 2010; Schilke et al. 2010; Gupta et al. 2010; Bruderer et al. 2010; Benz et al. 2010; Krelowski, Beletsky, & Galazutdinov 2010) and in external galaxies (van der Tak et al 2008; Weiss et al. 2010; van der Werf et al. 2010; González-Alfonso et al. 2010; Aalto et al 2011). The most reliable column density determinations are obtained for foreground molecular clouds lying along the sight-lines to bright submillimeter continuum sources in the Galactic disk. Here, the absorbing material typically covers a wide range of line-of-sight velocities, arising in widely distributed material along the sight-line. The total inferred column densities of the ions lie in the range $\text{few} \times 10^{13} - \text{few} \times 10^{14} \text{ cm}^{-2}$, the largest values being attained for OH^+ and the smallest for H_3O^+ (Gerin et al. 2010; Neufeld et al. 2010).

In their study of OH^+ and H_2O^+ absorption along the sight-line to the luminous star-forming region W49N, Neufeld et al. (2010, hereafter N10) measured an average $\text{OH}^+/\text{H}_2\text{O}^+$ abundance ratio of ~ 10 , with variations over the range $\sim 3 - 15$. These observed ratios are considerably larger

³Note, however, that the H_2O^+ ion has long been observed in cometary comae (e.g. Wehinger et al. 1974), where it is produced by the photoionization of water by solar ultraviolet radiation.

than the value ~ 1 expected in fully molecular gas.⁴ By means of a simple analytical treatment of the chemistry of OH^+ and H_2O^+ , confirmed by more detailed pure gas-phase models performed using the Meudon PDR model (Le Petit et al 2006; Goicoechea & Le Bourlot 2007), N10 concluded that the molecular fraction in the absorbing material lies in the range 2 – 8 %. This conclusion was supported by the observed distribution in velocity space of the OH^+ and H_2O^+ absorption, which proved similar to that of the atomic gas probed by 21 cm absorption studies, and quite dissimilar from that of the molecular gas traced by HF or CH absorption. The analytic treatment introduced by N10 also allowed the cosmic ray ionization rate to be inferred from the abundances of OH^+ and H_2O^+ relative to atomic hydrogen. The resulting estimate of the cosmic ray ionization rate in the range $\zeta_{crp} = 0.6 - 2.4 \times 10^{-16} \text{ s}^{-1}$ (primary ionization rate per H atom) was broadly consistent with earlier values inferred quite independently from observations of the H_3^+ molecular ion toward different sight lines (Indriolo et al. 2007). One of the goals of the present study is to refine the N10 analytic treatment of diffuse cloud chemistry through detailed modeling, as an aid to interpreting the growing body of observational data now available.

This paper is organized as follows. In §2 we describe the chemical/thermal model of both an opaque molecular cloud illuminated by FUV radiation, or a diffuse cloud illuminated by the interstellar radiation field. In §3 we show the model columns and column ratios of OH^+ , H_2O^+ , and H_3O^+ as functions of the cloud gas density n , the incident FUV flux χ (in units of the local average interstellar field, see below), and the primary cosmic ray ionization rate ζ_{crp} per H atom for the case of opaque molecular clouds. We also show the same results for diffuse clouds, but with the total column or A_{Vt} through the cloud as an additional parameter. In §4 we compare our model results with previous H_3O^+ observations and recent OH^+ , H_2O^+ , and H_3O^+ observations by *Herschel*, and show how observations compared to models can constrain the cosmic ray ionization rates. We summarize our results in §5. Appendix A presents tables of key reaction rate coefficients and adopted abundances and grain parameters. Appendix B includes analytic expressions that explain the variation of OH^+ with A_V over the first peak, and the variation of H_3O^+ with A_V over the second peak. Appendix C assesses the sensitivity of our results to certain chemical rate coefficients, the gas phase abundance of elemental oxygen and low ionization potential metals, and the freeze-out of species.

⁴In fully molecular gas the formation rates of these ions per unit volume are equal because every OH^+ formation is followed by H_2O^+ formation and the destruction rate per ion is nearly the same (due to reaction with H_2), leading to similar abundances for both ions (N10).

2. THE CHEMICAL AND THERMAL MODEL OF A CLOUD

2.1. Summary of Prior PDR Model and Modifications

The numerical code we have developed to model the chemical and thermal structure of an opaque cloud externally illuminated by FUV flux is based on our previous PDR model described in H09. This 1D code models a constant density n (the hydrogen nucleus density) slab of gas, illuminated from one side by an FUV flux of $2.7 \times 10^{-3} \chi$ erg cm⁻² s⁻¹ incident perpendicular to the slab. The unitless parameter χ is defined above in such a way that $\chi \sim 1$ corresponds to the average local interstellar radiation field in the FUV band (Draine 1978).⁵ The code calculates the steady state chemical abundances and the gas temperature from thermal balance as a function of depth into the cloud. It incorporates 63 chemical species, ~ 300 chemical reactions, and a large number of heating mechanisms and cooling processes. The chemical reactions include FUV photoionization and photodissociation; cosmic ray ionization; neutral-neutral, ion-neutral, and electronic recombination reactions. H₂ self-shielding is included as described in H09, and CO self-shielding and the partial shielding of CO by H₂ is included as described in Visser et al (2009). The code includes the photodissociation of molecules by “secondary” FUV photons produced (ultimately) by cosmic rays (Prasad & Tarafdar 1983). We also include reactions with charged dust grains and PAHs; and the formation of H₂, OH, H₂O, CH, CH₂, CH₃, and CH₄ on grain surfaces. The code treats the freezing of all condensable species to grain surfaces and three desorption processes: thermal desorption, photodesorption, and cosmic ray desorption. The only significant difference in the desorption code used here versus the H09 code is the inclusion of the new (higher by factor ~ 3) rate of photodesorption of CO (Oberg et al 2009). The code does not include photodesorption by the secondary FUV photons; this process is negligible at the peaks in the OH⁺, H₂O⁺, and H₃O⁺ abundances. The code has been used to model regions which lie at hydrogen nucleus column densities $N \lesssim 4 \times 10^{22}$ cm⁻² (or $A_V \lesssim 20$) from the surface of a cloud. Therefore, it applies not only to the photodissociated surface region, where gas phase hydrogen and oxygen are nearly entirely atomic and where gas phase carbon is mostly C⁺, but also to regions deeper into the molecular cloud where hydrogen is in H₂ molecules and carbon is in CO molecules. Even in these molecular regions, the attenuated FUV field can play a significant role in photodissociating H₂O and O₂, in photodesorbing species adsorbed on grain surfaces, and in heating the gas. However, the code is now sufficiently general that it finds the steady state solutions for abundances and temperature in any region of a molecular cloud, even where FUV is insignificant.

We emphasize that we present a steady-state model of chemical abundances as a function of depth into the cloud. The chemical timescales can be quite long, which might suggest that time dependent models are more appropriate. For example, the timescale to convert atomic H gas to fully

⁵ Note that $\chi = 1$ corresponds to $G_0 = 1.7$ in the Tielens & Hollenbach (1985) units based on the Habing (1968) local interstellar radiation field. The shape of the FUV spectrum for $\chi > 1$ is implicitly assumed to mimic that of the Draine field, which is approximately that of a $T_{eff} \sim 30,000$ K star.

molecular H_2 gas is $t_{\text{H}_2} \sim 10^9/n$ years, where n is the hydrogen nucleus density in units of cm^{-3} . However, as we show below, the OH^+ and H_2O^+ ions peak in abundance when $x(\text{H}_2) \sim 0.03 - 0.1$, which occur typically at $A_V \sim 0.1$. [Note, abundances in this paper are defined relative to hydrogen nuclei, so that $x(\text{H}_2) \equiv n(\text{H}_2)/n$ and $n \simeq n(\text{H}) + 2n(\text{H}_2)$]. Therefore, the timescales for even diffuse clouds of density $n \sim 100 \text{ cm}^{-3}$ to reach these abundances are less than $\sim 10^6$ years, which is shorter than the typical lifetime of a diffuse cloud (Wolfire et al 2003). Steady state solutions therefore generally apply, at least for computing the columns of these ions. The steady state models may somewhat underestimate the ion columns for low density diffuse clouds with $A_V > 0.1$, since the steady state solutions can lead to lower abundances of these two ions than time dependent solutions in the high A_V regions. This arises because the steady state abundances of H_2 are higher than time dependent models which start with fully atomic gas. Higher H_2 abundances lead to more destruction of OH^+ and H_2O^+ in the high A_V regions where H_2 and not electrons dominate the destruction of these ions. Liszt (2007) provides a detailed analysis of the time dependent formation of H_2 and OH^+ as a function of A_V in diffuse clouds with initial atomic conditions.

We also emphasize that our model does not include turbulent dissipation and heating of small pockets of gas along the line of sight (e.g., Godard, Falgarone, & Pineau des Forets 2009 and references therein). We do, however, run PDR models with small fractions of the line of sight having either enhanced temperature or enhanced rates of ion-neutral drift to test the possible effects of turbulence, and find the effects on OH^+ , H_2O^+ , H_3O^+ column densities are likely small.

For simplicity we assume constant H nucleus density n in our models. At low A_V and low $x(\text{H}_2) < 0.1$, where much of the OH^+ and H_2O^+ columns often arise, the temperature is quite constant so that constant density implies constant thermal pressure. If thermal pressure (and not turbulence) dominates deeper into a high A_V cloud, then the density will rise as one moves from its warmer PDR surface to its CO-cooled molecular interior. In addition, self gravity can raise the density of the interior regions at higher A_V . Still another effect is the transition of atomic hydrogen to molecular hydrogen which can raise n by a factor of 2 if thermal pressure is conserved. We ignore the possible rise in density, which mainly affects the second peaks of the ions deep ($A_V > 4$) in the cloud. If such a density enhancement occurs, it tends to depress the abundances of OH^+ and H_2O^+ in the second peaks, but the abundance of H_3O^+ at the second peak is not sensitive to hydrogen density if PAHs are present(see §3).⁶ The second peak is dependent on the abundance of PAHs, very small grains and low ionization potential metal ions there, which can control the electron density, n_e . The abundance of PAHs and very small grains at high A_V is uncertain due to their possible coagulation on larger grain surfaces.

One significant difference between the chemical code used in this paper and that used in H09 is the inclusion of PAHs and very small grains (VSGs, radius $\lesssim 50 \text{ \AA}$), which affect the ionization balance by enhancing the recombination of positive atomic ions. In the rest of this paper we shall

⁶If a reader is interested in the second peak and knows the density n of a given source there, then our models with that n will give a good prediction of the behavior of the second peaks.

often use the term “PAH” to denote both PAHs and VSGs. PAHs also affect the second peaks of the ions by destroying electrons in the reaction $e + \text{PAH} \rightarrow \text{PAH}^-$. (The effects of PAHs on ionization balance has been treated extensively before in the literature: e.g., Lepp & Dalgarno 1988, Bakes & Tielens 1998, Weingartner & Draine 2001a, Flower & Pineau des Forets 2003, Liszt 2003, Wolfire et al 2003, 2008). H09 focused on the H_2O and O_2 peaks, which occur at relatively high $A_V \sim 3 - 7$. Although the PAH abundances are not known deep in molecular clouds, H09 assumed that their abundances are low, due to coagulation of PAHs on the surfaces of larger dust grains. Here, however, we are mostly interested in the chemistry at low $A_V < 1$, and in particular in the chemistry of diffuse clouds. These are the regions where PAHs are observed to be present, and we use PAH parameters derived from the literature. For simplicity, we adopt a single size PAH for the PAH distribution, and assume that the standard PAH has 100 C atoms, and a number abundance of $x_{\text{PAH}} = 2 \times 10^{-7}$ with respect to H nuclei (see Wolfire et al 2008 for a discussion of the amount of carbon in PAHs; here we adopt 100 C atoms and not the 35 C atoms that Wolfire et al adopted because of the result of Draine & Li 2007, which suggested that the distribution in mass peaks at 100 C atoms). One of the key impacts of PAHs is in the recombination of H^+ . As shown in Figure 1 (top), cosmic ray ionization of H can lead to OH^+ , but a competing route is the neutralization of H^+ by an electron, PAH, or PAH^- . PAHs therefore lower the production of OH^+ and the columns of all the ions in the first peak. Conversely, in the second peaks, the reduction in electron abundance caused by PAHs cause fewer H_3^+ ions to recombine with electrons, and lead to greater production rates of the ions as well as smaller destruction rates for H_3O^+ . Therefore, the columns of the ions increase with the presence of PAHs in the second peaks. We also discuss results with no PAHs or very small grains at high A_V .

In Appendix A we present Table 1 which lists the rate coefficients of key reactions in the pathways to the OH^+ , H_2O^+ , and H_3O^+ ions, as well as reactions that are either new or changed since H09. Of particular note here are the photoionization of OH and H_2O , the photodissociation of OH^+ and H_2O^+ , the treatment of PAHs—especially the photodetachment reaction rate for PAH^- , the fine structure level population dependence in the charge exchange reaction of O with H^+ , and some minor modifications in reaction rates key to determining the abundances of the OH^+ , H_2O^+ , and H_3O^+ ions, such as their dissociative recombination rates with electrons and their reactions rates with H_2 .

We have also included in Table 1 rates that are important in producing H^+ by chemical means rather than by cosmic ray ionization of H in PDRs. There are two main chemical routes. The first is initiated by the FUV photoionization of C to C^+ . The C^+ reacts with OH to form CO^+ . The CO^+ charge exchanges with H to form H^+ . The second is also initiated by FUV photoionization of C to C^+ . The C^+ reacts with H_2 to form CH^+ . The CH^+ is photodissociated by FUV photons to produce H^+ . Both these reaction chains are very much enhanced by high ($\gtrsim 300$ K) temperatures in gas with appreciable H_2 . The first chain is enhanced because high gas temperatures lead to significant amounts of OH being formed by the reaction $\text{H}_2 + \text{O} \rightarrow \text{OH} + \text{H}$. This reaction has an activation barrier of $\Delta E/k = 3160$ K and so is insignificant for low gas temperatures. The

second chain similarly is enhanced because the reaction $C^+ + H_2 \rightarrow CH^+ + H$ has an activation barrier of $\Delta E/k = 4640$ K (see Table 1).⁷ In regions where either of these two chains dominate the production of H^+ over cosmic ray ionization, the ions OH^+ , H_2O^+ , and H_3O^+ only provide upper limits to the cosmic ray ionization rates.

Other alternate routes to the production of OH^+ and H_2O^+ ions include three routes which produce OH or H_2O without the ions: the production of water on grain surfaces followed by photodesorption of the water to produce gas phase OH and H_2O , the radiative association of O with H to form OH , and the reaction of FUV-pumped H_2 in excited vibrational states with O to form OH . The gas phase OH and H_2O can be photoionized by FUV photons to produce OH^+ and H_2O^+ (see Table 1). Unlike the routes described in the preceding paragraphs, these routes are never dominant in producing the ion column densities.

An analogous route to the formation of H_2O on grain surfaces followed by photodesorption, but one not treated in this work, is the time-dependent evaporation of water ice which occurs around newly formed stars. The rapid rise in embedded luminosity heats the dust grains above about 100 K, and the icy mantles on grains are then thermally evaporated. This sudden injection of high abundances of water vapor into the gas is followed by reaction of the gas phase water with HCO^+ and H_3^+ to form H_3O^+ . Eventually, the system relaxes to the steady state chemistry described in this paper, but for a short time, there might be a large enhancement in H_3O^+ (Millar, Herbst, & Charnley 1991, PvDK92). If this release of H_2O from the icy grain surface to the gas occurs in regions with elevated FUV fields, the photoionization of H_2O could also result in enhanced H_2O^+ abundances (Gupta et al 2010)

We also present in Appendix A Table 2, which lists the gas phase elemental abundances, the PAH properties, and the grain surface area per H nucleus adopted in our code.

2.2. Interstellar Cloud Models

As noted above, our opaque molecular cloud models invoke a constant density n slab, illuminated from one side by a 1D normal FUV flux χ . We solve for the gas temperature and the gas phase and ice abundances of the various species as a function of depth in the slab. Note that depth is synonymous with hydrogen nucleus column $N [=N(H)+2N(H_2)]$ into the cloud or A_V into the cloud. We take $N = 2 \times 10^{21} A_V \text{ cm}^{-2}$. We follow the chemistry to $A_V \sim 20$, beyond which there is little contribution to the columns of OH^+ , H_2O^+ , and H_3O^+ ions.

We use the primary cosmic ray ionization rate per H atom as an input parameter, since our code calculates the secondary ionizations caused by cosmic rays and these depend on the H_2 and electron abundances. In order to probe the range of cosmic ray ionization rates suggested in the literature,

⁷As discussed in Tielens & Hollenbach (1985), our code also includes the reaction of vibrationally excited H_2 with C^+ to form CH^+ . This reaction has no activation barrier and can be moderately important at low $A_V \lesssim 0.6$.

we include cases with primary ionization rates of $\zeta_{crp} = 2 \times 10^{-17} \text{ s}^{-1}$ and $2 \times 10^{-16} \text{ s}^{-1}$ per H atom, which correspond to total rates (including secondary ionizations) of about $\zeta_{crt} \sim 3 - 5 \times 10^{-17} \text{ s}^{-1}$ and $3 - 5 \times 10^{-16} \text{ s}^{-1}$ respectively. Note that the primary rate per H_2 molecule is $2\zeta_{crp}$. We also adopt ζ_{crp} as the primary rate for He atoms; however, He has insignificant secondary ionizations. Although there is evidence that the cosmic ray ionization rate may decrease with depth (e.g., Rimmer et al 2011, Indriolo & McCall 2012, and discussion later in this paper), for simplicity we assume the primary cosmic ray ionization rate does not vary with depth into a cloud in a given model. The main effect of this assumption is that we may have overestimated the abundances and columns of the OH^+ and H_2O^+ ions in the second (deeper) peak relative to the first peak. However, since we vary ζ_{crp} in our parameter study, the reader can use lower ζ_{crp} for the columns in the second peak if so desired. The abundance of H_3O^+ in the second peak is not sensitive to ζ_{crp} if PAHs are present, as we will show below.

The main parameters that we explore for our one-sided, opaque molecular cloud models are the gas density n , the incident FUV flux χ , and the primary cosmic ray ionization rate ζ_{crp} . We study the parameter space $10 \text{ cm}^{-3} < n < 10^7 \text{ cm}^{-3}$, $1 < \chi < 10^6$, and $2 \times 10^{-17} \text{ s}^{-1} < \zeta_{crp} < 2 \times 10^{-16} \text{ s}^{-1}$. We explore the sensitivity of the columns of OH^+ , H_2O^+ , and H_3O^+ ions to assumptions about the PAH chemistry, the elemental gas phase abundances of low ionization potential metals, and the rate coefficient for the formation of H_2 on grain surfaces.

The diffuse cloud models treat a constant density slab of total thickness A_{Vt} illuminated on both sides by a 1D normal FUV flux $\chi/2$. We explore the parameter space $10^{-17.5} \text{ s}^{-1} < \zeta_{crp}/n_2 < 10^{-14.5} \text{ s}^{-1}$, $0.01 < A_{Vt} < 3$, $30 \text{ cm}^{-3} < n < 300 \text{ cm}^{-3}$, $1 < \chi < 10$, and $1 \leq \chi/n_2 \leq 10$ where $n_2 = n/100 \text{ cm}^{-3}$. The models of Wolfire et al (2003) provide a good estimate of χ/n_2 in the Galaxy by estimating χ from the star formation rate and the dust opacity as a function of galactocentric radius R , and setting the thermal pressure to provide two phases, a cold diffuse cloud phase and a warm intercloud medium that fills most of the volume. Assuming $R = 8.5 \text{ kpc}$ as the solar location, Wolfire et al find $\chi = 1.0$, $n = 33 \text{ cm}^{-3}$, and $\chi/n_2 = 3.0$ for diffuse clouds at $R = 8.5 \text{ kpc}$; $\chi = 2.35$, $n = 49 \text{ cm}^{-3}$, and $\chi/n_2 = 4.8$ at $R = 5 \text{ kpc}$; $\chi = 3.0$, $n = 54 \text{ cm}^{-3}$, and $\chi/n_2 = 5.5$ at $R = 4 \text{ kpc}$; and $\chi = 3.8$, $n = 60 \text{ cm}^{-3}$, $\chi/n_2 = 6.3$ at $R = 3 \text{ kpc}$. Therefore, our prime region for study is $\chi/n_2 = 3 - 6$. We are especially interested in how the ratio of the columns $N(\text{OH}^+)/N(\text{H}_2\text{O}^+)$ and $N(\text{OH}^+)/N(\text{H})$ vary as functions of A_{Vt} , χ/n and ζ_{crp}/n .

We note that the columns our models predict are columns perpendicular to the 1-sided (molecular cloud) slab or 2-sided (diffuse cloud) slab. If the slabs are viewed at an angle θ with respect to the normal, the observed columns will increase by $(\cos \theta)^{-1}$. Another effect that will obviously raise the columns is if there are more than one diffuse cloud (in a given velocity range) along the line of sight (los), or if the molecular cloud is clumpy and FUV scattering then introduces several “surfaces” along the los. However, as we will show, ζ_{crp}/n in diffuse clouds can be estimated from our models from the ratios $N(\text{OH}^+)/N(\text{H}_2\text{O}^+)$ and $N(\text{OH}^+)/N(\text{H})$, and the ratios are independent of the geometric effects. Nevertheless, there is some degeneracy in the solution for ζ_{crp}/n , depending on the combination of the A_{Vt} of a single cloud, χ/n , and the enhancement in columns

created by the geometrical effects.

3. MODEL RESULTS

3.1. PDR surfaces of opaque molecular clouds

3.1.1. The chemical and thermal structure of individual clouds

In order to understand the columns of OH^+ , H_2O^+ , and H_3O^+ ions produced as a function of n , χ , and ζ_{crp} , we first study the detailed chemical and thermal structure of a few specific (standard) cases. Figure 2 shows the chemical abundances as a function of depth A_V into the cloud for the case $n = 10^2 \text{ cm}^{-3}$, $\chi = 1$, and $\zeta_{crp} = 2 \times 10^{-17} \text{ s}^{-1}$. This case is chosen not only because it may be appropriate for the ambient interstellar radiation field (ISRF) incident on a relatively low density GMC, but also because the surface ($A_V \lesssim 3$) structure (i.e., T and chemical abundances as a function of depth or A_V) is illustrative of the depth structure of a diffuse or translucent cloud. In addition, the cosmic ray rate may be appropriate to the interior of molecular clouds.

The main chemical result is that the OH^+ , H_2O^+ , and H_3O^+ ions all have a peak at $0.03 < A_V < 0.3$, and then have a second peak at $A_V \sim 6$ for this combination of n and χ . We first discuss the surface peaks at low A_V . OH^+ peaks at $A_V \sim 0.03$, where the molecular hydrogen abundance is $x(\text{H}_2) \sim 0.01$. The H_2O^+ peaks slightly deeper, at $A_V \sim 0.1$, where $x(\text{H}_2) \sim 0.1$. Finally, H_3O^+ peaks at $A_V \sim 0.3$, where $x(\text{H}_2) \sim 0.25$. Appendix B provides an approximate analytic solution to the chemistry that explains the OH^+ first peak, and its relation to $x(\text{H}_2)$. From $A_V \sim 0.01$ to either $A_V \sim 0.03$ (OH^+) or $A_V \sim 0.1$ (H_2O^+) or $A_V \sim 0.3$ (H_3O^+) the three ions rise in abundance with increasing A_V because of the rise in the H_2 abundance, which drives the cosmic ray-produced O^+ to the molecular ions. At larger A_V , but for $x(\text{H}_2)$ significantly less than its maximum value of 0.5, the abundance of OH^+ and H_2O^+ plateau at the peak value because here both their formation and destruction rates are proportional to $x(\text{H}_2)$. H_2O^+ tends to peak at somewhat higher A_V than OH^+ because, even at the peak of OH^+ abundance, not all cosmic ray ionizations lead to H_2O^+ and so its abundance continues to rise as the H_2 abundance rises with increasing A_V . Finally, as $x(\text{H}_2)$ approaches 0.5, two effects lead to a drop in the OH^+ and H_2O^+ abundances with increasing A_V . One is that the formation rates of these ions saturate as nearly every cosmic ray ionization leads to their production, whereas the destruction rates still scale as $x(\text{H}_2)$, which increases with increasing A_V . The other dominant effect is that the H abundance drops so that the OH^+ formation rate via the top chain of reactions in Figure 1 drops. The bottom chain at relatively low A_V is not as efficient at producing OH^+ , as the electrons are relatively abundant ($x_e \sim 10^{-4}$) in these surface regions, and H_3^+ recombines with electrons rather than forming OH^+ .⁸ The H_3O^+ is destroyed

⁸As a result of the inefficiency of the bottom chain when the electron abundance is relatively high, the first peak is always dominated by the top chain of reactions in Figure 1, even as $x(\text{H}_2)$ approaches 0.5. The bottom chain

not by H_2 , but by electrons, whose abundance stays quite constant (supplied mostly by C^+ but with possible contribution by H^+ at high ζ_{crp}/n) at the cloud surface. The H_3O^+ starts to drop in abundance once the gas becomes predominantly H_2 , due to the second effect described above.

We next discuss the second deeper peak in the OH^+ , H_2O^+ , and H_3O^+ ions. As one moves deeper into the cloud (typically, $A_V \gtrsim 2$), the electron abundance starts to drop. As this happens, a greater fraction of the cosmic ray ionizations of H_2 leads to the production of the three ions, and their formation rates rise. The destruction of OH^+ and H_2O^+ is by H_2 , which now has constant abundance (the gas is fully H_2), so the destruction rates hold constant. Therefore, these two ions rise in abundance. Finally, they peak and fall in abundance for $A_V > 6$ because gas phase oxygen freezes out as water ice, and again the oxygen reaction with H_3^+ cannot compete with H_3^+ electronic recombination or its reaction with CO . Therefore, the formation rates of all three ions drop. H_3O^+ behaves somewhat more dramatically, because its destruction is mainly by dissociative recombination with electrons. Thus, as the electron abundance drops, not only is the formation rate of H_3O^+ enhanced, but the destruction rate is suppressed. Therefore, H_3O^+ rises to much higher abundances than OH^+ and H_2O^+ in the second peak. It also drops at very high A_V because gas phase elemental oxygen from which H_3O^+ forms freezes out as water ice.

In this particular case, there is a column of $N(\text{OH}^+) = 2 \times 10^{11} \text{ cm}^{-2}$ in the first surface peak and $4 \times 10^{11} \text{ cm}^{-2}$ in the deeper peak; for H_2O^+ the columns are $1.4 \times 10^{11} \text{ cm}^{-2}$ and $2 \times 10^{11} \text{ cm}^{-2}$; and for H_3O^+ the columns are $1.1 \times 10^{11} \text{ cm}^{-2}$ and $9.4 \times 10^{13} \text{ cm}^{-2}$. The columns of OH^+ and H_2O^+ are not detectable. Typically, columns of $\gtrsim 10^{12} \text{ cm}^{-2}$ are needed for detection via absorption spectroscopy. In particular, observations of OH^+ often imply columns $\gtrsim 10^{13} \text{ cm}^{-2}$, which suggests that higher cosmic ray rates are required. Therefore, for the rest of our standard cases we use $\zeta_{crp} = 2 \times 10^{-16} \text{ s}^{-1}$. Most of the H_3O^+ column is produced in the second deeper peak, and in our model the predicted columns are detectable. For an absorption measurement a background submillimeter source behind or in a cloud with $A_V > 6$ from observer to submillimeter source is required.

Figure 3 shows the case $n = 10^2 \text{ cm}^{-3}$, $\chi = 1$, and $\zeta_{crp} = 2 \times 10^{-16} \text{ s}^{-1}$: in other words, the same as Figure 2 but with ten times the cosmic ray ionization rate. The abundances of all three ions in the first peak rise in proportion to ζ_{crp} . The OH^+ and H_2O^+ ion abundances in the second peak also scale roughly with ζ_{crp} . The column of $N(\text{OH}^+) = 2.2 \times 10^{12} \text{ cm}^{-2}$ in the first peak and $3.2 \times 10^{12} \text{ cm}^{-2}$ in the deeper peak; for H_2O^+ the columns are $1.5 \times 10^{12} \text{ cm}^{-2}$ and $6.9 \times 10^{12} \text{ cm}^{-2}$; and for H_3O^+ the columns are $9.2 \times 10^{11} \text{ cm}^{-2}$ and $7.3 \times 10^{13} \text{ cm}^{-2}$. Because the electron abundance is low in the second peak, a significant fraction (.1 – 0.3) of cosmic ray ionizations of H_2 lead to OH^+ and H_2O^+ , and their destruction is by H_2 , which does not change in abundance with varying ζ_{crp} . Thus, the scaling of OH^+ and H_2O^+ abundances and columns

dominates in the second peak, however, because the H_2 abundance is high and the electron abundance is low.

with ζ_{crp} .⁹ However, the H_3O^+ abundance in the second peak does not rise linearly with ζ_{crp} , but stays fairly constant, because although the formation rate scales with ζ_{crp} , the destruction rate also increases as ζ_{crp} is raised, due to the higher electron abundances produced by the enhanced cosmic ray flux. Unlike OH^+ and H_2O^+ , which are destroyed by H_2 , H_3O^+ is destroyed by dissociative recombinations with electrons. In fact, to first order, we would expect the abundance of H_3O^+ to scale as $\zeta_{crp}/n_e = \zeta_{crp}/(x_e n)$ at the second peak.

The abundance of electrons x_e deep in the cloud depends on the uncertain PAH abundance deep in the cloud. If the PAH abundance remains as high as is indicated in diffuse clouds and cloud surfaces (as we assume in our standard models), then we obtain the following result. Electrons are formed by cosmic ray ionization of H_2 . Electrons are mainly destroyed by collisional attachment to neutral PAHs, and the PAHs are mostly neutral. Therefore, the abundance of electrons $x_e \propto \zeta_{crp}/n$. As a result, if PAHs are abundant in this deep peak, we predict that $x(\text{H}_3\text{O}^+) \propto \zeta_{crp}/(x_e n)$ will be independent of both n and ζ_{crp} ! Note that Figure 3 compared to Figure 2 shows that the electron abundance in the second peak does scale roughly as ζ_{crp} , and that the abundance of H_3O^+ in the second peak does not change significantly as we increase the cosmic ray ionization rate by 10. Appendix B presents an analytic solution for $x(\text{H}_3\text{O}^+)$ near the second peak if PAHs are present. Since cosmic ray ionization of H_2 is similar to X-ray ionization of H_2 , this result implies that, *if PAHs are present*, regions of enhanced X-ray ionization will not show enhanced H_3O^+ columns. We discuss in §3.1.3 the case of no PAHs at high A_V .

Figure 4 shows the same case as Figure 3, but plots a parameter ϵ , first discussed by N10. Here, the parameter ϵ is defined as the rate per unit volume of formation of OH^+ divided by the total (not primary) rate per unit volume of cosmic ray ionization of H and H_2 . In effect, ϵ is an efficiency parameter in determining the formation of OH^+ from cosmic rays. If PAH, PAH^- and electron abundances are relatively low, and H_2 and gas phase O abundances are high, then ϵ is near unity. Essentially, one needs O^+ to react with H_2 before H^+ reacts with e, PAH, or PAH^- . Although this qualitative limit is clear from the chemical pathways shown in Figure 1, we derive in Appendix B an analytic formula for ϵ which makes this statement more quantitative. Roughly, the condition for ϵ to be of order unity is:

$$\left(\frac{x(\text{H}_2)}{0.5}\right) \left(\frac{x(\text{O})}{10^{-4}}\right) \gtrsim 0.028e^{230/T} \left[\left(\frac{x_e}{3 \times 10^{-4}}\right) + 4.4 \left(\frac{x(\text{PAH}^-)}{1.5 \times 10^{-8}}\right) + 2.7 \left(\frac{x(\text{PAH})}{1.85 \times 10^{-7}}\right) \right] \quad (1)$$

However, if the reverse is true, then H^+ can recombine with PAH, PAH^- , or electrons and disrupt the chain of reactions that lead to OH^+ , leading to low (< 1) values of ϵ . Figure 4 also plots the temperature and repeats the plots of the abundances of H_2 and electrons, since they help determine the value of ϵ , as well as the abundance of OH^+ (see Appendix B). Finally, we add the abundance of H_3^+ to Figure 4 since it is also used to estimate cosmic ray rates (e.g., Indriolo et al 2007, 2011).

⁹Even at the second peak, both electrons and CO compete with O in reacting with H_3^+ .

Because H_3^+ is formed by the reaction of H_2 with H_2^+ and often destroyed by electrons (see Figure 1), we see the H_3^+ abundance rise with A_V as the H_2 abundance rises and the electron abundance falls. In general, the H_3^+ probes the cosmic ray ionization rates at higher A_V than the first peak in OH^+ .

Figures 5 and 6 show the case $n = 10^4 \text{ cm}^{-3}$, $\chi = 100$, and $\zeta_{crp} = 2 \times 10^{-16} \text{ s}^{-1}$. This case is nearly identical to the standard case in H09, and is representative of a Giant Molecular Cloud (GMC) surface illuminated by an FUV field somewhat higher than the interstellar radiation field because of the presence of nearby O and B stars. The total cosmic ray ionization rate ($\sim 3\text{--}5 \times 10^{-16} \text{ s}^{-1}$ including secondary ionizations) may represent values on the surfaces of GMCs, but may be somewhat high for the interior. We see from Figures 4 and 6 that the gas temperatures of the molecular interiors of these clouds at $A_V > 5$ is of order 30 K for $n = 10^4 \text{ cm}^{-3}$ and 70 K for $n = 100 \text{ cm}^{-3}$, due to cosmic ray heating when $\zeta_{crp} = 2 \times 10^{-16} \text{ s}^{-1}$. Typically, temperatures in molecular cloud interiors are observed to be $\lesssim 30 \text{ K}$, suggesting that such high cosmic ray ionization rates may not be appropriate for molecular cloud interiors. However, as we shall see, such high cosmic ray rates are required to explain observations of diffuse clouds, which should have the same cosmic ray rates as the surfaces ($A_V \lesssim 2$) of GMCs. This suggests that ζ_{crp} may be higher on the surface of a molecular cloud than deep in its interior.

If chemistry is driven by FUV photoreactions and particle-particle reactions, such as H/H_2 chemistry, then the chemical abundances mainly depend on the ratio χ/n . Therefore, one expects and sees that the H_2 abundance of Figure 5 closely matches that of Figures 2 and 3, which have the same χ/n ratio. The H_2 abundance in the higher χ case is a bit lower because of FUV photodissociation of H_2 in FUV-pumped excited vibrational states of H_2 .

However, the molecular ion abundances in the first peak depend to first order on the ratio ζ_{crp}/n (see Appendix B) and are not too sensitive to χ . Thus, in this $n = 10^4 \text{ cm}^{-3}$ case, their abundances in the first peak drop by a factor of nearly 10-30 compared to Figure 3 (which has the same value of ζ_{crp}) as the density rises by 100 from the $n = 10^2 \text{ cm}^{-3}$ assumed in Figure 3. Slight differences in electron abundances, H_2 abundances, and T explain the divergence from the expected n^{-1} dependence.

The second peaks of OH^+ and H_2O^+ nearly scale as n^{-1} , as expected. However, the second peak of the H_3O^+ abundance ($\sim 10^{-8}$) is independent of n , as predicted above by the scalings of the electron density with n and ζ_{crp} if PAHs are present.

Figure 7 shows the case $n = 10^6 \text{ cm}^{-3}$, $\chi = 10^5$, and $\zeta_{crp} = 2 \times 10^{-16} \text{ s}^{-1}$. This case may represent strongly illuminated PDRs such as may occur around embedded compact or ultracompact HII regions, or possibly embedded protostars illuminating the opaque walls of outflow cones. This high density and high FUV flux case was chosen because most of the column of all three ions is produced not by cosmic ray ionization, but by other chemical reactions. In Figure 7 we see an enormous enhancement of OH^+ abundance at $A_V \sim 1.6$. Here, $T \sim 1000 \text{ K}$ and at the same time the abundance of H_2 is moderately high, $\sim 10^{-2}$. At these elevated temperatures, as discussed in

§2.1, the H_2 can react rapidly with O to form OH or with C^+ to form CH^+ , leading to reaction chains that make OH^+ , H_2O^+ , and H_3O^+ . One of the key heating mechanisms providing this high T is the FUV pumping and the H_2 formation pumping of excited vibrational levels of H_2 , followed by collisional de-excitation of these levels which leads to gas heating (e.g., Tielens & Hollenbach 1985). The essential point is that the OH^+ , H_2O^+ , and H_3O^+ columns are not provided by cosmic ray ionization, and therefore cannot diagnose the cosmic ray ionization rate, except to give an upper limit.

3.1.2. Contour plots of integrated columns of ions

Figure 8 shows the contours of the integrated (from $A_V = 0$ to $A_V = 20$) columns of OH^+ ions for a primary cosmic ray ionization rate of $\zeta_{crp} = 2 \times 10^{-16} \text{ s}^{-1}$ per H atom, and plotted as functions of n and χ . Note that the OH^+ columns include both the first and second peaks. We emphasize that these are columns perpendicular to the face of the PDR slab. If clouds are observed obliquely, proportionately more column will be in the line of sight. Similarly, if we are observing a slab illuminated on both sides, the columns will be raised by a factor of 2 if the slab is quite optically thick ($A_V \gg 1$) so that first and second peaks occur on both sides. The upper right hand portion of the figure is blacked out because radiation pressure, photoelectric emission, and photodesorption forces on dust grains, when $\chi/n_2 \gtrsim 300$, drives dust rapidly through the PDR (Weingartner & Draine 2001b). Such high ratios of χ/n rarely occur in nature, and require a much more detailed PDR code.

Figure 8 shows two main features. First, at low $\chi \lesssim 1000$ or low $n \lesssim 10^4 \text{ cm}^{-3}$, the columns of OH^+ are roughly proportional to n^{-1} and almost independent of χ , as discussed above. There is a weak dependence on χ for $\chi \lesssim 1000$ because higher χ leads to higher gas T , and the O^+ abundance rises with $\exp(-230 \text{ K}/T)$. From this figure it is clear that since OH^+ columns of at least 10^{12} cm^{-2} are needed to make absorption observations feasible, low density ($n \lesssim 300 \text{ cm}^{-3}$) clouds should be targeted if $\zeta_{crp} = 2 \times 10^{-16} \text{ s}^{-1}$. It should also be noted, as is obvious in Figures 2, 3 and 5, that both the first and second peaks contribute to the OH^+ column so that there is substantial column at both $A_V < 1$ and $A_V > 1$. The OH^+ in this case is quite cold, $T \lesssim 200 \text{ K}$. Second, these relations completely break down in the upper right portion ($n \gtrsim 10^4 \text{ cm}^{-3}$ and $\chi \gtrsim 10^3$) of this contour plot. Here, as discussed above, the high χ and n (high density brings the H/ H_2 interface closer to the surface, where the gas is warm) lead to very warm ($T \sim 1000 \text{ K}$) H_2 near the surface ($A_V \lesssim 2$) of the cloud. This warm H_2 drives reactions which produce OH^+ without the need for cosmic ray ionization. In this way, observable columns of OH^+ can be formed at these elevated values of χ and n , and the columns occur at moderate $A_V \sim 2$. The OH^+ in this case is quite warm, $T \gtrsim 300 \text{ K}$, and its column is independent of ζ_{crp} , but depends on n and χ .

Figure 9 shows the contours of the integrated (from $A_V = 0$ to $A_V = 20$) columns of H_2O^+ ions for a primary cosmic ray ionization rate of $\zeta_{crp} = 2 \times 10^{-16} \text{ s}^{-1}$ per H atom. This figure can be compared with Figure 8, which treats the same cosmic ray case for OH^+ . We focus on regions

where these ions might be detectable, that is, for columns $> 10^{12} \text{ cm}^{-2}$, and in the cosmic ray dominated zones of n and χ . In these low density regions, comparison of Figure 9 with 8 reveals that the column ratios are of order unity, as might be expected. The formation rates of these two ions are nearly the same (stemming from the cosmic ray ionization rate) and the destruction rates of these two molecules are nearly the same (via H_2 in the regions where most of the columns are generated). Note that in Figures 2, 3, and 5 the local OH^+ abundance peaks at lower values of A_V than the H_2O^+ abundance, and that Figures 8 and 9 present integrated columns through a high A_V slab. Therefore, we can obtain higher column ratios of these two molecular ions if we truncate our slabs to small diffuse clouds with $A_V < 1$ (see below, §3.2.2).

We do not provide a contour plot similar to Figures 8 and 9 but with different ζ_{crp} because the results are simple to describe. For $\chi \lesssim 1000$ the OH^+ and H_2O^+ columns scale as ζ_{crp} . For $\chi \gtrsim 1000$ the columns are independent of ζ_{crp} because cosmic rays do not produce the OH^+ and H_2O^+ . Forcing a fit with the expected (to first order) ζ_{crp}/n dependence in the cosmic ray-dominated region $\chi \lesssim 100$, we find roughly (factor of 2) the simple expressions

$$N(\text{OH}^+) \sim 5 \times 10^{12} \chi^{1/3} \left(\frac{100 \text{ cm}^{-3}}{n} \right) \left(\frac{\zeta_{crp}}{2 \times 10^{-16} \text{ s}^{-1}} \right) \text{ cm}^{-2}. \quad (2)$$

and

$$N(\text{H}_2\text{O}^+) \sim 10^{13} \chi^{1/4} \left(\frac{100 \text{ cm}^{-3}}{n} \right) \left(\frac{\zeta_{crp}}{2 \times 10^{-16} \text{ s}^{-1}} \right) \text{ cm}^{-2}. \quad (3)$$

We emphasize that these columns are the total OH^+ and H_2O^+ columns in both the first and second peaks.

We do not present integrated (from $A_V = 0$ to $A_V = 20$) columns of H_3O^+ ions because, as discussed above, most of their column arises at high $A_V \sim 6$ and this second peak column is quite constant as a function of n , χ , and ζ_{crp} if PAHs are present at the same abundances as in diffuse clouds. With PAHs present in the second peak, we find that the H_3O^+ column is slightly dependent on the gas density, varying from 10^{14} cm^{-2} at $n \sim 100 \text{ cm}^{-3}$ to $10^{13.5} \text{ cm}^{-2}$ at $n \sim 10^6 \text{ cm}^{-3}$. At densities of $n = 100 \text{ cm}^{-3}$ and with $\chi = 1$ and $\zeta_{crp} = 2 \times 10^{-16} \text{ s}^{-1}$, we remind the reader (see discussion of Figure 3) that $N(\text{H}_3\text{O}^+) = 9.2 \times 10^{11} \text{ cm}^{-2}$ in the first peak; like OH^+ and H_2O^+ the column of H_3O^+ in the first peak scales with ζ_{crp}/n so that even lower densities or higher ζ_{crp} are needed to make H_3O^+ detectable in the first peak (e.g., in a diffuse foreground cloud).

3.1.3. Sensitivity to PAH abundance and other parameters

PAHs may not have a high abundance deep in the high A_V regions of a molecular cloud, perhaps due to coagulation of PAHs on larger grains (see, for example, discussion in H09). We have run a number of cases with the PAH abundance set to zero to see the effect on the second peaks. In these runs, we also reduce the number of small grains by setting the minimum grain size to 100 \AA , but we still refer below to this case as the "no PAH" case for high A_V cloud interiors .

The results depend on the gas phase abundance of metals, like S, Si, Mg, and Fe; see Table 2 of Appendix A for our assumed gas phase abundances of these species in the interstellar radiation field. Our code follows the freezeout of these species as a function of depth into the cloud, as photodesorption no longer is able to keep the metal atoms off the grain surfaces. The photodesorption yields of these species are not known. We find that for yields greater than 10^{-6} , there are still sufficient gas phase metals present at the second peak to supply electrons and suppress the H_3O^+ abundance by factors of $\gtrsim 10$ relative to the case with PAHs. However, if the photodesorption yields are very low so that the gas phase abundances of these metals at the second peak are $\lesssim 3 \times 10^{-8}$, then we obtain H_3O^+ columns in the second peak comparable to the case with PAHs. For example, assuming $n = 10^4$ and $\chi = 100$, we obtain $N(\text{H}_3\text{O}^+) = 4 \times 10^{13} \text{ cm}^{-2}$ if $\zeta_{\text{crp}}/n_2 = 2 \times 10^{-16} \text{ s}^{-1}$ per H atom, and $N(\text{H}_3\text{O}^+) = 8 \times 10^{13} \text{ cm}^{-2}$ if $\zeta_{\text{crp}}/n_2 = 2 \times 10^{-15} \text{ s}^{-1}$ per H atom. The main difference between the PAH and no PAH case lies in the electron loss mechanisms: with PAHs the electrons are lost by encountering PAHs; with no PAHs the electrons are lost by recombining with ions. The atomic ions have slower rates of recombination than the molecular ions, so the presence of metal atomic ions leads to higher electron abundances and lower H_3O^+ columns. The OH^+ and H_2O^+ abundances and columns also decrease in the second peak, but by smaller factors ($\lesssim 3$), because their destruction is not by electrons but by H_2 , whose abundance does not change.

In Appendix C we discuss the lack of sensitivity of the results on certain key reaction rate coefficients, the assumed abundance of gas phase oxygen, and on the rate coefficient for H_2 formation on grain surfaces. We discuss the effect of *raising* the gas phase abundances of metals. We also treat the increase in the H_3O^+ columns in the second peak if elemental O does not freeze (as water ice) at high A_V .

3.2. Diffuse and Translucent Clouds

Diffuse clouds have relatively small columns, $A_V \lesssim 1$, whereas translucent clouds have columns intermediate between diffuse clouds and GMCs, $1 \lesssim A_V \lesssim 5$. Although GMCs have sufficient column to incorporate both peaks of the OH^+ , H_2O^+ , and H_3O^+ abundances, diffuse and translucent clouds typically (with the possible exception of the highest A_V translucent clouds) only contain the surface peak. In fact, a diffuse cloud may have such small A_V that the cloud may truncate the full peak of one or all of the ions. Therefore, the parameter A_{Vt} , the total A_V through the cloud becomes an important new parameter in determining, for example, ratios of the columns of the ions.

Both diffuse and translucent clouds have insufficient column to be gravitationally bound, so generally they are in thermal pressure equilibrium with the interstellar medium. The local typical value of the thermal pressure is $nT \sim 3 - 4 \times 10^3 \text{ cm}^{-3} \text{ K}$, and this pressure may rise by factors of 2-3 for clouds in the molecular ring of the Galaxy (Wolfire et al 2003). As discussed above (§2.2), depending on the galactocentric radius R , they have densities $30 \text{ cm}^{-3} < n < 100 \text{ cm}^{-3}$, temperatures $T \sim 50 - 100 \text{ K}$, and incident FUV fluxes characterized by $1 < \chi < 4$. The ratio χ/n_2 , critical to the photochemistry, varies typically from about 3-6, although we explore a somewhat

larger range 3-10 here.

In the low density regime, $n < 10^3 \text{ cm}^{-3}$, appropriate for diffuse and translucent clouds, there is a scaling of the results of thermochemical models. The parameters which control the thermochemical structure of a cloud are just χ/n , ζ_{crp}/n , and A_{Vt} . We note that this scaling does not apply to the denser PDR models discussed in the previous section. At high density, $n > 10^3 \text{ cm}^{-3}$, the cooling of the gas is suppressed by collisional de-excitation of the fine structure states of C^+ and O . Therefore, higher density gas will typically give higher gas temperatures, even when χ/n is held constant. However, given that this scaling applies for diffuse and translucent clouds, we generally in this section plot our results as functions of χ/n , ζ_{crp}/n , and A_{Vt} . We note that this implies that the observations may give us a measure of ζ_{crp}/n , but to get an estimate of ζ_{crp} we will then have to estimate the gas density n in the region observed.

3.2.1. The total column of OH^+ through a diffuse cloud of size A_{Vt}

Figure 10 plots the column of OH^+ , $N(\text{OH}^+)$, as a function of A_{Vt} for four values of ζ_{crp}/n_2 (recall, $n_2 \equiv n/100 \text{ cm}^{-3}$) and for $\chi/n_2 = 3.16$. The dotted lines plot $x_c(\text{H}_2)$, the abundance of H_2 at cloud center, and these values appear on the right of the figure. Recall A_{Vt} is the total A_V through the diffuse slab, measured perpendicular to the slab and the ion columns plotted are perpendicular to the slab.

Figure 10 shows that $N(\text{OH}^+)$ increases with ζ_{crp}/n and with A_{Vt} , although one sees a saturation of the column with A_{Vt} at $A_{Vt} \gtrsim 0.3$ for the lower three cases of ζ_{crp}/n . This saturation is due to the peaking of the local OH^+ abundance at lower values of A_V . Figure 10 shows that $N(\text{OH}^+)$ correlates with $x_c(\text{H}_2)$, and that moderate molecular hydrogen abundances $x_c(\text{H}_2) \gtrsim 0.03$ are required to obtain substantial columns of OH^+ . Observed OH^+ columns in broad ($\Delta v \sim 20 \text{ km s}^{-1}$, see §4.1.1) velocity components in the ISM are of order $3 \times 10^{13} - 3 \times 10^{14} \text{ cm}^{-2}$. With this value of $\chi/n_2 = 3.16$, we see that it requires very high cosmic ray ionization rates, $\zeta_{crp}/n_2 \gtrsim 3 \times 10^{-16} \text{ s}^{-1}$ and high $A_{Vt} \gtrsim 0.3$ for a single cloud, seen face on, to produce these columns. Therefore, it appears that geometrical effects such as seeing several clouds along the line of sight, or viewing the cloud obliquely, may be required to match observation. In fact, as we discuss in §4.1.1, many clouds may be required to cover the broad ($\Delta v \sim 20 \text{ km s}^{-1}$) absorption components since single clouds would have much narrower velocity widths. Because of geometrical effects and variation in A_{Vt} and χ/n , the observation of the column of OH^+ is not sufficient to tightly restrict ζ_{crp}/n .

Figure 11 plots $N(\text{OH}^+)$ as a function of A_{Vt} for four values of ζ_{crp}/n_2 and for $\chi/n_2 = 10$: in other words, the same as Figure 10 but with a ratio of χ/n that is 3.16 times higher. The main effect of raising χ/n is to push the H/H_2 transition deeper into the cloud to higher A_V . This is seen in the plot of $x_c(\text{H}_2)$ which rises to 0.01 at $A_{Vt} \sim 0.3$ in this case, compared to $A_{Vt} \sim 0.1$ in the previous case of $\chi/n_2 = 3.16$. Since H_2 is required to make OH^+ , this moves the peak of OH^+ to higher values of A_V , and thus pushes the rise of $N(\text{OH}^+)$ to higher values of A_{Vt} than in

Figure 10. However, this first peak has more column of OH^+ compared with the case $\chi/n_2 = 3.16$. Therefore, to produce the observed columns of OH^+ now requires only $\zeta_{crp}/n_2 \gtrsim 3 \times 10^{-17} \text{ s}^{-1}$ and high $A_{Vt} \gtrsim 1$ for a single cloud, seen face on.

3.2.2. $N(\text{OH}^+)/N(\text{H}_2\text{O}^+)$ and $N(\text{OH}^+)/N(\text{H})$ through a diffuse cloud of size A_{Vt}

The results on the total column of OH^+ suggests that other observations must be brought into play to further restrict the cosmic ray ionization rate. Since H_2O^+ is often observed as well, we first consider the ratio $N(\text{OH}^+)/N(\text{H}_2\text{O}^+)$. As seen in Figures 2, 3, and 5, the H_2O^+ abundance peaks at higher values of A_V than the OH^+ abundance. Therefore, the ratio of the columns of these two ions may give us some measure of A_{Vt} .

Figure 12 plots the ratio $N(\text{OH}^+)/N(\text{H}_2\text{O}^+)$ as a function of A_{Vt} for four values of ζ_{crp}/n_2 and for $\chi/n_2 = 3.16$. As expected, at low values of $A_{Vt} \lesssim 0.1$, the ratio $N(\text{OH}^+)/N(\text{H}_2\text{O}^+)$ is high, $\sim 10 - 30$, as we have not yet reached high enough values of A_V to include the H_2O^+ peak. However, as A_{Vt} increases, the ratio of the columns continues to drop until at $A_{Vt} \gtrsim 1$, the ratio is approximately 2-3, except in the case of the highest cosmic ray rate $\zeta_{crp}/n_2 = 3.16 \times 10^{-15} \text{ s}^{-1}$.¹⁰ Once we have incorporated both the OH^+ and the H_2O^+ abundance peaks, the column ratios are near unity, as noted in §3.1.

Figure 13 plots the ratio $N(\text{OH}^+)/N(\text{H}_2\text{O}^+)$ as a function of A_{Vt} for four values of ζ_{crp}/n_2 and for $\chi/n_2 = 10$: in other words, the same cases as Figure 12 except the ratio χ/n is raised by a factor of 3.16. The rise in χ/n pushes the H/H_2 transition and the peaks of OH^+ and H_2O^+ to higher values of A_V . Therefore, compared to Figure 12, we see the drop in the $N(\text{OH}^+)/N(\text{H}_2\text{O}^+)$ ratio at higher values of A_{Vt} . The observed ratios of $N(\text{OH}^+)/N(\text{H}_2\text{O}^+)$ range from 3-15. If $\chi/n_2 = 3.16$ and if we assume that $\zeta_{crp}/n_2 \lesssim 3 \times 10^{-16} \text{ s}^{-1}$, Figure 12 suggests that $A_{Vt} \sim 0.1 - 0.3$ to obtain these ratios. However, if this is true, Figure 10 implies that even with as high a value of $\zeta_{crp}/n_2 = 3 \times 10^{-16} \text{ s}^{-1}$, we will need a “geometrical factor” of ~ 10 in order to obtain $N(\text{OH}^+) \sim 10^{14} \text{ cm}^{-2}$. This geometrical factor is the combination of many clouds along the line of sight, along with the enhancement in column due to viewing angle of the cloud. The situation changes with $\chi/n_2 = 10$, as seen in Figure 13. Here, again assuming that $\zeta_{crp}/n_2 \lesssim 3 \times 10^{-16} \text{ s}^{-1}$, the observed ratios can be obtained with $A_{Vt} \sim 1 - 3$. In this case, using Figure 11, the geometrical factor needs to be only $\sim 1 - 3$ to produce OH^+ columns of 10^{14} cm^{-2} when $\zeta_{crp}/n_2 \sim 3 \times 10^{-16} \text{ s}^{-1}$.

Observations of HI 21 cm are often available along the same lines of sight as the OH^+ and

¹⁰The $\zeta_{crp}/n_2 = 3.16 \times 10^{-15} \text{ s}^{-1}$ case is extreme; cosmic ray ionization of H produces an electron abundance of $x_e \simeq 3 \times 10^{-3}$. In this case, electrons and not H_2 dominate the destruction of OH^+ and H_2O^+ even when $x(\text{H}_2) \sim 0.5$. Therefore, the fraction of cosmic ray ionizations that produce OH^+ is higher than the fraction that produce H_2O^+ , even at the peaks of their abundance. Hence we have much more OH^+ than H_2O^+ as seen in this figure, and, once we reach high enough A_{Vt} where the ion chemistry shown in Figure 1(top) dominates, the ratio rises as a function of A_{Vt} . This holds as well in X-ray ionized regions with high ionization rates.

H_2O^+ measurements. In this case, the column of HI, $N(\text{H})$, along the line of sight associated with the velocity feature of the ions can be estimated. To be precise, the observations directly give $N(\text{H})/T$, where T is an average temperature along the line of sight. In Figures 14 and 15 we plot the ratio $N(\text{OH}^+)/[N(\text{H})/T_2]$ on the vertical axis ($T_2 = T/100$ K) and the ratio $N(\text{OH}^+)/N(\text{H}_2\text{O}^+)$ on the horizontal axis for two fixed values of $\chi/n_2 = 3.16$ and 10. The results of our 2 sided diffuse cloud models are shown as contours on this figure. As noted above, higher average abundances of OH^+ (or $N(\text{OH}^+)/N(\text{H})$) requires higher ζ_{crp}/n . On the other hand, higher $N(\text{OH}^+)/N(\text{H}_2\text{O}^+)$ requires either low A_{Vt} or high χ/n . In the next section we apply Figures 10, 11, 14, and 15 to the observational data to constrain ζ_{crp}/n along sightlines to W49N.

3.2.3. The possible effects of turbulence

We have run additional models to estimate how turbulence might affect the production of OH^+ , H_2O^+ , and H_3O^+ . It has been recognized for several decades that standard astrochemical models for diffuse molecular clouds greatly underpredict the observed column densities ($\sim 10^{13}$ cm^{-2}) of CH^+ (e.g., Falgarone et al 2010a,b; and references therein.) The models presented here are no exception; in our models with $\chi \sim 1$, $n \sim 100$ cm^{-3} , and $A_{Vt} > 1$, for example, we obtain a predicted CH^+ column density $\sim 3 \times 10^{10}$ cm^{-2} , more than two orders of magnitude lower than that typically observed. Both shock waves with large scale order (Elitzur & Watson 1978, Draine & Katz 1986, Flower & Pineau des Forets 1998), and interstellar turbulence (e.g. Joulain et al. 1998; Lesaffre et al 2007, Godard et al 2009, Falgarone et al 2010a,b) have been proposed as sources of heating that could enhance the CH^+ abundance within some small fraction of the cloud volume; in these models, CH^+ is formed by the endothermic reaction of C^+ with H_2 . It has also been long recognized (e.g. Draine & Katz 1986) that models invoking ion-neutral drift – either in C-type shock waves or in turbulent dissipation regions – are most successful in simultaneously matching the observed column densities of CH^+ and OH. In particular, while models in which the gas temperature is merely elevated without significant ion-neutral drift tend to overpredict the OH/ CH^+ ratio (the neutral-neutral endothermic reaction $\text{O} + \text{H}_2 \rightarrow \text{OH} + \text{H}$ being enhanced along with the reaction of C^+ with H_2), models incorporating ion-neutral drift preferentially enhance the endothermic ion-molecule reactions that produce CH^+ (and SH^+ ; Godard et al. 2012), *without* producing more OH than the observations permit. We have crudely estimated the effects of turbulence by positing an enhanced rate of endothermic ion-neutral reactions in a small fraction of the cloud volume. Motivated by recent calculations performed by Myers & McKee (private communication), we adopted enhanced ion-neutral reaction rates - equal to the thermal rate coefficients at 1000 K - in 3% of the cloud volume: this leads to a predicted CH^+ column in accord with what is typically observed.¹¹ We found that turbulence does not greatly enhance the OH^+ , H_2O^+ , and

¹¹In particular, we add 97% of the columns from our standard model to 3% of our columns from the same model but with the enhanced ion-neutral rates to obtain the total columns of, for example, CH^+ .

H_3O^+ column densities through such a cloud. There was a modest enhancement of these oxygen hydride ions within the region of ion-neutral drift, due to the faster reaction of H^+ with O, but since that region occupies only a small fraction of the total volume, this effect did not affect the total column densities significantly. Therefore, we conclude that turbulent dissipation or shocks in small regions of the clouds are unlikely to affect our conclusions concerning OH^+ , H_2O^+ or H_3O^+ in the models presented here.

4. OBSERVATIONS AND COMPARISON WITH MODEL PREDICTIONS

4.1. OH^+ , H_2O^+ , and H_3O^+ Absorption in Diffuse Galactic Molecular Clouds

As discussed in §1, recent *Herschel* observations of bright Galactic continuum sources have revealed OH^+ and H_2O^+ absorption features arising in multiple foreground clouds along the targeted sight-lines (Gerin et al. 2010; N10; Neufeld et al. 2011). The three crosses in Figure 14 denote the $N(\text{OH}^+)/N(\text{H}_2\text{O}^+)$ and $N(\text{OH}^+)/[N(\text{H})/T_2]$ ratios for the two such sources for which results have been reported to date: G10.6–0.4 (a.k.a. W31C) (the lower limits) and W49N (2 points to the right). Those given for G10.6–0.4 apply to all the material along the sight-line, while those given for W49N apply to two separate velocity intervals (30–50 km s^{-1} and 50–78 km s^{-1}). The OH^+ absorption in G10.6–0.4 is largely saturated, and thus the plotted values are lower limits. For W49N, the columns of H derived assumed $T = 100$ K or $T_2 = 1$; the quoted values of $N(\text{H})/T_2$ are $6.95 \times 10^{21} \text{ cm}^{-2}$ for the 30 – 50 km s^{-1} feature and $7.23 \times 10^{21} \text{ cm}^{-2}$ for the 50 – 78 km s^{-1} feature. The total columns $N(\text{OH}^+)$ observed in these two velocity intervals are 3.6×10^{14} and $2.1 \times 10^{14} \text{ cm}^{-2}$, respectively.

The $N(\text{OH}^+)/N(\text{H}_2\text{O}^+)$ ratios measured toward W49N (~ 10) and the wide velocity range of the absorbing clouds suggest that the absorbing material is comprised of multiple clouds of small extinction. The line of sight to W49N is approximately 11 kpc long, and passes as close as $R = 5$ kpc to the Galactic center. Assuming $\chi/n_2 = 3.16$, models with $A_{Vt} = 0.32$ and 0.25 best account for all the data (Figure 14), with cosmic-ray ionization rates of ~ 6 and $4 \times 10^{-16} n_2 \text{ s}^{-1}$, respectively, for the 30 – 50 km s^{-1} and 50 – 78 km s^{-1} velocity intervals. As seen in Figure 10 for $\chi/n_2 = 3.16$, the column of OH^+ in a single cloud of size $A_{Vt} = 0.32$ is $N(\text{OH}^+) \simeq 2 \times 10^{13} \text{ cm}^{-2}$ and for $A_{Vt} = 0.25$ is $N(\text{OH}^+) \simeq 1.5 \times 10^{13} \text{ cm}^{-2}$. Therefore, we either need ~ 15 clouds along the line of sight, or a smaller number but with geometrical enhancement effects. Note that a single cloud might have an OH^+ absorption linewidth of only $\sim 1 - 3 \text{ km s}^{-1}$. Therefore, to cover the broad absorption features we are modeling ($\Delta v = 20$ or 28 km s^{-1}), we need 10–30 clouds spread out along the line of sight so that their galactic rotational velocities coupled with their individual line widths cover this velocity range. Therefore, this $\chi/n_2 = 3.16$ model has barely enough clouds to produce the relatively smooth absorption feature observed. Assuming $\chi/n_2 = 10$, models with $A_{Vt} \simeq 0.75$ and $A_{Vt} \simeq 0.63$ and with $\zeta_{crp}/n_2 \sim 2 \times 10^{-16}$ and $1.2 \times 10^{-16} \text{ s}^{-1}$, respectively, best account for the data (see Figure 15). With these values of A_{Vt} and ζ_{crp}/n_2 , inspection of Figure

11 shows that we require ~ 12 clouds along the line of sight. This value of χ/n_2 has even fewer clouds to cover the broad absorption line observed. Moreover, the temperatures in clouds with $\chi/n_2 = 10$ are higher (~ 200 K) than is typically observed near the solar neighborhood (Heiles & Troland 2003). And finally, the Wolfire et al (2003) results suggest that along the line of sight to W49N, the average $\chi/n_2 \sim 4$. A similar modeling of the case $\chi/n_2 = 1$, not shown in the figures, gives $\zeta_{crp}/n_2 = 2.5 \times 10^{-15}$ and $2.0 \times 10^{-15} \text{ s}^{-1}$ with $A_{Vt} = 0.16$ and 0.08 , respectively. Again, because of the high cosmic ray rates, the gas temperatures are high in these clouds (~ 150 K). In addition, these cosmic ray rates seem improbably high. This model is driven to high cosmic ray rates in part because otherwise (with low χ/n_2) the gas is cold, which reduces the rate that H^+ can charge exchange with O. Therefore, we finally conclude that our models suggest typical $A_{Vt} \sim 0.3$, $\chi/n_2 \sim 3$, and $\zeta_{crp}/n_2 \sim 6 \times 10^{-16} \text{ s}^{-1}$ for the $30 - 50 \text{ km s}^{-1}$ component, and $\zeta_{crp}/n_2 \sim 4 \times 10^{-16} \text{ s}^{-1}$ for the $50 - 78 \text{ km s}^{-1}$ component.

A better approach is to ask, “What distribution of cloud A_{Vt} or hydrogen nucleus column N through the cloud will we encounter in traversing the ~ 11 kpc to W49N?” HI 21 cm observational data suggest that $dn_{cl}/dN \propto N^{-2}$, where n_{cl} is the number of clouds for $N \gtrsim 2.6 \times 10^{20} \text{ cm}^{-2}$, and proportional to N^{-1} for $N \lesssim 2.6 \times 10^{20} \text{ cm}^{-2}$ (Heiles & Troland 2005).¹² We have crudely integrated a distribution of clouds with this dependence, with the constant of proportionality derived by requiring the integral to obtain a total column of $N(\text{H}) = 7 \times 10^{21} \text{ cm}^{-2}$, the observed atomic H column in each velocity component of W49N. We use $N = 6 \times 10^{21} \text{ cm}^{-2}$ as an upper limit for the integration; above this, we enter small number statistics since the total column is of this order. The lower limit does not enter the integration significantly, as long as it is $\ll 2.6 \times 10^{20} \text{ cm}^{-2}$, since these clouds contain very little of the total column of any species. The integration removes A_{Vt} as a variable, and leaves only the parameters ζ_{crp}/n_2 and χ/n_2 as free parameters to match the observed $\text{OH}^+/\text{H}_2\text{O}^+$ ratio and the total column of OH^+ . We find that with $\chi/n_2 = 3.16$ and $\zeta_{crp}/n_2 = 3.7 \times 10^{-16} \text{ s}^{-1}$, we obtain $N(\text{OH}^+) \simeq 2.1 \times 10^{14} \text{ cm}^{-2}$ and $N(\text{H}_2\text{O}^+) \simeq 2.4 \times 10^{13} \text{ cm}^{-2}$. These values match the velocity interval $50 - 78 \text{ km s}^{-1}$ extremely well. Increasing the cosmic ray rate to $\zeta_{crp}/N_2 = 6.3 \times 10^{-16} \text{ s}^{-1}$, we obtain $N(\text{OH}^+) \simeq 3.6 \times 10^{14} \text{ cm}^{-2}$ and $N(\text{H}_2\text{O}^+) \simeq 4.0 \times 10^{13} \text{ cm}^{-2}$, a very good fit to the lower velocity component. Considering the small number statistics, especially of the higher A_{Vt} clouds, this is very good agreement. Interestingly, the main contribution to $N(\text{OH}^+)$ comes from near $A_{Vt} = 0.2 - 0.6$. This is because of the dependence of $N(\text{OH}^+)$ on A_{Vt} (see Figure 10). Note that $N(\text{OH}^+)$ rises sharply with A_{Vt} until about $A_{Vt} = 0.3$, and then it levels off. Therefore, the integral is weighted to that size cloud in the range of the turnover ($A_{Vt} \sim 0.3 - 0.6$), which has the peak OH^+ abundance (averaged through the cloud). In addition, the cloud distribution steepens when $A_{Vt} > 0.13$, thereby decreasing the contribution from higher A_{Vt} clouds. The total number of clouds in the range $A_{Vt} \simeq 0.1 - 1$ is approximately 20. We note that the H_2O^+ columns have greater contribution from higher A_{Vt} clouds, which are less numerous, and therefore we predict the H_2O^+ absorption feature to have greater fluctuations.

¹²Recall that N is the column of H nuclei; however, in the above range, generally $N \simeq N(\text{H})$.

We next examine the cases $\chi/n_2 = 1$ and 10. Assuming $\chi/n_2 = 10$, we find that we need cosmic ray rates of $1.1 \times 10^{-15} \text{ s}^{-1}$ and $7 \times 10^{-16} \text{ s}^{-1}$ to match the OH^+ columns in the two velocity components, respectively. However, the $\text{OH}^+/\text{H}_2\text{O}^+$ column ratio is 12.1, somewhat higher than observed, and again, the clouds are too warm ($\sim 200 \text{ K}$). The high field pushes the peaks of OH^+ and H_2O^+ deeper into the cloud, and our clouds tend to truncate the H_2O^+ column, leading to the high $\text{OH}^+/\text{H}_2\text{O}^+$ ratio. We need much higher cosmic ray rates than our solution above for $\chi/n_2 = 10$ with clouds of single $A_{Vt} \sim 0.7$ because the cloud distribution leads to a significant column of H from clouds of low A_{Vt} which have very little OH^+ . Assuming $\chi/n_2 = 1$, we find that we need cosmic ray rates of $2 \times 10^{-15} \text{ s}^{-1}$ and $1.2 \times 10^{-15} \text{ s}^{-1}$ to match the OH^+ columns in the two velocity components, respectively. However, the $\text{OH}^+/\text{H}_2\text{O}^+$ column ratio is 5.6, lower than observed. With low χ/n_2 , the clouds tend to contain both OH^+ and H_2O^+ peaks, driving the ratio down. We conclude that the best fit is with $\chi/n_2 = 3.16$, giving $\zeta_{crp}/n_2 \sim 6 \times 10^{-16} \text{ s}^{-1}$ and $4 \times 10^{-16} \text{ s}^{-1}$ for the two velocity components, in good agreement with our analysis above that did not use the cloud distribution. However, the cloud distribution gives added weight to the conclusion that $\chi/n_2 \sim 3$.

The cosmic ray rates derived from our models are roughly 2-4 times larger than those inferred by N10, who used a simple analytic treatment to infer cosmic ray ionization rates of 0.6 and $1.2 \times 10^{-16} (n_2/\epsilon) \text{ s}^{-1}$, where ϵ is the fraction of cosmic-ray ionizations that lead to OH^+ . Using pure gas-phase model results from the Meudon PDR code (Le Petit et al. 2006), N10 found that ϵ lay in the range 0.5 – 1.0 for a wide variety of cloud conditions; this would imply cosmic ray ionization rates in the range $\sim 0.6 - 2.4 \times 10^{-16} n_2 \text{ s}^{-1}$ for the material along the sight-line. The main source of the difference between our models and those of N10 is our inclusion of $\text{PAH}^- - \text{H}^+$ recombination and the charge exchange of H^+ with neutral PAH in the present work, processes – previously omitted – that reduce the fraction of cosmic-ray ionizations that lead to OH^+ production (in our models $\epsilon \sim 0.1 - 0.3$ in the regions where most of the OH^+ lies).

Figures 16 and 17 repeat Figures 14 and 15 except that the rates of PAH and PAH^- neutralization of H^+ have been reduced by > 4 , so that they are negligible compared to the radiative recombination of H^+ with electrons (see Appendix B). Note that this reduction could be achieved by either lower PAH abundances or lower PAH rate coefficients with H^+ , or a combination of both. Another possibility is increased photoionization rates of PAH^- and PAH. Figure 16 shows that the best fit to the data for $\chi/n = 3.16$ is $A_{Vt} \sim 0.316$ and $\zeta_{crp}/n_2 \sim 1 - 2 \times 10^{-16} \text{ s}^{-1}$, in complete agreement with N10. Therefore, the PAH chemistry is extremely important in deriving cosmic ray rates from the OH^+ and H_2O^+ ions. We consider the rates from Figures 16 and 17 lower limits to the cosmic ray rates, whereas the rates from Figures 14 and 15 could be considered upper limits, although they represent our best estimates of PAH chemistry at this time.

The cosmic-ray ionization rates suggested by the predictions shown in Figure 14 are also a factor $\sim 5 - 10$ larger than those typically inferred from observations of H_3^+ in the Galactic disk (Indriolo et al. 2007, Indriolo & McCall 2012). Indriolo & McCall conclude, however, that cosmic ray rates vary by more than an order of magnitude over various sight lines, from $\zeta_{crp} \sim 0.7 \times 10^{-16}$

s^{-1} to $4.6 \times 10^{-16} \text{ s}^{-1}$, with a mean of $\sim 1.5 \times 10^{-16} \text{ s}^{-1}$ (note that we have converted their total ionization rate per H_2 to our primary ionization rate per H nucleus by dividing their values by 2.3; we also note that their typical density was $n \sim 200 \text{ cm}^{-3}$ so their results imply ζ_{crp}/n_2 that are two times smaller than these values. Their highest values of ζ_{crp}/n_2 are still a factor of ~ 2 below what we find for W49N, so there appears to be a small discrepancy. We point out that the cosmic ray rate derived from H_3^+ observations is directly proportional to the assumed electron abundance. Indriolo & McCall assumed that the electrons were supplied by C^+ , with an abundance of 1.5×10^{-4} . However, in our models of diffuse clouds, where typically the gas density is $\sim 100 \text{ cm}^{-3}$, the cosmic ray ionization of H can produce comparable or greater abundances of H^+ than C^+ . Therefore, we find for $\zeta_{crp}/n_2 = 2 \times 10^{-16} \text{ s}^{-1}$, for example, that $x_e \simeq 3 \times 10^{-4}$ when $x(\text{H}_2) \simeq 0.1$ and $x_e \simeq 2 \times 10^{-4}$ when $x(\text{H}_2) \simeq 0.4$. This implies that the Indriolo et al rates may need to be increased, by factors as much as ~ 2 , depending on ζ_{crp}/n_2 . Given the small number of sources toward which $N(\text{OH}^+)/N(\text{H}_2\text{O}^+)$ and $N(\text{OH}^+)/N(\text{H})$ ratios have so far been reported, the proven variation in cosmic ray rates along different lines of sight, the lack of a common sight line to compare the cosmic ray rates derived by H_3^+ versus by OH^+ and H_2O^+ , the possibility of higher electron abundances than assumed by Indriolo and coworkers, and the lack of certainty in PAH chemistry, it is not yet possible to draw firm conclusions about whether our results differ significantly from that of Indriolo et al. What is clear is that cosmic ray rates in the diffuse ISM are higher than was previously thought.

Herschel has also detected absorption by H_3O^+ in foreground material along the sight-line to G10.6 – 0.4 (Gerin et al. 2010). The *average* $\text{H}_3\text{O}^+/\text{H}_2\text{O}^+$ ratio along the sight-line is 0.7, but the distribution of H_3O^+ is clearly different from that of H_2O^+ and OH^+ , with the H_3O^+ concentrated within a single narrow velocity component where the H_2 fraction is presumably largest. This cloud is unassociated with the source, but is probably the foreground cloud with the largest A_V along the line of sight. It appears in the HF spectrum (Neufeld et al. 2010) and CO spectrum (C. Vastel, private communication; see also Corbel & Eikenberry 2004), suggesting a high molecular fraction and therefore substantial A_V . The H_3O^+ column in this narrow component is $\sim 1 - 2 \times 10^{13} \text{ cm}^{-2}$, consistent with our predictions for the second peak in a high A_V cloud.

4.2. H_3O^+ Emission from Dense Galactic Molecular Clouds

PvDK92 searched for the 396, 364, and 307 GHz inversion-rotation lines of H_3O^+ in 20 Galactic targets – including GMCs, star forming regions, Galactic center sources and a few evolved stars – and reported definitive detections of H_3O^+ emission from the G34.3+0.15 hot core, two positions in Sgr B2 (a Galactic center GMC), and the W3 IRS5, W3(OH), W51M and Orion KL high-mass star forming regions. In the case of Orion and Sgr B2, H_3O^+ emissions had been previously discovered by Wootten et al. (1991). The H_3O^+ column densities derived by PvDK92 for the high-mass cores W3 IRS5, W3(OH), W51M are fairly similar, ranging from a few $\times 10^{13}$ to a few $\times 10^{14} \text{ cm}^{-2}$, and arguing for a similar environment and formation mechanism. Given the large critical

densities for the observed transitions, PvdK92 inferred relatively high densities ($n > 10^6 \text{ cm}^{-3}$) and temperatures ($T > 50 \text{ K}$) for the H_3O^+ emitting gas. The H_3O^+ column densities observed in these high-mass cores are in good agreement with the predictions of our models for either the case in which PAHs and/or very small grains are assumed to be present or the case where PAHs and low ionization potential metals are highly depleted¹³); the PAH case predicts H_3O^+ column densities of $3 \times 10^{13} - 10^{14} \text{ cm}^{-2}$, regardless of density n or ζ_{crp} .

Herschel’s HIFI instrument has allowed the detection of far-infrared and submillimeter H_3O^+ lines that are not accessible to ground-based observatories. Several H_3O^+ emission lines in the THz domain have been reported towards high-mass YSOs in the W3 IRS5 region (Benz et al. 2010). A rotation diagram combining HIFI data with lower frequency data from PvdK92 indicates a rotational temperature $T_{rot} \sim 239 \text{ K}$, suggesting that the observed emission may arise either from hot and dense gas or is radiatively excited by continuum photons from hot dust grains. Benz et al. (2010) inferred $N(\text{H}_3\text{O}^+) = 8.5 \pm 2 \times 10^{13} \text{ cm}^{-2}$ and interpreted the H_3O^+ emission as arising from the outflow walls heated and irradiated by the FUV radiation field from massive YSOs. Their inferred H_3O^+ column densities and rotational temperatures are consistent with our models of dense gas illuminated by a relatively strong FUV field (where large kinetic temperatures are achieved at relatively low $A_V \sim 1 - 2$).

4.3. Combined H_3O^+ Emission and Absorption in Strong Far-infrared Continuum Sources

For sources where a strong infrared radiation field is present, submillimeter H_3O^+ line emission can be accompanied by far-infrared absorption within an extended envelope. The H_3O^+ $J_K=2_1^- - 1_1^+$ and $2_0^- - 1_0^+$ inversion-rotation and $1_1^- - 1_1^+$ pure-inversion FIR absorption lines at 100.577, 100.869 and 181.054 μm were detected by ISO towards the optically thick FIR continuum emission of Sgr B2 (Goicoechea & Cernicharo 2001). An H_3O^+ column density of $\sim 1.6 \times 10^{14} \text{ cm}^{-2}$ was inferred in the warm and low density extended envelope of Sgr B2 ($n = 10^3 - 10^4 \text{ cm}^{-3}$, $\chi = 10^3 - 10^4$ from [OI] and [CII] observations; Goicoechea et al. 2004). However, the p- H_3O^+ $3_2^+ - 2_2^-$ 364 GHz emission line was subsequently mapped around the Sgr B2(M) core at 18'' angular resolution with APEX by van der Tak et al. (2006), who inferred column densities $\sim 10^{15} - 10^{16} \text{ cm}^{-2}$ on the basis of a detailed excitation model. This value is much larger than the estimates obtained from FIR absorption lines, presumably because the latter only probe the outer envelope of the source whereas the submillimeter observations probe material to a much larger depth. The H_3O^+ column densities inferred by van der Tak et al. (2006) are much larger than our model predictions

¹³If PAHs and very small grains coagulate into larger aggregates deeper inside the cloud (e.g., Boulanger et al. 1990; Rapacioli et al. 2006) or onto larger grain surfaces, our models would predict H_3O^+ column densities that are roughly an order of magnitude lower than the values inferred from the above observations, unless low ionization potential metal atoms are highly depleted at the second peak of H_3O^+ .

for externally-illuminated clouds; this discrepancy likely reflects the presence of a strong internal luminosity source in Sgr B2 that heats the dust grains within the interior and prevents the freeze-out of oxygen nuclei (see Appendix C).

4.4. Extragalactic, OH^+ , H_2O^+ and H_3O^+

Thanks to the much improved sensitivity of space- and ground-based receivers and detectors, molecular ions can now be detected outside the Milky Way. Extragalactic H_3O^+ was first detected through JCMT observations of the p- H_3O^+ 364 GHz emission line towards the prototypical ultraluminous infrared galaxy Arp 220, and towards M82, an evolved starburst (van der Tak et al. 2008). H_3O^+ was subsequently detected towards IC342, NGC253, NGC1068, NGC4418 and NGC 6240, and upper limits obtained towards IRAS 15250 and Arp 299 galaxies (Aalto et al. 2011). Except for IC342 and M82, the typical H_3O^+ column densities ($\sim 10^{15} - 10^{16} \text{ cm}^{-2}$) derived from extragalactic H_3O^+ detections are much larger than the predictions of our models for single clouds. These observations are of H_3O^+ in emission and the authors assume $T_{ex} \sim T_{rad}$ to obtain these columns with error bars of factor of 2. As in the case of Sgr B2, the discrepancy between our models and the observations may reflect the effect of enhanced dust temperatures that prevent the freeze-out of elemental oxygen. Alternatively, there may be a large number of clouds along the line of sight,

For the starburst galaxies M82 and IC342, however, where H_3O^+ column densities ($\sim 10^{14} \text{ cm}^{-2}$) are inferred from the observations, enhanced dust temperatures or ionization rates are not apparently required. For example, van der Tak et al (2008) inferred $N(\text{H}_3\text{O}^+) \simeq 1.1 \times 10^{14} \text{ cm}^{-2}$ in M82 from an emission line which contained a combination of a broad ($\Delta v \sim 260 \text{ km s}^{-1}$) and a narrow ($\Delta v \sim 40 \text{ km s}^{-1}$) component. In addition, a recent *Herschel*/HIFI detection (Weiss et al. 2010) of the o- H_2O^+ $1_{11} - 0_{00}$ ground-state line in absorption towards M82 revealed $N(\text{H}_2\text{O}^+) \simeq 2.9 \times 10^{14} \text{ cm}^{-2}$, arising from a $\Delta v \simeq 77 \text{ km s}^{-1}$ feature. The large width of the lines suggest numerous clouds in the beam. Overall, these numbers are consistent with our models with the H_2O^+ arising from the first (and possibly second) peak of numerous relatively low density clouds, whereas the H_3O^+ arises from the second peaks of many molecular clouds in the beam.

5. Summary and Conclusions

We model the production of OH^+ , H_2O^+ , and H_3O^+ in interstellar clouds, using a steady state photodissociation region code that treats the freeze-out of gas species, grain surface chemistry, and desorption of ices from grains. The code includes PAHs, which have an important effect on the chemistry.

As a function of depth or A_V into a molecular cloud, the ions tend to have two peaks, one at low $A_V \lesssim 1$ and one at high $A_V \sim 6$, the exact value depending on χ/n . In the first peak the

ions are created by the cosmic ray ionization of H to H^+ , followed by reactions with O and H_2 (see Figure 1 top). These peaks appear on the surfaces of molecular clouds as well as in diffuse clouds. PAHs can lower the production of the ions here, by neutralizing H^+ and interrupting the reaction chain (Figure 1 top). At most, they depress the ion abundances and columns by a factor of ~ 3 .

In molecular clouds a significant fraction of the column density of OH^+ and H_2O^+ is found in the first peak at the surface ($A_V < 1$) of the cloud. For relatively low values of the incident far ultraviolet flux on the cloud ($\chi \lesssim 1000$), the columns of OH^+ and H_2O^+ scale as the cosmic ray ionization rate divided by the gas density. Roughly, the columns of OH^+ , H_2O^+ , and H_3O^+ in the first peak are $2.2 \times 10^{12} \chi^{1/3} (\zeta_{crp}/2 \times 10^{-16} \text{ s}^{-1}) (100 \text{ cm}^{-3}/n) \text{ cm}^{-2}$, $1.5 \times 10^{12} \chi^{1/4} (\zeta_{crp}/2 \times 10^{-16} \text{ s}^{-1}) (100 \text{ cm}^{-3}/n) \text{ cm}^{-2}$, and $9 \times 10^{11} \chi^{1/3} (\zeta_{crp}/2 \times 10^{-16} \text{ s}^{-1}) (100 \text{ cm}^{-3}/n) \text{ cm}^{-2}$.

There is a second peak in OH^+ , H_2O^+ , and H_3O^+ abundances at larger depths ($A_V \sim 6$) in molecular clouds, when the second route to OH^+ formation, initiated by the cosmic ray ionization of H_2 becomes dominant (Figure 1 bottom). Here, lower electron abundances enhance the abundances of the ions by lowering the electronic recombination rate of H_3^+ (which raises the abundance of H_3^+ and the formation rates of the three ions), and by lowering the electronic recombination of H_3O^+ (its main destruction path). However, even deeper in the cloud, the oxygen freezes out as water ice on the grain surfaces, and the ion abundances fall as their formation rates fall, being starved for gas phase elemental oxygen. If PAHs or VSGs are present at these high values of $A_V \sim 6$, the electron abundance at the second peak is controlled by association with neutral PAH or VSG. In this case, rather surprisingly, the column of H_3O^+ ($\sim 4 \times 10^{13} \text{ cm}^{-3}$) in the second peak and the peak abundance ($\sim 10^{-8}$) of H_3O^+ is independent of both ζ_{crp} and n . Raising the cosmic ray ionization rate increases the production rate of H_3O^+ , but it also increases the destruction rate by electrons by the same amount. If PAHs and VSGs are not present at high A_V , the column of H_3O^+ depends mainly on the gas phase abundance of elemental S, Si, Mg, and Fe at the second peak. If these abundances are low, $\lesssim 3 \times 10^{-8}$, then columns comparable to the PAH case are obtained. However, for higher abundances of the metals, the H_3O^+ column is reduced by a factor of roughly 10. The columns of OH^+ and H_2O^+ in the second peaks are usually of order of the columns in the first peaks.

The observed H_3O^+ columns of $\sim 4 \times 10^{13} \text{ cm}^{-2}$ seen in many dense Galactic molecular clouds therefore imply that either PAHs or VSGs are present deep in molecular clouds or that the depletion of PAHs and VSGs are accompanied by a very significant depletion of gas phase metals. There are a few observations that imply much higher column ($\sim 10^{15} - 10^{16} \text{ cm}^{-2}$) of H_3O^+ , and these can only be explained in the context of our models as arising in very high A_V clouds where high gas phase elemental O abundances are present throughout due to either desorption processes or time dependent effects. We suspect that the grains in these sources may be so warm, $\gtrsim 100 \text{ K}$, that thermal desorption keeps water ice from depleting the oxygen reservoir. In the case of extragalactic sources with very broad velocity features, the columns may be increased by the presence of a large number of clouds along the line of sight.

For high values of the incident far ultraviolet flux ($\chi \gtrsim 1000$) and high gas densities ($\gtrsim 10^4 \text{ cm}^{-3}$), producing warm ($T > 300 \text{ K}$) gas with significant H_2 abundance at $A_V \sim 1 - 2$, chemical reactions initiated by the photoionization of carbon in the mainly atomic surface can form ionized hydrogen, which then leads to the formation of OH^+ , H_2O^+ , and H_3O^+ . In this case, their columns (typically, of order $3 \times 10^{13} \text{ cm}^{-2}$) are not related to the cosmic ray ionization rates. H_3O^+ emission from W3 IRS5 may be an example of such conditions.

We also model diffuse and translucent clouds in the interstellar medium, and show how observations of $N(\text{OH}^+)/N(\text{H})$ (typically $10^{-8} - 10^{-7}$) and $N(\text{OH}^+)/N(\text{H}_2\text{O}^+)$ (typically 3-15) can be used to estimate ζ_{crp}/n . The ratio $N(\text{OH}^+)/N(\text{H})$, which is essentially the average abundance of OH^+ in all the clouds along the line of sight (within the same absorption velocity component), is mainly a measure of ζ_{crp}/n . The ratio of the OH^+ column to the H_2O^+ column in diffuse clouds is mainly dependent on the ratio χ/n and A_{Vt} (i.e, the total hydrogen column through a single typical cloud). If χ/n is known, or at least constrained to a narrow range such as $\chi/n_2 \sim 3 - 6$ typical of diffuse clouds in random locations along the line of sight in the Galaxy, then observations of $N(\text{OH}^+)/N(\text{H})$, $N(\text{OH}^+)/N(\text{H}_2\text{O}^+)$, and $N(\text{OH}^+)$ can determine ζ_{crp}/n , A_{Vt} , and a geometrical factor which is a combination of the number of clouds along the line of sight and the typical angle that the line of sight makes as it passes through each diffuse cloud slab. Using the observed distribution of A_{Vt} in diffuse clouds, the models can provide an estimate of χ/n_2 .

We discuss the relation of our models to recent observations of OH^+ and H_2O^+ by the Herschel Space Observatory, and the ability to constrain the cosmic ray ionization rate through comparison of observations with these models. We conclude that the cosmic ray primary ionization rates ζ_{crp} in the observed foreground diffuse clouds towards W49N have values of approximately $\zeta_{crp} \sim 4 - 6 \times 10^{-16} (n/100 \text{ cm}^{-3}) \text{ s}^{-1}$, if our adopted PAH chemistry is correct.¹⁴ We find a hard lower limit of $\zeta_{crp}/n_2 \gtrsim 1 - 2 \times 10^{-16} \text{ s}^{-1}$ by neglecting PAH chemistry in W49N. Our best fit models suggest that $\chi/n_2 \sim 3$ in the diffuse clouds towards W49N. Our W49 models suggest that, in terms of producing OH^+ and H_2O^+ column, the typical $A_{Vt} \sim 0.3$ through a single cloud towards W49N. and that a diffuse cloud A_{Vt} distribution measured by Heiles & Troland (2005) fits the data very well. To produce the total column of OH^+ and H observed in the two velocity components requires ~ 20 clouds in each component along the line of sight. We discuss differences between our estimates and those of N10 and Indriolo et al (2007), pointing out the former neglected PAH chemistry and the latter may have slightly underestimated the electron abundance in the diffuse foreground clouds with the highest cosmic ray ionization rates. We look forward to further observations of OH^+ and H_2O^+ along many sight lines to probe the cosmic ray ionization rates throughout the Galaxy.

Acknowledgements

We would like to thank A. Benz, J.H. Black, E. Falgarone, B. Godard, C. Heiles, V. Ossenkopf, and E. van Dishoeck for many useful discussions. We especially thank M. Gerin, N. Indriolo, and

¹⁴We emphasize the need for further theoretical and laboratory work to investigate PAH reaction rates.

the anonymous referee for careful readings of the manuscript and many useful suggestions. We gratefully acknowledge the support of a grant from the NASA Herschel Science Center’s Theoretical Research/Laboratory Astrophysics Program. Partial support for MGW, MJK and DJH was provided by a NASA Long Term Space Astrophysics Grant NNG05G46G. JRG is supported by a Ramón y Cajal research contract and thanks the Spanish MICINN for funding support through grants AYA2009-07304 and CSD2009-00038.

Appendix A: Tables of rate coefficients and adopted abundances

Table 1 presents some of the key reactions and/or some of the reaction rates that have changed since H09. We emphasize that this is not a complete listing of the ~ 300 chemical reactions in the PDR code described in H09. The PAH rates are scaled by the factor Φ_{PAH} , a scaling factor introduced in Wolfire et al (2008) that incorporates the uncertainties in PAH reaction rates, PAH sizes, and PAH abundances. Wolfire et al (2008) found from a semi-empirical fit of our PDR models to C, C⁺, H, and H₂ column densities in diffuse clouds that $\Phi_{\text{PAH}} \sim 0.5$, and we have adopted that value in all of our PDR models.

Table 2 presents the standard gas phase abundances and grain properties that we have adopted in most of our PDR models. As discussed in the text, we have also run models with these values changed to test the sensitivity of the results to the standard values. In particular, we have run models with $x(\text{PAH})=0$; with $x(\text{Si})$, $x(\text{Fe})$, $x(\text{S})$, and $x(\text{Mg})$ all set to 10^{-8} or 10^{-5} ; and with $x(\text{O}) = 4.5 \times 10^{-4}$.

Table 1. Reaction Rates

Reaction	Rate Coefficient
$\text{PAH}^- + \text{H}^+ \rightarrow \text{PAH}^0 + \text{H}$	$8.1 \times 10^{-7} \Phi_{\text{PAH}} (T/300 \text{ K})^{-0.50} \text{ cm}^3 \text{ s}^{-1} \text{ a}$
$\text{PAH}^0 + \text{H}^+ \rightarrow \text{PAH}^+ + \text{H}$	$7.0 \times 10^{-8} \Phi_{\text{PAH}} \text{ cm}^3 \text{ s}^{-1} \text{ a}$
$\text{PAH}^+ + e \rightarrow \text{PAH}^0$	$3.4 \times 10^{-5} \Phi_{\text{PAH}} (T/300 \text{ K})^{-0.50} \text{ cm}^3 \text{ s}^{-1} \text{ a}$
$\text{PAH}^0 + e \rightarrow \text{PAH}^-$	$3.0 \times 10^{-6} \Phi_{\text{PAH}} \text{ cm}^3 \text{ s}^{-1} \text{ a}$
$\text{PAH}^- + \text{C}^+ \rightarrow \text{PAH}^0 + \text{C}$	$2.3 \times 10^{-7} \Phi_{\text{PAH}} (T/300 \text{ K})^{-0.50} \text{ cm}^3 \text{ s}^{-1} \text{ a,b}$
$\text{PAH}^0 + \text{C}^+ \rightarrow \text{PAH}^+ + \text{C}$	$2.0 \times 10^{-8} \Phi_{\text{PAH}} \text{ cm}^3 \text{ s}^{-1} \text{ a,b}$
$\text{PAH}^0 + h\nu \rightarrow \text{PAH}^+ + e$	$2.8 \times 10^{-8} \chi \exp(-2.34A_V) \text{ s}^{-1} \text{ c,d}$
$\text{PAH}^- + h\nu \rightarrow \text{PAH}^0 + e$	$5.7 \times 10^{-7} \chi \exp(-1.09A_V) \text{ s}^{-1} \text{ c,e}$
$\text{PAH}^0 + h\nu \rightarrow \text{PAH}^+ + e$	$3.5 \times 10^{-8} \chi \exp(-2.45A_V) \text{ s}^{-1} \text{ f,d}$
$\text{PAH}^- + h\nu \rightarrow \text{PAH}^0 + e$	$1.7 \times 10^{-7} \chi \exp(-1.77A_V) \text{ s}^{-1} \text{ f,e}$
$\text{C} + h\nu \rightarrow \text{C}^+ + e$	$3.1 \times 10^{-10} \chi \exp(-3.33A_V) \text{ s}^{-1} \text{ g}$
$\text{H}_2\text{O} + h\nu \rightarrow \text{H}_2\text{O}^+ + e$	$3.1 \times 10^{-11} \chi \exp(-3.90A_V) \text{ s}^{-1} \text{ g}$
$\text{H}_2\text{O} + h\nu \rightarrow \text{OH} + \text{H}$	$7.5 \times 10^{-10} \chi \exp(-1.70A_V) \text{ s}^{-1} \text{ g,h}$
$\text{H}_2\text{O} + h\nu \rightarrow \text{O} + \text{H}_2$	$4.8 \times 10^{-11} \chi \exp(-2.20A_V) \text{ s}^{-1} \text{ g,h}$
$\text{OH} + h\nu \rightarrow \text{O} + \text{H}$	$3.9 \times 10^{-10} \chi \exp(-1.70A_V) \text{ s}^{-1} \text{ g,h}$
$\text{OH} + h\nu \rightarrow \text{OH}^+ + e$	$2.2 \times 10^{-11} \chi \exp(-4.05A_V) \text{ s}^{-1} \text{ i}$
$\text{OH}^+ + h\nu \rightarrow \text{O}^+ + \text{H}$	$1.1 \times 10^{-11} \chi \exp(-3.50A_V) \text{ s}^{-1} \text{ g}$
$\text{CH}^+ + h\nu \rightarrow \text{H}^+ + \text{C}$	$3.3 \times 10^{-10} \chi \exp(-2.94A_V) \text{ s}^{-1} \text{ g}$
$\text{H} + \text{CR} \rightarrow \text{H}^+ + e$	$\zeta_{crp} \text{ s}^{-1} \text{ j}$
$\text{H}_2 + \text{CR} \rightarrow \text{H}_2^+ + e$	$2\zeta_{crp} \text{ s}^{-1} \text{ j}$
$\text{H}^+ + e \rightarrow \text{H}$	$3.5 \times 10^{-12} (T/300 \text{ K})^{-0.75} \text{ cm}^3 \text{ s}^{-1} \text{ k}$
$\text{H}_2^+ + e \rightarrow \text{H} + \text{H}$	$1.6 \times 10^{-8} (T/300 \text{ K})^{-0.43} \text{ cm}^3 \text{ s}^{-1} \text{ k,l}$
$\text{H}_3^+ + e \rightarrow \text{H}_2 + \text{H}$	$3.4 \times 10^{-8} (T/300 \text{ K})^{-0.50} \text{ cm}^3 \text{ s}^{-1} \text{ m}$
$\text{H}_3^+ + e \rightarrow \text{H} + \text{H} + \text{H}$	$3.4 \times 10^{-8} (T/300 \text{ K})^{-0.50} \text{ cm}^3 \text{ s}^{-1} \text{ m}$
$\text{OH}^+ + e \rightarrow \text{O} + \text{H}$	$3.8 \times 10^{-8} (T/300 \text{ K})^{-0.50} \text{ cm}^3 \text{ s}^{-1} \text{ k,l}$
$\text{H}_2\text{O}^+ + e \rightarrow \text{H}_2 + \text{O}$	$3.9 \times 10^{-8} (T/300 \text{ K})^{-0.50} \text{ cm}^3 \text{ s}^{-1} \text{ k}$
$\text{H}_2\text{O}^+ + e \rightarrow \text{OH} + \text{H}$	$8.6 \times 10^{-8} (T/300 \text{ K})^{-0.50} \text{ cm}^3 \text{ s}^{-1} \text{ k}$
$\text{H}_2\text{O}^+ + e \rightarrow \text{O} + \text{H} + \text{H}$	$3.1 \times 10^{-7} (T/300 \text{ K})^{-0.50} \text{ cm}^3 \text{ s}^{-1} \text{ k}$
$\text{H}_3\text{O}^+ + e \rightarrow \text{OH} + \text{H} + \text{H}$	$3.4 \times 10^{-7} (T/300 \text{ K})^{-0.74} \text{ cm}^3 \text{ s}^{-1} \text{ n}$
$\text{H}_3\text{O}^+ + e \rightarrow \text{H}_2\text{O} + \text{H}$	$1.4 \times 10^{-7} (T/300 \text{ K})^{-0.74} \text{ cm}^3 \text{ s}^{-1} \text{ n}$
$\text{H}_3\text{O}^+ + e \rightarrow \text{H}_2 + \text{OH}$	$7.9 \times 10^{-8} (T/300 \text{ K})^{-0.74} \text{ cm}^3 \text{ s}^{-1} \text{ n}$
$\text{H}_3\text{O}^+ + e \rightarrow \text{H}_2 + \text{O} + \text{H}$	$7.4 \times 10^{-9} (T/300 \text{ K})^{-0.74} \text{ cm}^3 \text{ s}^{-1} \text{ n}$
$\text{H}_3^+ + \text{CO} \rightarrow \text{HCO}^+ + \text{H}_2$	$1.7 \times 10^{-9} \text{ cm}^3 \text{ s}^{-1} \text{ k}$

Table 1—Continued

Reaction	Rate Coefficient
$C^+ + e \rightarrow C + h\nu$	^o
$C^+ + OH \rightarrow CO^+ + H$	$2.9 \times 10^{-9} (T/300 \text{ K})^{-0.33} \text{ cm}^3 \text{ s}^{-1} \text{ p}$
$C^+ + H_2 \rightarrow CH^+ + H$	$1.0 \times 10^{-10} \exp(-T/4640 \text{ K}) \text{ cm}^3 \text{ s}^{-1} \text{ k}$
$CO^+ + H \rightarrow CO + H^+$	$7.5 \times 10^{-10} \text{ cm}^3 \text{ s}^{-1} \text{ k}$
$O + H^+ \rightarrow O^+ + H$	^q
$O + H \rightarrow OH + h\nu$	$9.9 \times 10^{-19} (T/300 \text{ K})^{-0.38} \text{ k}$
$O^+ + H \rightarrow H^+ + O$	$5.7 \times 10^{-10} (T/300 \text{ K})^{-0.36} e^{8.6 \text{ K}/T} \text{ cm}^3 \text{ s}^{-1} \text{ q}$
$O^+ + H_2 \rightarrow OH^+ + H$	$1.7 \times 10^{-9} \text{ cm}^3 \text{ s}^{-1} \text{ k}$
$OH^+ + H_2 \rightarrow H_2O^+ + H$	$1.0 \times 10^{-9} \text{ cm}^3 \text{ s}^{-1} \text{ k}$
$H_2O^+ + H_2 \rightarrow H_3O^+ + H$	$6.4 \times 10^{-10} \text{ cm}^3 \text{ s}^{-1} \text{ k}$
$H_2^+ + H_2 \rightarrow H_3^+ + H$	$2.1 \times 10^{-9} \text{ cm}^3 \text{ s}^{-1} \text{ k}$
$H_3^+ + O \rightarrow OH^+ + H_2$	$8.4 \times 10^{-10} \text{ cm}^3 \text{ s}^{-1} \text{ k}$
$H_3^+ + O \rightarrow H_2O^+ + H$	$3.6 \times 10^{-10} \text{ cm}^3 \text{ s}^{-1} \text{ k}$
$H_2 + O \rightarrow OH + H$	$3.40 \times 10^{-13} (T/300 \text{ K})^{2.67} \exp(-T/3160 \text{ K}) \text{ cm}^3 \text{ s}^{-1} \text{ k}$

H_2O^+ has no photodissociation channels longward of 13.61 eV and the rate is set to zero (van Dishoeck et al. 2006).

^aNon-photo PAH rates are calculated using the equations of Draine & Sutin (1987). Representative rates are given at $T = 300 \text{ K}$ for disk PAHs. $\Phi_{\text{PAH}} = 0.5$ from Wolfire et al. (2008).

^bAdditional collisional rates scale as $(m)^{-0.5}$ where m is the mass of the collision partner.

^c χ is the FUV field measured in units of the Draine (1978) field. Rate for $N_C = 100$. The shape of the FUV and optical field from Mathis et al. (1983) used for $\chi = 1$.

^dAbsorption cross section and ionization potential of circumovalene (IP=5.7 eV; Mallocci et al. 2007), and linear yield function (Jochims et al. 1996).

^eAbsorption cross section and electron affinity of circumovalene (EA=1.9 eV; Mallocci et al. 2007), and maximum yield ($Y = 1$).

^f χ is the FUV field measured in units of the Draine (1978) field. Rate for $N_C = 100$. FUV and optical field using a $T = 30,000 \text{ K}$ blackbody used for $\chi > 1$.

^gvan Dishoeck et al. (2006) except for the attenuation factors for H_2O and OH photodissociation. Here we adopt Roberge et al (1991), see footnote h, because otherwise the models overproduce these molecules and O_2 at the second peak compared with observations (see H09).

^h<http://www.strw.leidenuniv.nl/ewine/photo/index.php?file=pd.php>, Roberge et al (1991)

ⁱRate for assumed cross-section of 1×10^{-17} cm² and threshold of 957 Å. Depth dependence from van Dishoeck (1988) for a molecule with a photoionization threshold wavelength of 950 Å.

^j ζ_{crp} is the primary cosmic-ray ionization rate per hydrogen nucleus. Various rates are investigated in this paper. The total rate including secondary ionizations is from Dalgarno et al. (1999).

^kUDFA06

^lBrian & Mitchell (1990)

^mMcCall et al. (2004)

ⁿP. Goldsmith 2011 private communication using mean total rate from Neau et al. (2000) and Jensen et al. (2000) of 5.7×10^{-7} cm³ s⁻¹; branching ratios from Jensen et al. (2000)

^oDielectronic plus radiative recombination rates from Badnell et al. (2003) and Badnell (2006).

^pOSU_01_2009 rate tables; <http://www.physics.ohio-state.edu/~eric/research.html>

^qState-specific rates from Stancil et al. (1999)

Table 2. Gas Phase Abundances and Grain Properties

Species	Symbol	Value	^a Ref
Carbon	$x(\text{C})$	1.6×10^{-4}	b
Oxygen	$x(\text{O})$	3.2×10^{-4}	c
Silicon	$x(\text{Si})$	1.7×10^{-6}	d
Iron	$x(\text{Fe})$	1.7×10^{-7}	d
Sulfur	$x(\text{S})$	2.8×10^{-5}	d
Magnesium	$x(\text{Mg})$	1.1×10^{-6}	d
PAHs	$x(\text{PAH})$	2.0×10^{-7}	e
Grain Area	σ_{H}	2×10^{-21}	f

^aGas-phase abundances per hydrogen nucleus.

^bSofia et al. (2004)

^cMeyer et al. (1998)

^dSavage & Sembach (1996) cool diffuse cloud towards ζ Oph

^eAbundance from Wolfire et al. (2003) modified for $N_{\text{C}} = 100$ planar PAHs. This abundance gives a total number of C in PAHs of 2×10^{-5} per hydrogen or $\sim 6\%$ of C in PAHs.

^fUnits cm^2 per hydrogen; Hollenbach et al. (2009)

Appendix B: Simple Analytic Analysis of the Results

The results in §3.1 and §3.2 can be understood by a simple analytic chemical model that incorporates the main physics. Such a model, though approximate, has the advantage of allowing one to determine and understand the sensitivity to various model parameters, and serves to validate the numerical model.

Analytic solution to $x(\text{OH}^+)$ and ϵ in the first peak ($A_V < 1$). The top panel of Figure 1 describes the main chemical pathways to OH^+ for $A_V < 1$, and Table 1 lists the rate coefficients used for each of these reactions. Figure 1 omits the formation of OH^+ by the photoionization of OH, which is only important at very low $A_V \lesssim 0.01$ and never dominates the production of the column of OH^+ for clouds of higher A_V . This minor route produces OH by the reactions $\text{O} + \text{H}_2$ (vibrationally excited), $\text{O} + \text{H}$, and the formation of water ice on grains followed by desorption leading to OH. The photoionization of OH leads to a constant (low) OH^+ abundance at the cloud surface. We also neglect that route in the analytic solution, as it does not affect the peak abundance of OH^+ , nor the values of ϵ near the peak. In addition, we approximate ϵ for this peak by only including the rate of formation of OH^+ by the reaction $\text{H}_2 + \text{O}^+ \rightarrow \text{OH}^+ + \text{H}$.

In the following we use rate coefficients from Table 1 with two exceptions. The Stancil et al (1999) rate coefficients for the reaction of H^+ with O and its reverse reaction are complicated, and we simplify them here, focussing on results for low density clouds. We set $\gamma_1 = 4 \times 10^{-10} \exp(-230 \text{ K}/T) \text{ cm}^3 \text{ s}^{-1}$ as the rate coefficient for the reaction $\text{H}^+ + \text{O} \rightarrow \text{O}^+ + \text{H}$, and $\gamma_2 = 4 \times 10^{-10} \text{ cm}^3 \text{ s}^{-1}$ as the rate coefficient for the reaction $\text{O}^+ + \text{H} \rightarrow \text{H}^+ + \text{O}$. Let γ_3 be the rate coefficient for the reaction $\text{H}_2 + \text{O}^+ \rightarrow \text{OH}^+ + \text{H}$; α_e the rate coefficient for the recombination of H^+ with electrons; α_{P^-} the rate coefficient for the neutralization of H^+ by PAH^- ; and α_P the rate coefficient for the charge exchange of H^+ with PAH. Let $x(\text{H}_2)$ be the abundance of H_2 with respect to H nuclei, x_e the abundance of electrons, $x(\text{PAH})$ the abundance of neutral PAHs, $x(\text{PAH}^-)$ the abundance of PAH^- , and x_O the gas phase elemental abundance of O. The solution to ϵ , the efficiency of making OH^+ from cosmic rays, is then:

$$\epsilon = \frac{1}{1 + y}, \quad (1)$$

where the parameter y is given:

$$y = \frac{[\gamma_2 + \gamma_3 x(\text{H}_2)] [\alpha_e x_e + \alpha_{P^-} x(\text{PAH}^-) + \alpha_P x(\text{PAH})]}{\gamma_1 \gamma_3 x_O x(\text{H}_2)}. \quad (2)$$

We utilized the fact that ϵ approaches unity when $y < 1$ to set the condition in §3.1.1 (Eq. 1) on the abundances of O, H_2 , electrons, PAHs and PAH^- s which lead to $\epsilon \sim 1$. One can immediately see that for low values of $x(\text{H}_2)$, where $y > 1$, ϵ is proportional to $x(\text{H}_2)$. Here, the dominant route of H^+ destruction is by recombination with electrons, PAHs, and PAH^- s. The small fraction of the H^+ created by cosmic rays that charge exchanges with O to form O^+ that then reacts with H_2 to form OH^+ is proportional to the H_2 abundance. Substituting likely values of $x_e \sim 3 \times 10^{-4}$

(we focus on cases with high ζ_{crp}/n_2 and here H^+ as well as C^+ contribute electrons-see Figure 4), $x(\text{PAH}) \sim 1.85 \times 10^{-7}$, $x(\text{PAH}^-) \sim 1.5 \times 10^{-8}$, and $x_{\text{O}} \sim 3.2 \times 10^{-4}$, we obtain

$$\epsilon \simeq \frac{227e^{-2.3/T_2}x(\text{H}_2)}{[1 + 4.25x(\text{H}_2) \left[\left(\frac{x_e}{3 \times 10^{-4}} \right) T_2^{-0.75} + 4.4 \left(\frac{x(\text{PAH}^-)}{1.5 \times 10^{-8}} \right) T_2^{-0.5} + 2.7 \left(\frac{x(\text{PAH})}{1.85 \times 10^{-7}} \right) \right]]}, \quad (3)$$

where $T_2 \equiv T/100$ K. For low values of $x(\text{H}_2) \ll 0.2$, and standard values of x_e , $x(\text{PAH})$ and $x(\text{PAH}^-)$, this becomes

$$\epsilon \simeq 28e^{-2.3/T_2}x(\text{H}_2). \quad (4)$$

For higher values of $x(\text{H}_2) \gg 0.2$, ϵ saturates at values near unity, as nearly every cosmic ray ionization leads to a production of OH^+ . With standard values of x_e , $x(\text{PAH})$ and $x(\text{PAH}^-)$ Equation (3) then becomes

$$\epsilon \simeq \frac{1}{1 + 0.15e^{2.3/T_2}}. \quad (5)$$

These formulae are very good fits to the results seen in Figures 4 and 6. Note, however, that they are only valid for $x(\text{H}_2) \ll 0.5$, since we have implicitly assumed $x(\text{H}) \gg x(\text{H}_2)$.

Equation (3) shows that PAH^- in particular can lower ϵ by neutralizing H^+ . We emphasize that equations (3-5) are valid only if the PAH and PAH^- rate coefficients we have adopted in Table 1 are valid. Equations (4-5) assume the standard PAH and PAH^- abundances given above.

Rather than a simple saturated value of ϵ at high $x(\text{H}_2)$, however, we see in the figures that the first peak in OH^+ shows a value of ϵ that peaks and then falls with increasing depth, once most of the gas is H_2 . This is because once the gas is more than half molecular ($x(\text{H}_2) > 0.25$), the cosmic ray ionization is mostly of H_2 , which we have not included in the analytic treatment. The route to OH^+ via the ionization of H_2 is not as efficient at the surface, because of the high abundance of electrons which react quickly with H_3^+ . Thus, as $x(\text{H})$ declines deeper into the cloud, the value of ϵ falls with increasing A_V .

The analytic equation for $x(\text{OH}^+)$ requires the addition of reactions of OH^+ with electrons and H_2 that destroy OH^+ . Let γ_4 be the rate coefficient for the destruction of OH^+ by H_2 , and γ_5 be the coefficient for destruction by electrons. Then, we find

$$x(\text{OH}^+) = \frac{(\zeta_{crt}/n)\epsilon}{\gamma_4x(\text{H}_2) + \gamma_5x_e}. \quad (6)$$

Here, $\zeta_{crt} \sim 1.5\zeta_{crp}$ is the total rate of cosmic ray ionization, including secondaries. Ignoring the photodissociation term, we can again scale to likely values of parameters to obtain

$$x(\text{OH}^+) \simeq \left[\frac{10^{-7} \epsilon}{\left(\frac{x_e}{3 \times 10^{-4}}\right) T_2^{-0.5} + 51x(\text{H}_2)} \right] \left(\frac{\zeta_{crt}}{10^{-16} \text{ s}^{-1}} \right) \left(\frac{100 \text{ cm}^{-3}}{n} \right). \quad (7)$$

Again, we can break this equation into two regimes. For $x(\text{H}_2) \ll 0.02(x_e/3 \times 10^{-4})T_2^{-0.5}$, OH^+ is mainly destroyed by dissociative recombination with electrons and the second term in the denominator can be ignored. Then, assuming standard parameters for the abundances of x_e , $x(\text{PAH})$, and $x(\text{PAH}^-)$, we obtain

$$x(\text{OH}^+) \simeq 2.1 \times 10^{-6} e^{-2.3/T_2} T_2^{0.5} x(\text{H}_2) \left(\frac{\zeta_{crt}}{10^{-16} \text{ s}^{-1}} \right) \left(\frac{100 \text{ cm}^{-3}}{n} \right). \quad (8)$$

However, if $0.02(x_e/3 \times 10^{-4})T_2^{-0.5} \ll x(\text{H}_2) < 0.2$, then H_2 mainly destroys OH^+ and, again using standard values for the parameters, we obtain the peak and plateau value of the OH^+ abundance:

$$x(\text{OH}^+) \simeq 4.1 \times 10^{-8} e^{-2.3/T_2} \left(\frac{\zeta_{crt}}{10^{-16} \text{ s}^{-1}} \right) \left(\frac{100 \text{ cm}^{-3}}{n} \right). \quad (9)$$

For higher values of $x(\text{H}_2) > 0.2$, the abundance of OH^+ declines as ϵ saturates, and as $x(\text{H})$ declines leading to the less efficient production of OH^+ initiated by cosmic ray ionization of H_2 . The column of OH^+ in the first peak can then be estimated

$$N(\text{OH}^+) \simeq 8 \times 10^{12} e^{-2.3/T_2} \left(\frac{\zeta_{crt}}{10^{-16} \text{ s}^{-1}} \right) \left(\frac{100 \text{ cm}^{-3}}{n} \right) (\Delta A_V / 0.1) \text{ cm}^{-2}, \quad (10)$$

where ΔA_V is the width of the peak region.

This shows the important result that the peak abundance (and approximately the column of OH^+ in the first peak) is proportional to ζ_{crt}/n . In order to find regions of high OH^+ column that can be observed, and where cosmic rays are the ultimate cause of the ions, we therefore must look at low density regions with high cosmic ray ionization rates.

Analytic solution to the second peak of H_3O^+ in the regime $A_V > 1$ and with PAHs present. Deeper in the cloud ($A_V > 1$) the dust and gas shield the FUV photons and carbon is no longer in the form of C^+ but converts to CO . Here, the electron abundance drops rapidly with depth, and the gas is almost entirely molecular so that the route to H_3O^+ is started with the cosmic ray ionization of H_2 . We then define $\epsilon(\text{H}_3\text{O}^+)$ so that the rate of formation of H_3O^+ per unit volume is $\zeta_{crt} n \epsilon(\text{H}_3\text{O}^+)$.¹⁵ Again $\epsilon(\text{H}_3\text{O}^+)$ is equivalent to the fraction of cosmic ray ionizations that lead to H_3O^+ .

Figure 1 shows the route to H_3O^+ from the ionization of H_2 . The key competition that determines $\epsilon(\text{H}_3\text{O}^+)$ revolves around H_3^+ . With all the hydrogen molecular, the routes via H_2

¹⁵ Note that if the total ionization rate per H is ζ_{crt} , then the total rate per H_2 is roughly $2\zeta_{crt}$. The cosmic ray ionization rate per unit volume is then $2\zeta_{crt} n(\text{H}_2) = \zeta_{crt} n$ in fully molecular zones.

dominate the rates via electrons. Thus, the only interruption in the chain that leads to H_3O^+ is the possibility that H_3^+ will react with either electrons or CO rather than with O to form either OH^+ or H_2O^+ . We then define γ_6 as the rate coefficient for H_3^+ reacting with O to form either OH^+ or H_2O^+ ; γ_7 is the rate coefficient for H_3^+ to dissociatively recombine with electrons; γ_8 is the rate coefficient for H_3^+ to react with CO; and γ_9 is the rate coefficient for H_3O^+ to dissociatively recombine with electrons (all channels). Therefore,

$$\epsilon(\text{H}_3\text{O}^+) \simeq \frac{\gamma_6 x(\text{O})}{\gamma_6 x(\text{O}) + \gamma_7 x_e + \gamma_8 s(\text{CO})} \quad (11)$$

The solution for the abundance of H_3O^+ follows

$$x(\text{H}_3\text{O}^+) = \frac{(\zeta_{crt}/n)\epsilon(\text{H}_3\text{O}^+)}{\gamma_9 x_e} \quad (12)$$

We find in our model runs that electrons are formed by the cosmic ray ionization of H_2 and destroyed by attachment to neutral PAHs. Most of the PAHs deep in the cloud are neutral, and therefore using a neutral PAH abundance of 2×10^{-7} we find

$$x_e \simeq 7.7 \times 10^{-6} (\zeta_{crt}/10^{-16} \text{ s}^{-1})(100 \text{ cm}^{-3}/n) \quad (13)$$

If either O or CO dominate the destruction of H_3^+ over electrons (or $x_e < 8 \times 10^{-3}x(\text{CO}) + 6 \times 10^{-3}x(\text{O})$), which we find is usually the case for most of our runs at the second peak of the H_3O^+ abundance, then we find, substituting x_e into the equation for $x(\text{H}_3\text{O}^+)$,

$$x(\text{H}_3\text{O}^+) \simeq \frac{4 \times 10^{-8} (T/30 \text{ K})^{0.74} x(\text{O})}{x(\text{O}) + 1.4x(\text{CO})} \quad (14)$$

At the peak, we generally find that most of the carbon is in CO, so $x(\text{CO}) \sim 1.6 \times 10^{-4}$ and that most of the remaining O is atomic, or $x(\text{O}) \sim 1.4 \times 10^{-4}$. Therefore, we predict a peak H_3O^+ abundance of

$$x_p(\text{H}_3\text{O}^+) \simeq 1.6 \times 10^{-8} (T/30 \text{ K})^{0.74} \quad (15)$$

This explains why the second peak abundance of H_3O^+ is independent of ζ_{crt} and n . The production rate per unit volume of H_3O^+ depends on $\zeta_{crt}n$ but the destruction rate per unit volume depends on $n^2 x_e$. Since electrons are formed by cosmic ray ionization and destroyed by PAHs, $x_e \propto \zeta_{crt}/n$. Therefore, both production and destruction of H_3O^+ is proportional to $\zeta_{crt}n$, and the resulting abundance of H_3O^+ is independent of both parameters. As one goes to higher A_V from the peak, the atomic O freezes out on grains as water ice, and thus the abundance of H_3O^+ declines. The thickness of the region of peak H_3O^+ abundance is therefore of order $\Delta A_V \sim 1$, or a hydrogen column of $2 \times 10^{21} \text{ cm}^{-2}$. Multiplying this by $x_p(\text{H}_3\text{O}^+)$, we estimate columns of H_3O^+ of $N(\text{H}_3\text{O}^+) \sim 4 \times 10^{13} \text{ cm}^{-2}$, as we found in our numerical runs. There has been some indication (Rimmer et al 2011)

that the cosmic ray ionization rate may decline with depth into a cloud. From the above result, this should have little consequence on the H_3O^+ column.

We should emphasize that this prediction is dependent on the presence of PAHs deep ($A_V \sim 5$) in the cloud. If PAHs coagulate on grain surfaces, then PAHs do not remove free electrons from the gas phase. In this case, the electron abundance at the peak of the H_3O^+ can be higher than in the PAH case if gas phase metal ions are present. This suppresses the H_3O^+ abundance at the peak. Therefore, the observation of high columns of H_3O^+ deep in molecular clouds may indicate either the presence of PAHs lowering the electron abundances there, or, in the absence of PAHs, may indicate a high depletion of gas phase metals at the second peak.

Appendix C: Sensitivity of results to other parameters

Recently, Klippenstein et al (2010) have provided theoretical rate coefficients for the reactions of H_3^+ with O and with CO that are 10 to 20% higher than the rate coefficients we adopted. We have run our standard cases with these new coefficients and find that the columns of OH^+ , H_2O^+ , and H_3O^+ increase by roughly 10% with the new coefficients. In addition, Cartledge et al (2004) suggest a gas phase oxygen abundance of 2.84×10^{-4} , whereas Jensen et al (2005) suggest a value of 4.2 to 4.7×10^{-4} . We have adopted 3.2×10^{-4} but the variation in the literature suggests that we test the dependence of the ion columns on the gas phase abundance of elemental O. Assuming an abundance of 4.5×10^{-4} , an increase of 40% over our standard rate, increases the columns of OH^+ , H_2O^+ , and H_3O^+ by 10-20%. Therefore, the slight possible variations in these rate coefficients and/or the gas phase elemental O abundance have a negligible effect on our conclusions.

We have also tested our results for their sensitivity to the H_2 formation rate coefficient for formation on grain surfaces. We find that lowering this rate by a factor of 3 hardly affects the results for high density gas, and that the effect is most pronounced at low density. At $n = 100 \text{ cm}^{-3}$, lowering the H_2 formation rate by 3 lowers the columns of OH^+ and H_2O^+ by factors of less than 2 in both peaks. The H_3O^+ column in both peaks decreases by a bit less than a factor of 3. The main effect of lowering the H_2 rate coefficient is to drive the H/ H_2 transition deeper into the cloud, which moves the first peaks of the ions to greater depths, but their columns and peak abundances do not change appreciably.

In the text we discussed the effect of lowering the gas phase abundance of low ionization potential metal atoms such as S, Fe, Mg, and Si if PAHs are not present. Here, we examine the effect of raising their abundances. Our standard gas phase abundances for these species are given in Table 2 of Appendix A. In our test cases, we raise the gas phase abundances of these species to 10^{-5} , a factor of 10-100 times their standard values. For our standard case of $n = 10^4 \text{ cm}^{-3}$ and $\zeta_{\text{crp}} = 2 \times 10^{-16} \text{ s}^{-1}$, but with no PAHs, this raises the electron abundance at high A_V in the gas from about 10^{-6} to about 10^{-5} . This rise depresses the (second) peak abundance of H_3O^+ from about 10^{-9} to about 10^{-10} if the photodesorption yields of Fe, Mg, and Si are 10^{-3} , a likely upper limit (H09). Smaller yields lower the electron abundance, thereby changing the H_3O^+ less. However, if PAHs are present, metal ions recombine with PAH^- and PAH, which is a much faster process than with electrons. Hence, the electron abundance does not depend much on the metal abundances. Consequently, the (second) peak H_3O^+ abundance does not change significantly. The first peaks of the ions are not affected, because the electrons are supplied by C^+ , whose gas phase abundance is more than 10 times the (high) abundance of the metal ions.

Section 4 discusses observations that indicate $N(\text{H}_3\text{O}^+) \gtrsim 10^{14} \text{ cm}^{-2}$ in some clouds, possibly even as high as 10^{16} cm^{-2} . The only way our models can accommodate very large columns of H_3O^+ in a single cloud is if there is incomplete freeze-out of water ice on grains. Note that our models are steady state, so that time dependent effects might leave more elemental oxygen in the gas phase than steady state results would indicate. Another possibility is that the grains are sufficiently warm,

$\gtrsim 100$ K, to thermally evaporate water ice off the grains, or that cosmic ray rates are sufficiently high to desorb the ice mantles. We have run our code fixing the grain temperature to be > 110 K, so that water ice cannot form and elemental oxygen is plentiful in the gas phase at all A_V . In the case of PAHs, and for our standard case of $n = 10^4 \text{ cm}^{-3}$ and $\zeta_{crp} = 2 \times 10^{-16} \text{ s}^{-1}$, we find that $x(\text{H}_3\text{O}^+)$ plateaus at a value of about 2×10^{-8} at about $A_V \sim 6$, and stays constant at that value for all higher A_V . (Note that given the discussion in §3.1, this result is independent of ζ_{crp} and n). Therefore, a cloud with a hydrogen nucleus column of 10^{23} cm^{-2} would have $N(\text{H}_3\text{O}^+) \sim 2 \times 10^{15} \text{ cm}^{-2}$, for example. Without PAHs, and assuming the low ionization potential metal atoms strongly deplete on grains, we would predict similar columns.

REFERENCES

- Aalto, S., Costagliola, F., van der Tak, F., & Meijerink, R. 2011, *A&A*, 527, A69
- Badnell, N. R., et al. 2003, *A&A*, 406, 1151
- Badnell, N. R. 2006, *ApJS*, 167, 334
- Bakes, E. L. O., & Tielens, A. G. G. M. 1998, *ApJ*, 499, 258
- Benz, A. O., Bruderer, S., van Dishoeck, E. F., et al. 2010, *A&A*, 521, L35
- Black, J. H., & Dalgarno, A. 1973, *ApJ*, 184, L101
- Boulanger, F., Falgarone, E., Puget, J. L., & Helou, G. 1990, *ApJ*, 364, 136
- Brian, J., & Mitchell, A. 1990, *Phys. Rep.* 186, 215
- Bruderer, S., Benz, A. O., van Dishoeck, E. F., et al. 2010, *A&A*, 521, L44
- Cartledge, S. I. B., Lauroesch, J. T., Meyer, D. M., & Sofia, U. J. 2004, *ApJ*, 613, 1037
- Corbel, S., & Eikenberry, S. S. 2004, *A&A*, 419, 191
- Dalgarno, A., Yan, M., & Liu, W. 1999, *ApJS*, 125, 237
- Draine, B. T. 1978, *ApJS*, 36, 595
- Draine, B. T., & Katz, N. 1986, *ApJ*, 310, 392
- Draine, B. T., & Li, A. 2007, *ApJ*, 657, 810
- Draine, B. T., & Sutin, B. 1987, *ApJ*, 320, 803
- Elitzur, M., & Watson, W. D. 1978, *ApJ*, 222, L141
- Falgarone, E., Godard, B., Cernicharo, J., et al. 2010, *A&A*, 521, L15
- Falgarone, E., Ossenkopf, V., Gerin, M., et al. 2010, *A&A*, 518, L118
- Flower, D. R., & Pineau des Forets, G. 1998, *MNRAS*, 297, 1182
- Flower, D. R., & Pineau des Forêts, G. 2003, *MNRAS*, 343, 390
- Gerin, M., de Luca, M., Black, J., et al. 2010, *A&A*, 518, L110
- Godard, B., Falgarone, E., Gerin, M., et al. 2012, [arXiv:1201.5457](https://arxiv.org/abs/1201.5457)
- Godard, B., Falgarone, E., & Pineau Des Forêts, G. 2009, *A&A*, 495, 847
- Godard, B., Falgarone, E., Gerin, M., Hily-Blant, P., & de Luca, M. 2010, *A&A*, 520, A20

- Goicoechea, J. R., & Cernicharo, J. 2001, *ApJ*, 554, L213
- Goicoechea, J. R., Rodríguez-Fernández, N. J., & Cernicharo, J. 2004, *ApJ*, 600, 214
- Goicoechea, J. R., & Le Bourlot, J. 2007, *A&A*, 467, 1
- González-Alfonso, E., Fischer, J., Isaak, K., et al. 2010, *A&A*, 518, L43
- Gupta, H., Rimmer, P., Pearson, J. C., et al. 2010, *A&A*, 521, L47
- Habing, H. J. 1968, *Bull. Astron. Inst. Netherlands*, 19, 421
- Heiles, C., & Troland, T. H. 2003, *ApJ*, 586, 1067
- Heiles, C., & Troland, T. H. 2005, *ApJ*, 624, 773
- Hollenbach, D., Kaufman, M. J., Bergin, E. A., & Melnick, G. J. 2009, *ApJ*, 690, 1497 (H09)
- Indriolo, N., Geballe, T. R., Oka, T., & McCall, B. J. 2007, *ApJ*, 671, 1736
- Indriolo, N., Geballe, T. R., Oka, T., & McCall, B. J. 2011, 66th International Symposium On Molecular Spectroscopy,
- Indriolo, N., Neufeld, D.A., Gerin, M., Geballe, T. R., Black, J. H., Menten, K. M., & Goicoechea, J. R. 2012, *ApJ*, submitted
- Jensen, M. J., Bilodeau, R. C., Safvan, C. P., Seiersen, K., Andersen, L. H., Pedersen, H. B., & Heber, O. 2000, *ApJ*, 543, 764
- Jensen, A. G., Rachford, B. L., & Snow, T. P. 2005, *ApJ*, 619, 891
- Jochims, H. W., Baumgaertel, H., & Leach, S. 1996, *A&A*, 314, 1003
- Joulain, K., Falgarone, E., Pineau des Forets, G., & Flower, D. 1998, *A&A*, 340, 241
- Klippenstein, S.J., Georgievskii, Y., & McCall, B.J. 2010, *J. Phys. Chem.*, 114, 278
- Krelowski, J., Beletsky, Y., & Galazutdinov, G. A. 2010, *ApJ*, 719, L20
- Le Petit, F., Nehmé, C., Le Bourlot, J., & Roueff, E. 2006, *ApJS*, 164, 506
- Lepp, S., & Dalgarno, A. 1988, *ApJ*, 324, 553
- Lesaffre, P., Gerin, M., & Hennebelle, P. 2007, *A&A*, 469, 949
- Liszt, H. 2003, *A&A*, 398, 621
- Liszt, H. S. 2007, *A&A*, 461, 205
- Malloci, G., Joblin, C., & Mulas, G. 2007, *Chemical Physics*, 332, 353

- Mathis, J. S., Mezger, P. G., & Panagia, N. 1983, *A&A*, 128, 212
- McCall, B. J., et al. 2004, *Phys. Rev. A*, 70, e052716
- Meyer, D. M., Jura, M., & Cardelli, J. A. 1998, *ApJ*, 493, 222
- Millar, T. J., Herbst, E., & Charnley, S. B. 1991, *ApJ*, 369, 147
- Neau, A., et al. 2000, *J. Chem. Phys.*, 113, 1762
- Neufeld, D. A., Goicoechea, J. R., Sonnentrucker, P., et al. 2010, *A&A*, 521, L10 (N10)
- Neufeld, D., Hollenbach, D., Kaufman, M., et al. 2011, *IAU Symposium*, 280,
- Öberg, K. I., van Dishoeck, E. F., & Linnartz, H. 2009, *A&A*, 496, 281
- Ossenkopf, V., Müller, H. S. P., Lis, D. C., et al. 2010, *A&A*, 518, L111
- Phillips, T. G., van Dishoeck, E. F., & Keene, J. 1992, *ApJ*, 399, 533 (PvDK92)
- Prasad, S. S., & Tarafdar, S. P. 1983, *ApJ*, 267, 603
- Rapacioli, M., Calvo, F., Joblin, C., et al. 2006, *A&A*, 460, 519
- Rimmer, P., & Herbst, E. 2011, *Mem. Soc. Astron. Italiana*, 82, 933
- Roberge, W. G., Jones, D., Lepp, S., & Dalgarno, A. 1991, *ApJS*, 77, 287
- Savage, B. D., & Sembach, K. R. 1996, *ARA&A*, 34, 279
- Schilke, P., Comito, C., Müller, H. S. P., et al. 2010, *A&A*, 521, L11
- Sofia, U. J., Lauroesch, J. T., Meyer, D. M., & Cartledge, S. I. B. 2004, *ApJ*, 605, 272
- Stancil, P. C., Schultz, D. R., Kimura, M., et al. 1999, *A&AS*, 140, 225
- Tielens, A. G. G. M., & Hollenbach, D. 1985, *ApJ*, 291, 722
- van der Tak, F. F. S., Aalto, S., & Meijerink, R. 2008, *A&A*, 477, L5
- van der Tak, F. F. S., Belloche, A., Schilke, P., et al. 2006, *A&A*, 454, L99
- van der Werf, P. P., Isaak, K. G., Meijerink, R., et al. 2010, *A&A*, 518, L42
- van Dishoeck, E. F. 1988, in *Rate Coefficients in Astrochemistry*, eds. T.J. Millar & D. A. Williams (Dordrecht: Kluwer), p.49
- van Dishoeck, E. F., & Black, J. H. 1986, *ApJS*, 62, 109
- van Dishoeck, E. F., Jonkheid, B. van Hemert, M. C. 2006, *Faraday Discussions*, 2006, 133, 231

- Visser, R., van Dishoeck, E. F., & Black, J. H. 2009, *A&A*, 503, 323
- Weingartner, J. C., & Draine, B. T. 2001a, *ApJ*, 563, 842
- Weingartner, J. C., & Draine, B. T. 2001b, *ApJ*, 553, 581
- Weiß, A., Requena-Torres, M. A., Güsten, R., et al. 2010, *A&A*, 521, L1
- Wolfire, M. G., McKee, C. F., Hollenbach, D., & Tielens, A. G. G. M. 2003, *ApJ*, 587, 278
- Wolfire, M. G., Tielens, A. G. G. M., Hollenbach, D., & Kaufman, M. J. 2008, *ApJ*, 680, 384
- Wootten, A., Mangum, J. G., Turner, B. E., et al. 1991, *ApJ*, 380, L79
- Wyrowski, F., Menten, K. M., Güsten, R., & Belloche, A. 2010, *A&A*, 518, A26
- Wyrowski, F., van der Tak, F., Herpin, F., et al. 2010, *A&A*, 521, L34

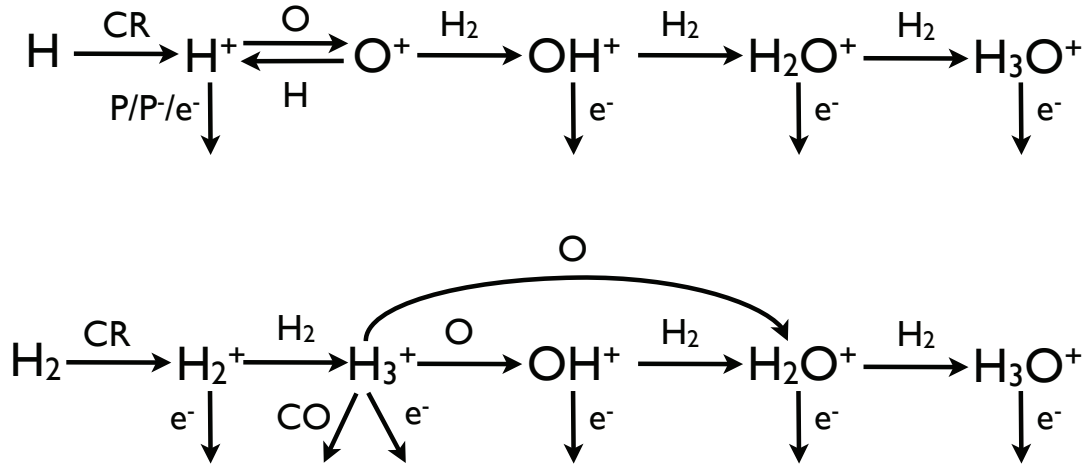


Fig. 1.— Standard ion-neutral chemistry leading to the formation of OH^+ , H_2O^+ , and H_3O^+ in clouds via ionization of atomic H (top panel), and via ionization of molecular H_2 (bottom panel). In the top panel, the destruction of H^+ labelled "P/P⁻/e⁻" means the neutralization of H^+ by reacting with PAHs, PAH⁻s, or electrons. "CR" means cosmic ray ionization.

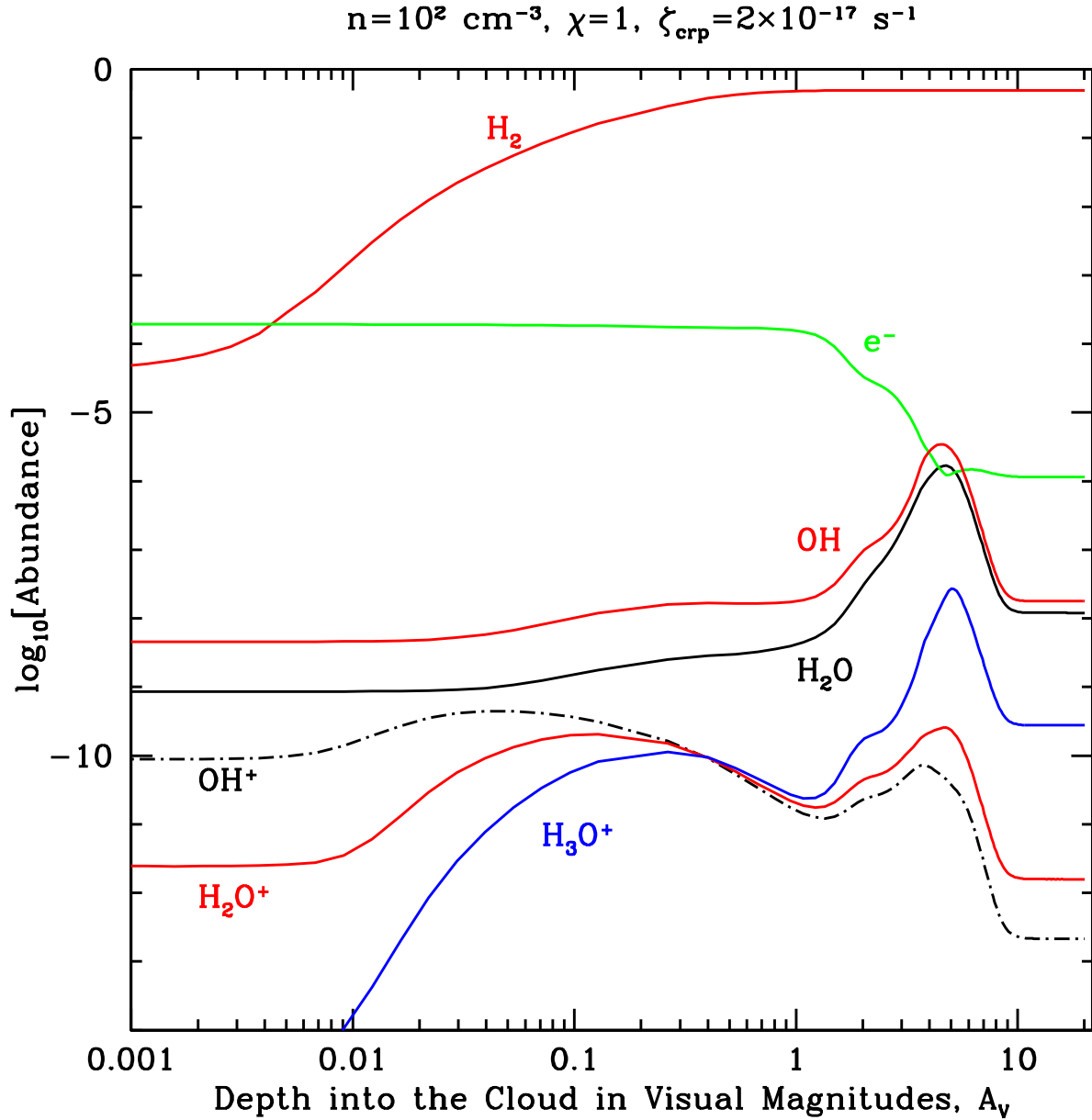


Fig. 2.— The variation of gas phase abundances of species as a function of depth A_V into a cloud for the standard case $n = 100 \text{ cm}^{-3}$, $\chi = 1$, and $\zeta_{\text{crp}} = 2 \times 10^{-17} \text{ s}^{-1}$. To convert A_V to hydrogen nucleus column N , use $N = 2 \times 10^{21} A_V \text{ cm}^{-2}$. This case probes diffuse cloud-like condition to high A_V , or could apply to low density surfaces of GMCs experiencing the local interstellar radiation field. Note these are columns when the cloud is viewed face-on. Color versions of the figures available in the on-line manuscript

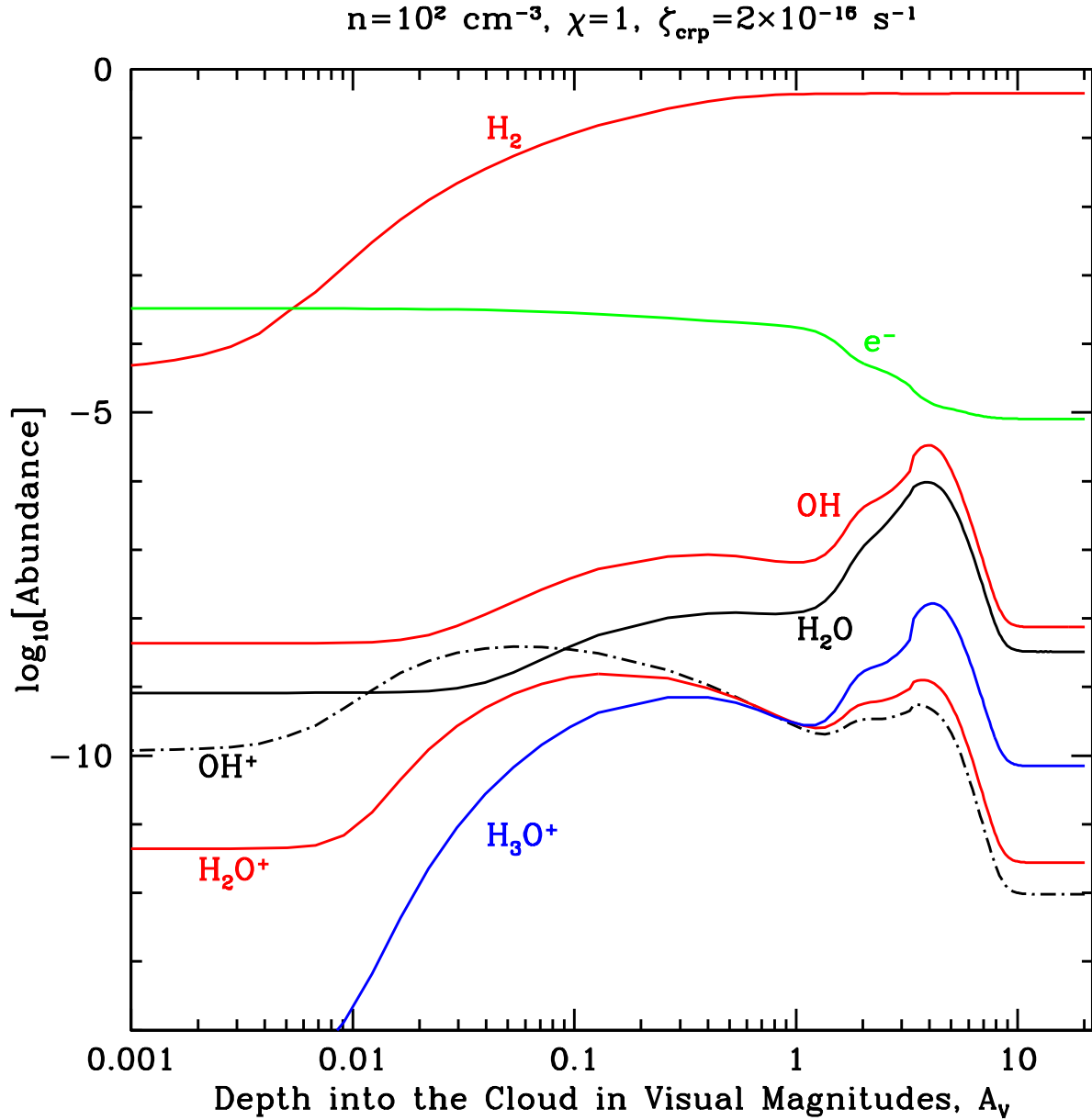


Fig. 3.— The variation of gas phase abundances of species as a function of depth A_V for the standard case $n = 100 \text{ cm}^{-3}$, $\chi = 1$, and $\zeta_{\text{crp}} = 2 \times 10^{-16} \text{ s}^{-1}$. This is the same case as Figure 2 but with 10 times the cosmic ray ionization rate. This case probes diffuse cloud-like condition to high A_V , or could apply to low density surfaces of GMCs experiencing the local interstellar radiation field.

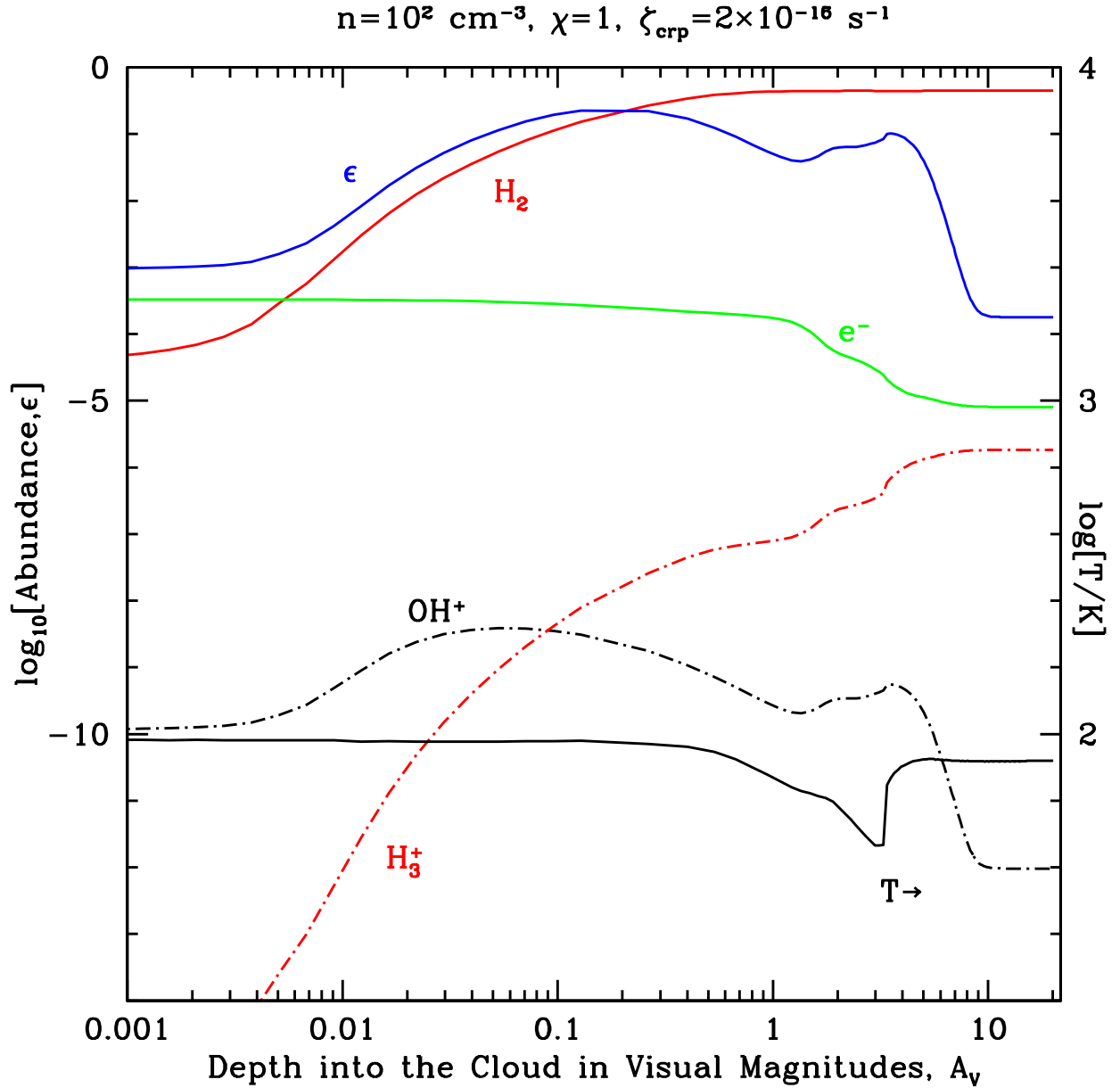


Fig. 4.— The variation of the parameter ϵ , the ratio of the rate of OH^+ formation to the cosmic ray ionization rate of H and H_2 , the gas temperature T (labelled on right), and the gas phase abundances of electrons, H_2 , H_3^+ , and OH^+ as a function of depth A_V for the case $n = 100 \text{ cm}^{-3}$, $\chi = 1$, and $\zeta_{\text{crp}} = 2 \times 10^{-16} \text{ s}^{-1}$. This case probes diffuse cloud-like condition to high A_V , or could apply to low density surfaces of GMCs experiencing the local interstellar radiation field. This is the same case as the previous figure.

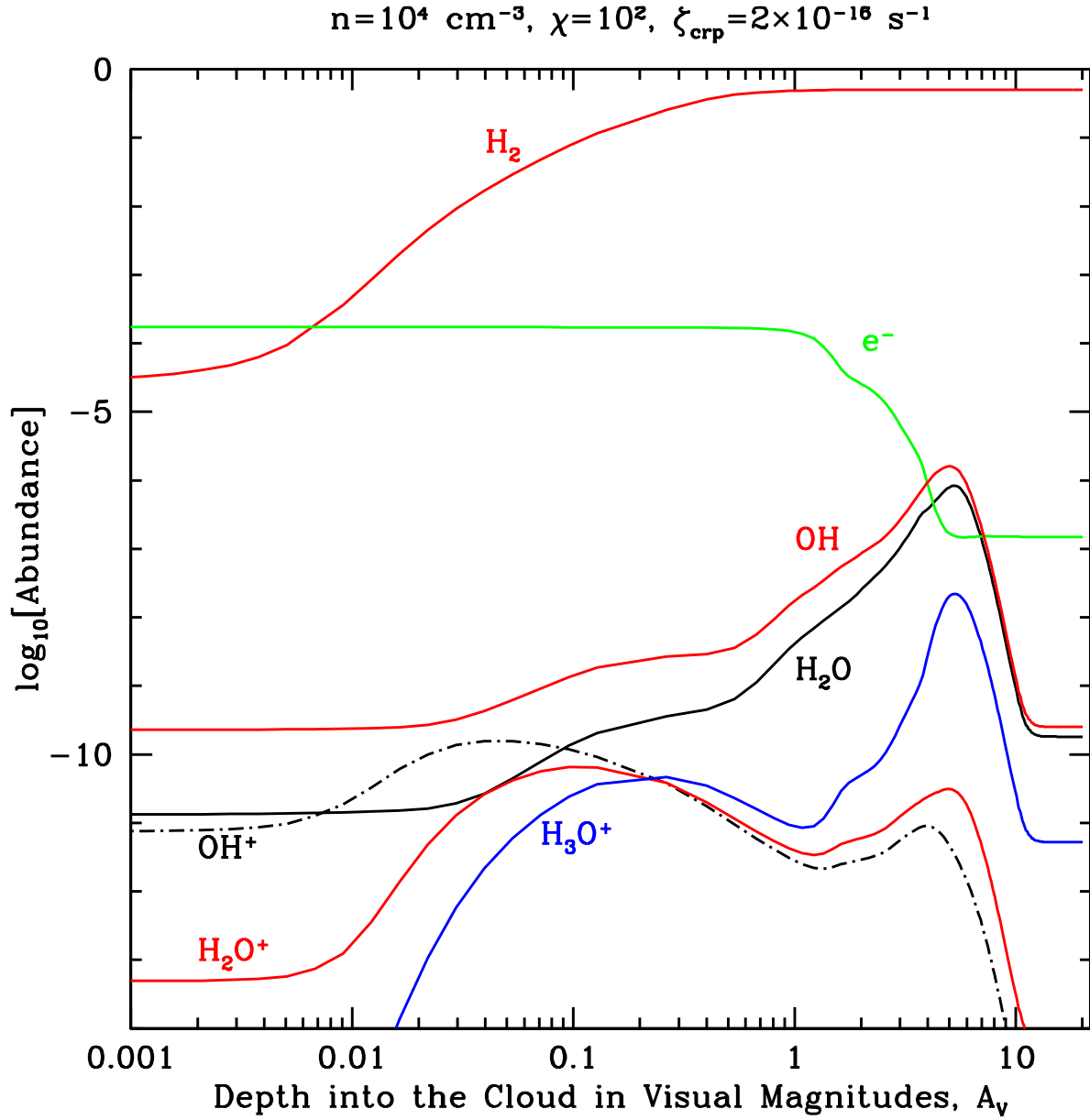


Fig. 5.— The variation of gas phase abundances of species as a function of depth A_V into the cloud for the standard case $n = 10^4 \text{ cm}^{-3}$, $\chi = 100$, and $\zeta_{\text{crp}} = 2 \times 10^{-16} \text{ s}^{-1}$. This case may be appropriate to GMCs with elevated FUV fluxes incident due to nearby O and B stars.

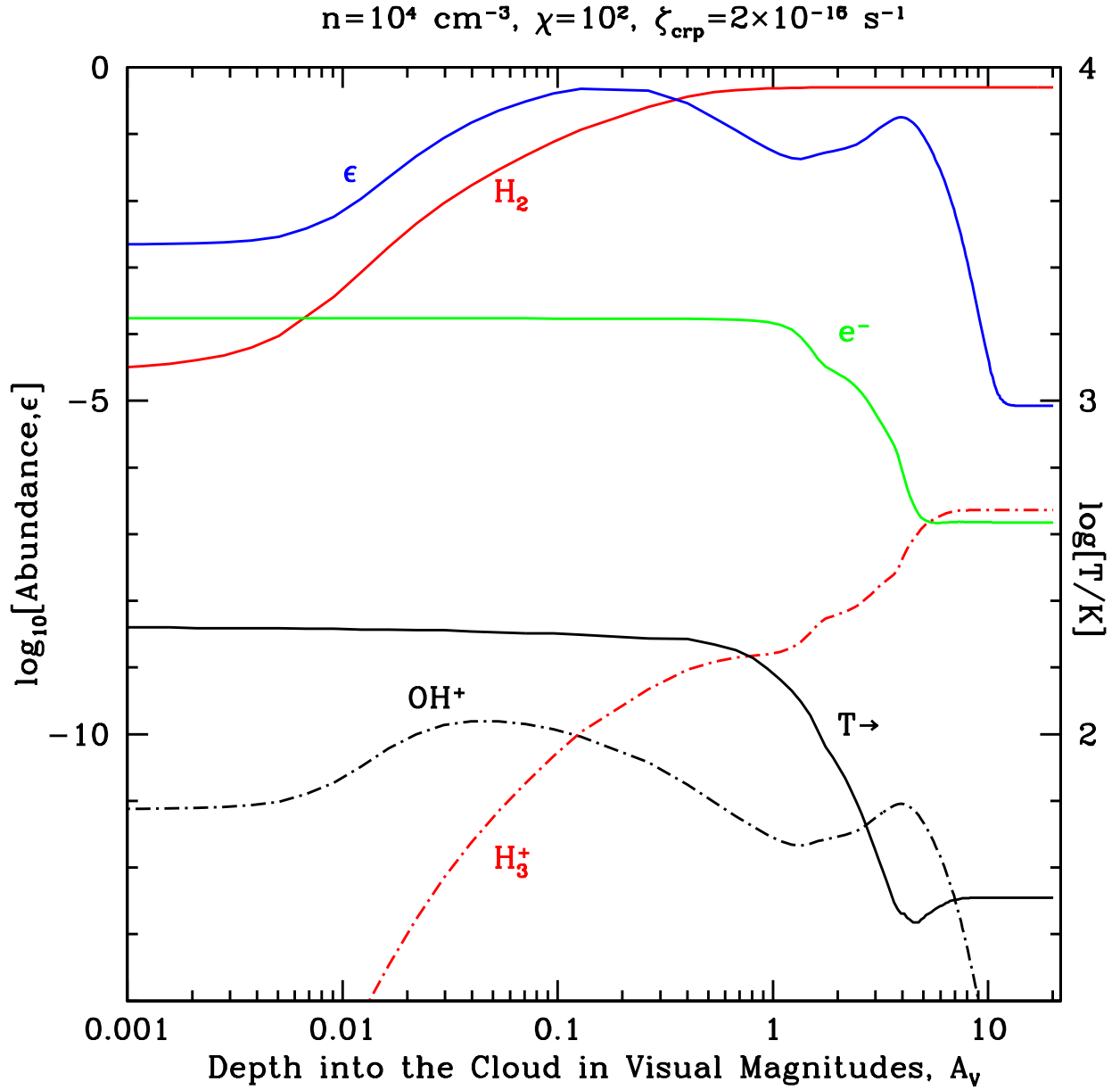


Fig. 6.— The variation of the parameter ϵ , the ratio of the rate of OH^+ formation to the cosmic ray ionization rate of H and H_2 , the gas temperature T (labelled on right), and the gas phase abundances of electrons, H_2 , H_3^+ , and OH^+ as a function of depth A_V for the case $n = 10^4 \text{ cm}^{-3}$, $\chi = 100$, and $\zeta_{\text{crp}} = 2 \times 10^{-16} \text{ s}^{-1}$. This is the same case as the previous figure.

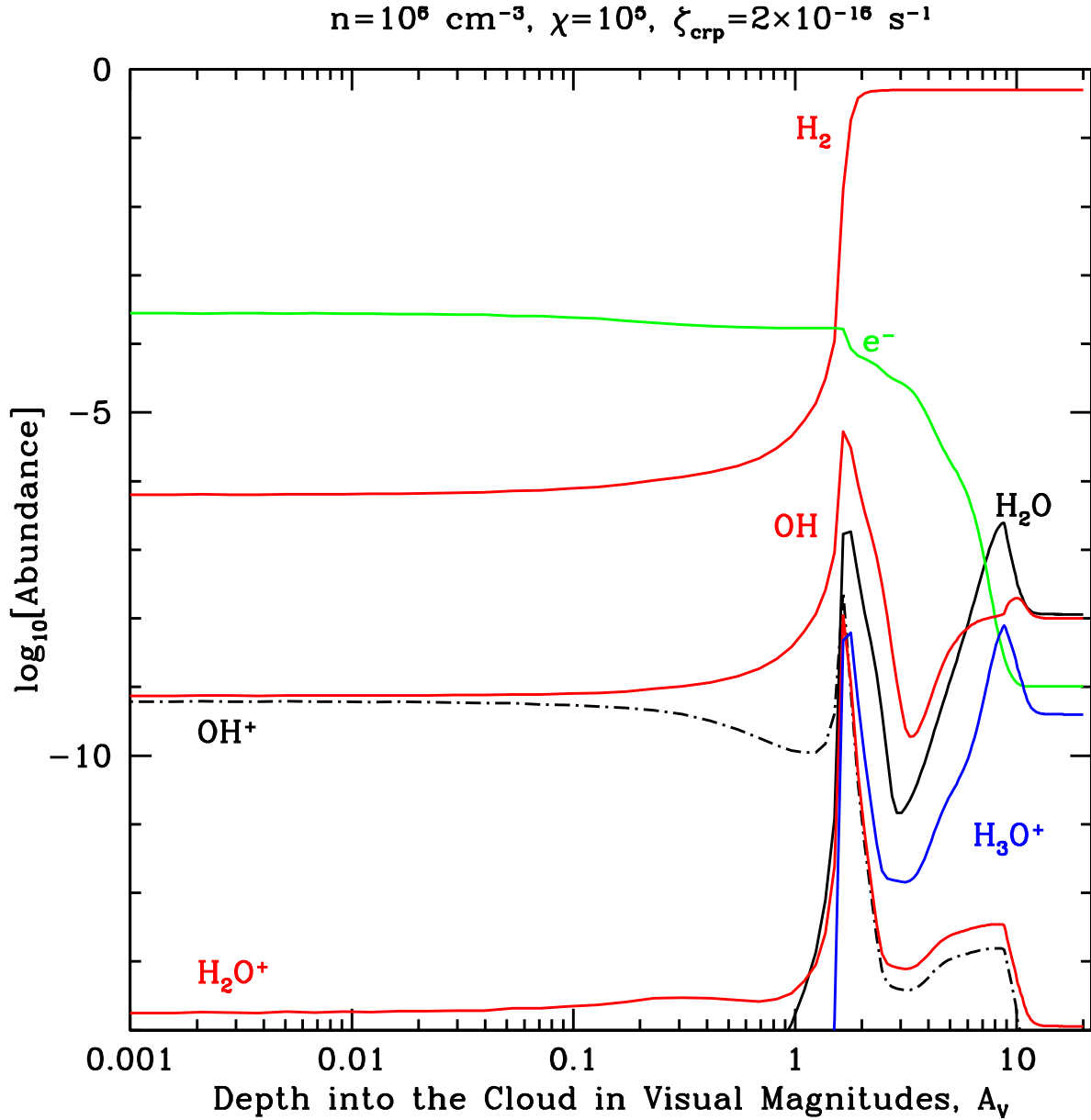


Fig. 7.— The variation of gas phase abundances of species as a function of depth A_V for the case $n = 10^6 \text{ cm}^{-3}$, $\chi = 10^5$, and $\zeta_{\text{crp}} = 2 \times 10^{-16} \text{ s}^{-1}$. This case demonstrates the structure of PDRs with both high density and high FUV fluxes, where elevated ($> 300 \text{ K}$) temperatures in the region with significant H_2 leads to the enhanced production of H^+ by chemical routes not initiated by cosmic ray ionization (see text). One mark of this is the enhanced OH abundance, produced by the neutral-neutral reaction of H_2 with O that is seen at $A_V \sim 1$, where the gas temperature is $T \sim 1000 \text{ K}$. The enhanced OH reacts with C^+ to produce CO^+ , which then reacts with H to form H^+ . The rest of the chemistry leading to OH^+ , H_2O^+ , and H_3O^+ is seen in Figure 1.

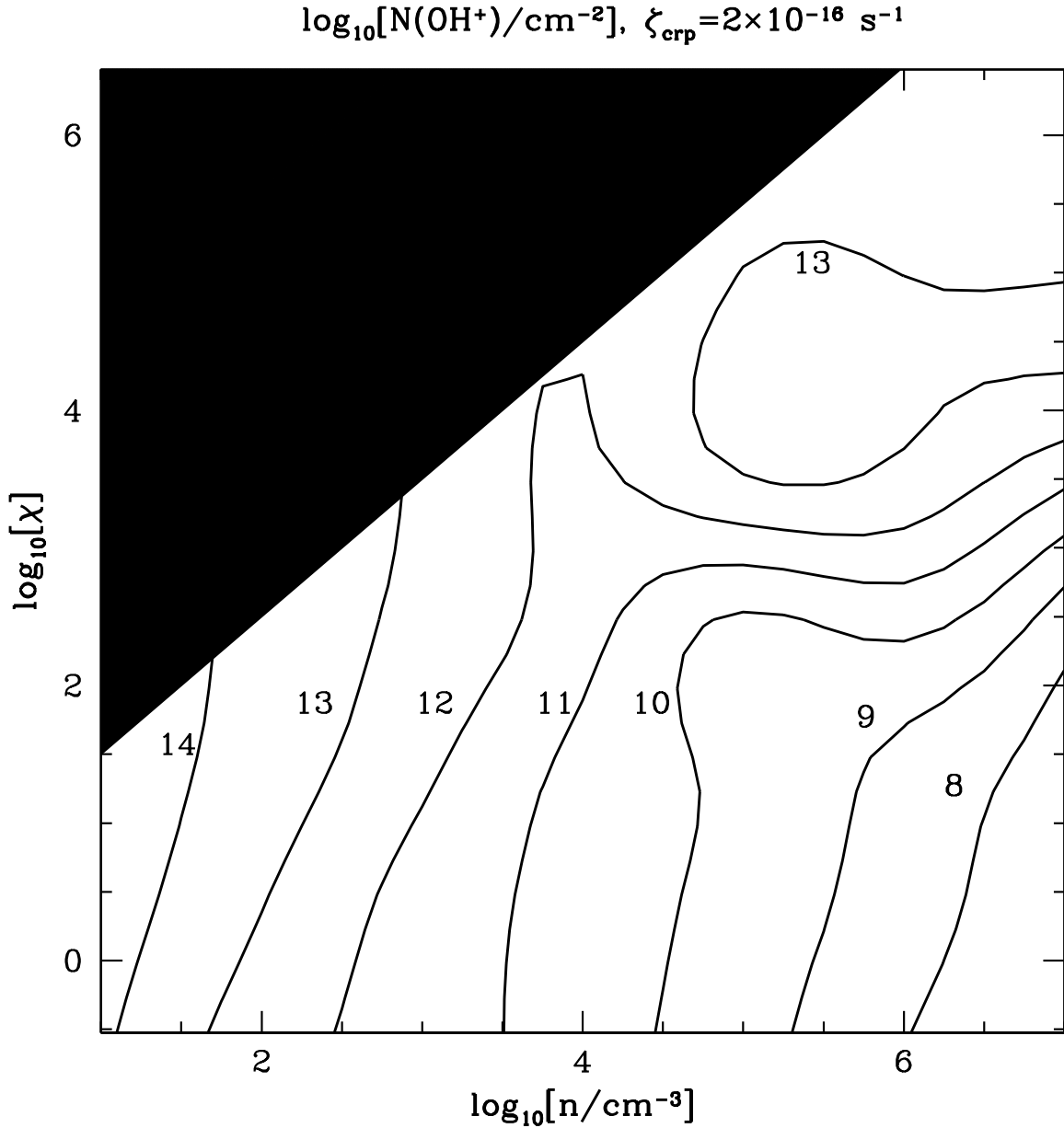


Fig. 8.— Contours of the column of OH^+ , labelled in log units, as a function of n and χ for a fixed primary cosmic ray ionization rate of $\zeta_{\text{crp}}=2 \times 10^{-16} \text{ s}^{-1}$ per H atom. The upper left portion of the figure is blacked out because radiation pressure on dust drives dust quickly through the PDR in this region, invalidating the physics assumed in the model. This combination of χ and n are rarely observed in any case. Except in the upper right hand corner of this figure (high n and high χ), we see that for fixed cosmic ray ionization rate, the column is roughly proportional to n^{-1} , and independent of χ . The upper right hand corner shows a secondary peak in the OH^+ column, caused by the alternate chemical routes described in text and shown in more detail in Figure 7. Low densities $n \lesssim 100 \text{ cm}^{-3}$ are required to obtain columns greater than about 10^{13} cm^{-2} created by cosmic rays.

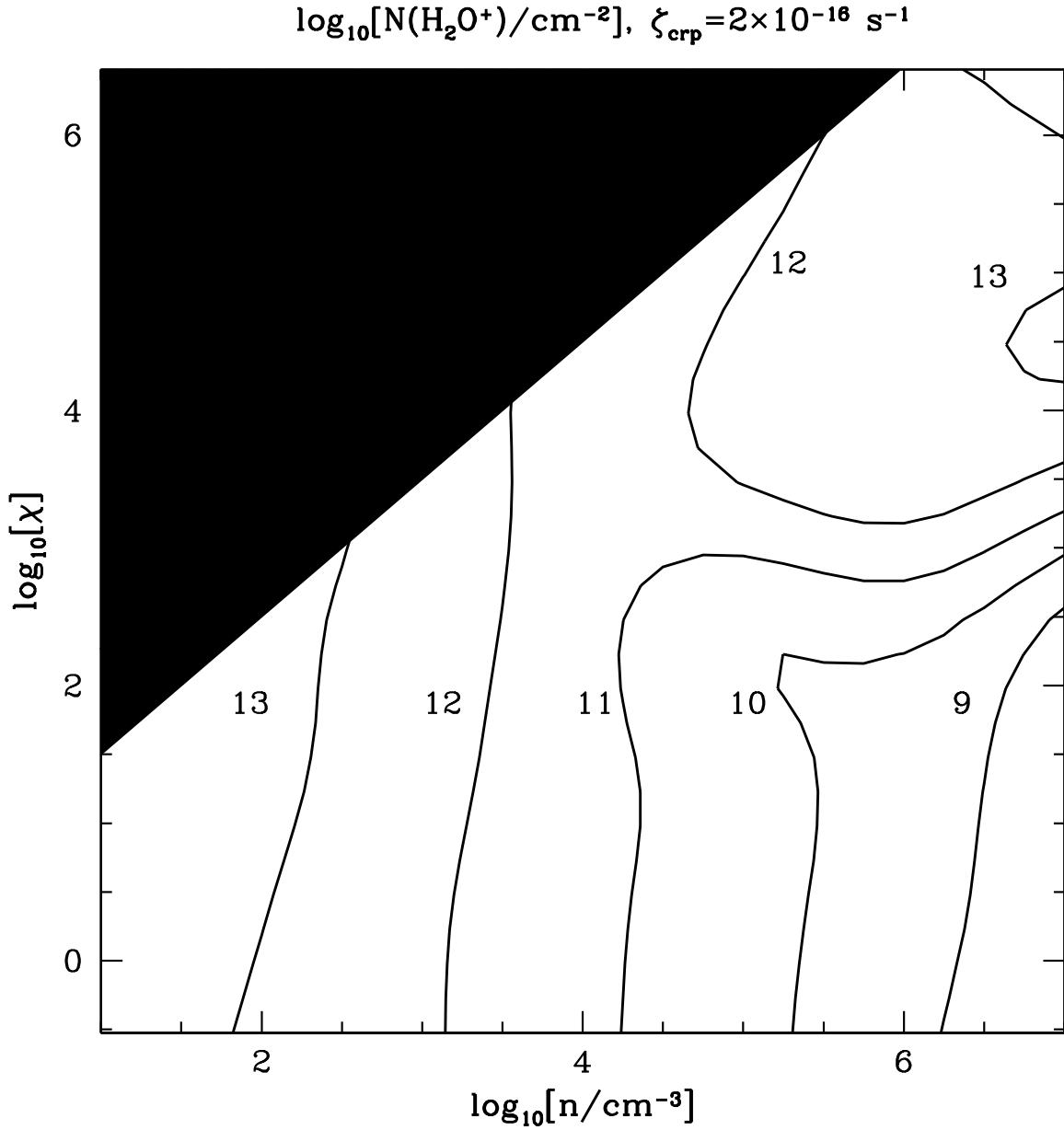


Fig. 9.— Contours of the column of H_2O^+ , labelled in log units, as a function of n and χ for a fixed primary cosmic ray ionization rate of $\zeta_{\text{crp}}=2 \times 10^{-16} \text{ s}^{-1}$ per H atom. The same discussion as in the previous figure applies here. To obtain columns greater than about 10^{13} cm^{-2} created by cosmic rays requires low densities $n \lesssim 100 \text{ cm}^{-3}$.

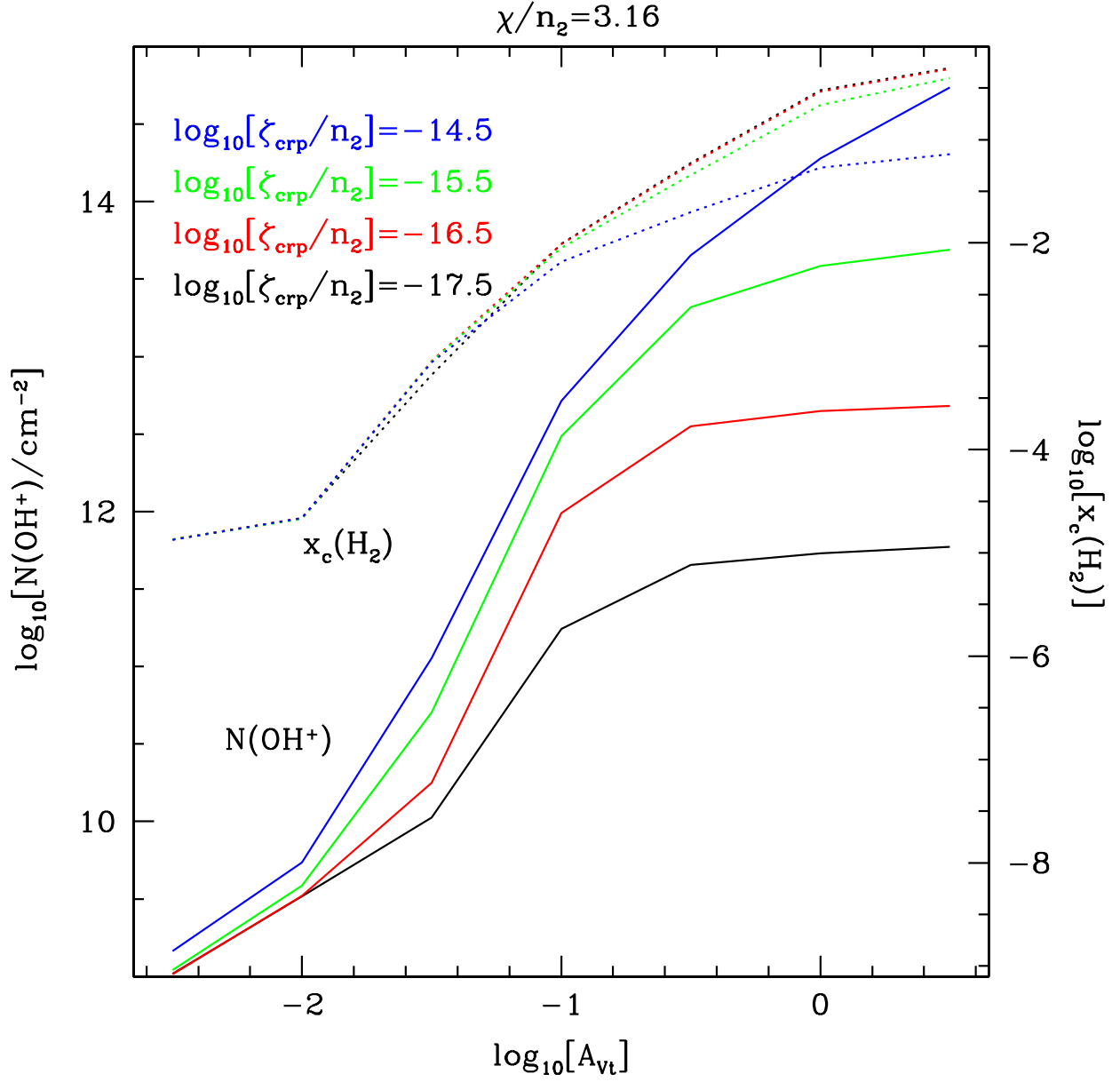


Fig. 10.— The columns of OH^+ , $N(\text{OH}^+)$, are plotted as a function of A_{Vt} for four values of the primary cosmic ray ionization rate per H atom divided by $n_2 \equiv n/100 \text{ cm}^{-3}$ and for $\chi/n_2 = 3.16$. The dotted line plots the abundance of H_2 at cloud center, and these values appear on the right of the figure. Recall A_{Vt} is the total A_V through the diffuse or translucent cloud. The H_2 abundance at cloud center, $x(\text{H}_2)$, is also plotted (dotted lines) and its values noted on the right.

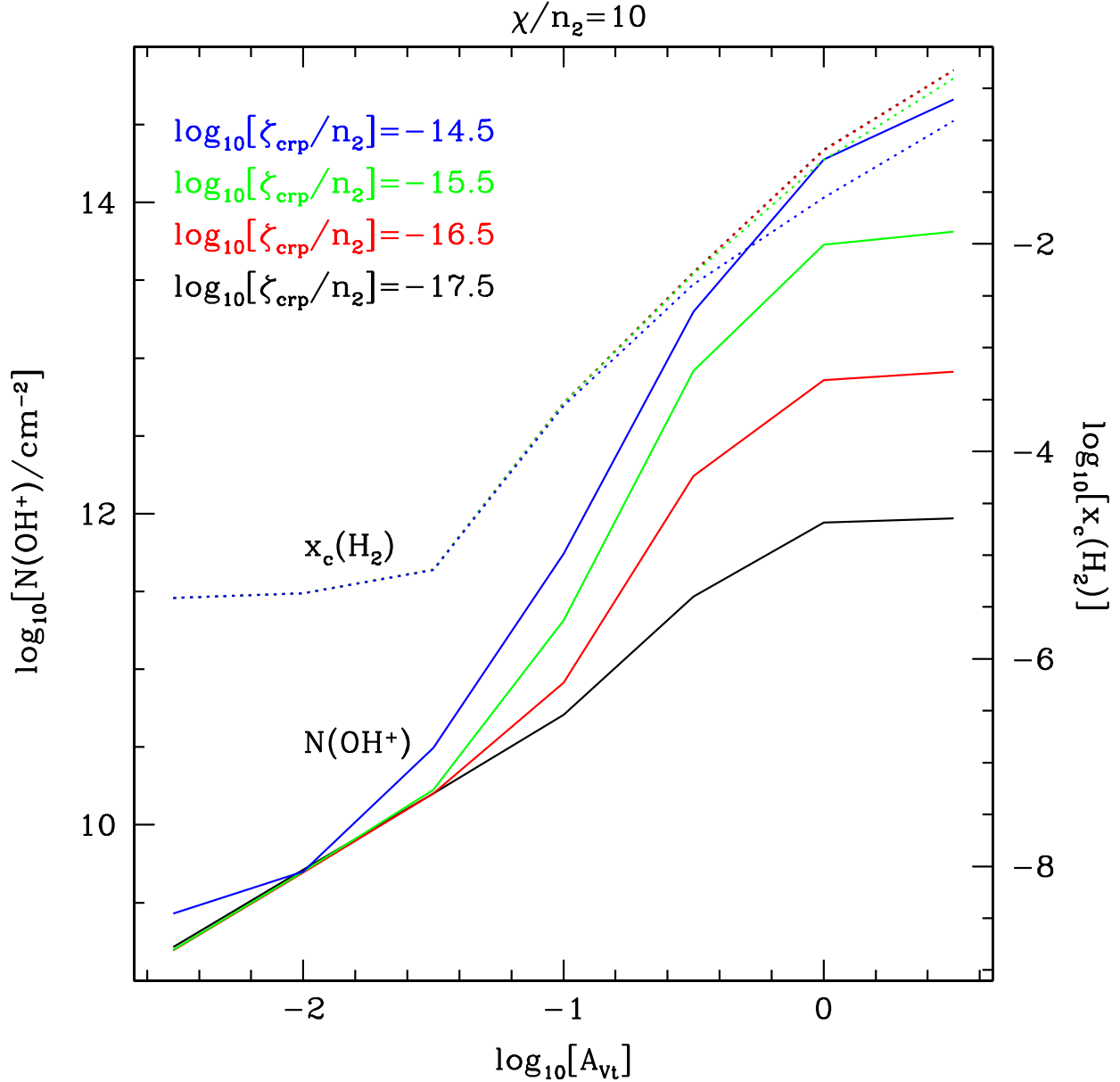


Fig. 11.— The columns of OH^+ , $N(\text{OH}^+)$, are plotted as a function of A_{Vt} for four values of the primary cosmic ray ionization rate per H atom divided by $n_2 \equiv n/100 \text{ cm}^{-3}$ and for $\chi/n_2 = 10$. The dotted line plots the abundance of H_2 at cloud center, and these values appear on the right of the figure. This figure is the same as Figure 10, only with χ/n_2 raised by 3.16.

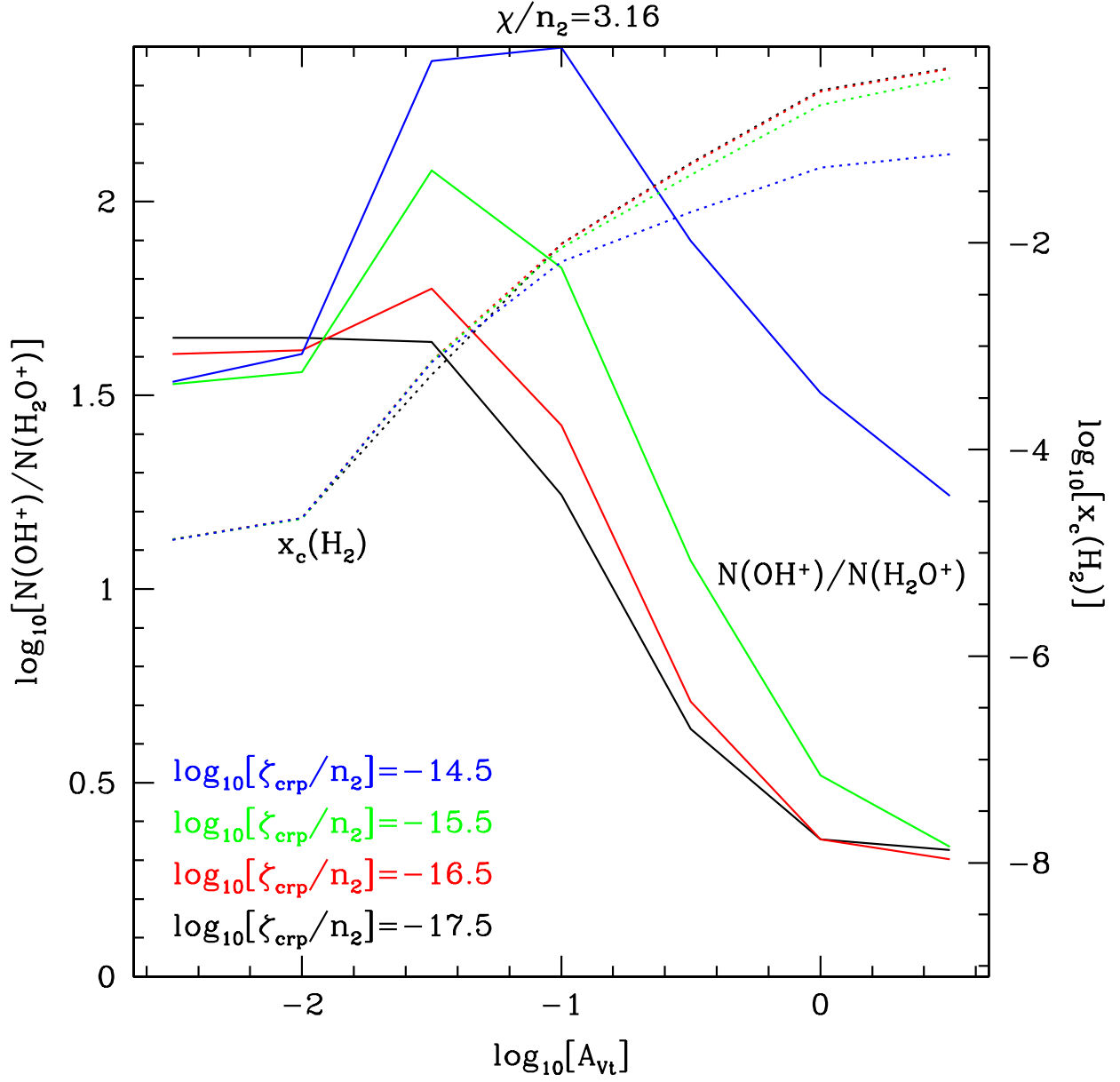


Fig. 12.— The ratio $N(\text{OH}^+)/N(\text{H}_2\text{O}^+)$ is plotted as a function of A_{Vt} for four values of the primary cosmic ray ionization rate per H atom divided by $n_2 \equiv n/100 \text{ cm}^{-3}$ and for $\chi/n_2 = 3.16$. The dotted line plots the abundance of H_2 at cloud center, and these values appear on the right of the figure.

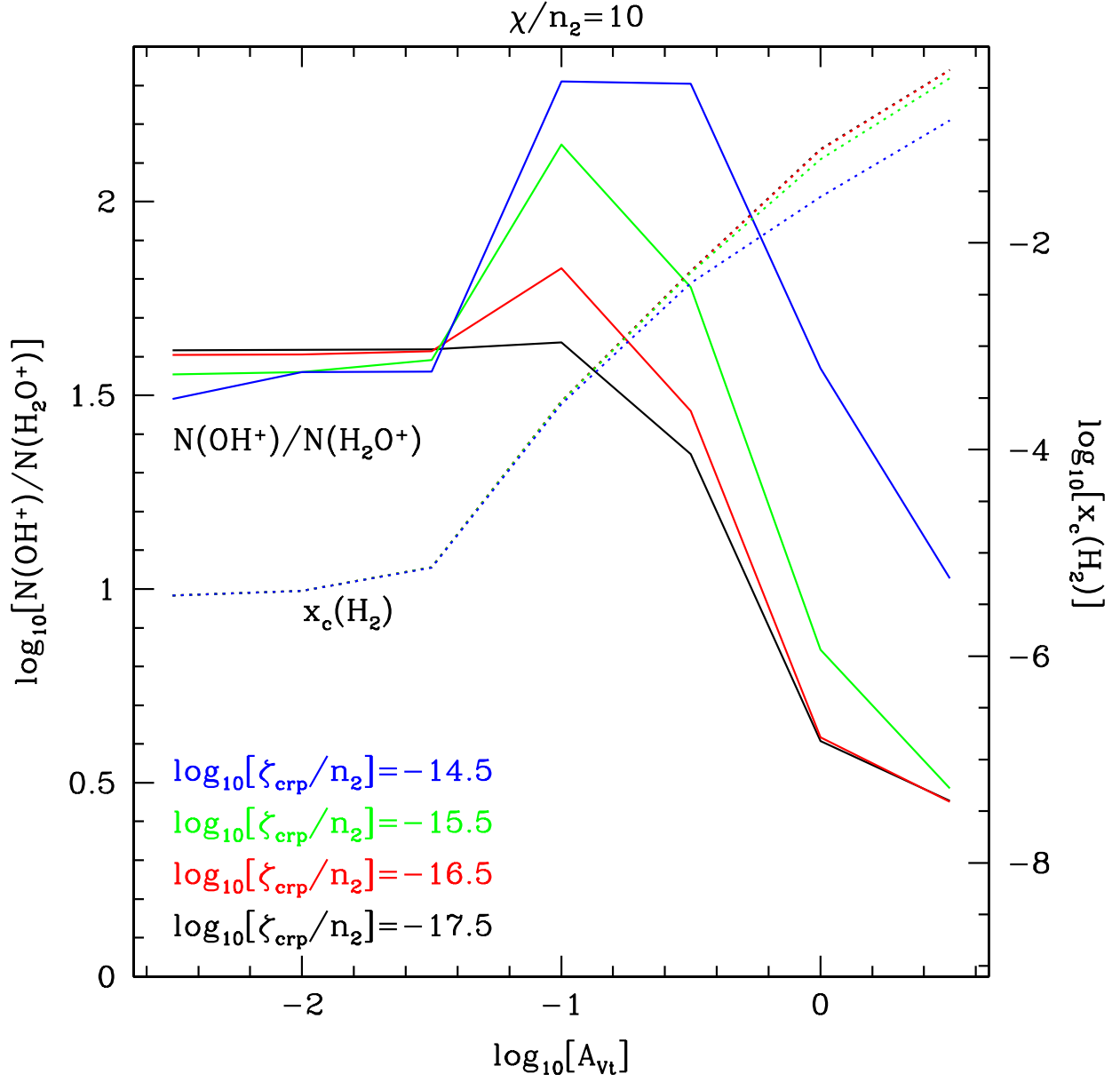


Fig. 13.— The ratio $N(\text{OH}^+)/N(\text{H}_2\text{O}^+)$ is plotted as a function of A_{Vt} for four values of the primary cosmic ray ionization rate per H atom divided by $n_2 \equiv n/100 \text{ cm}^{-3}$ and for $\chi/n_2 = 10$. The dotted line plots the fraction of H_2 in the cloud, and these values appear on the right of the figure. This figure is the same as Figure 12, only with χ/n_2 raised by 3.16.

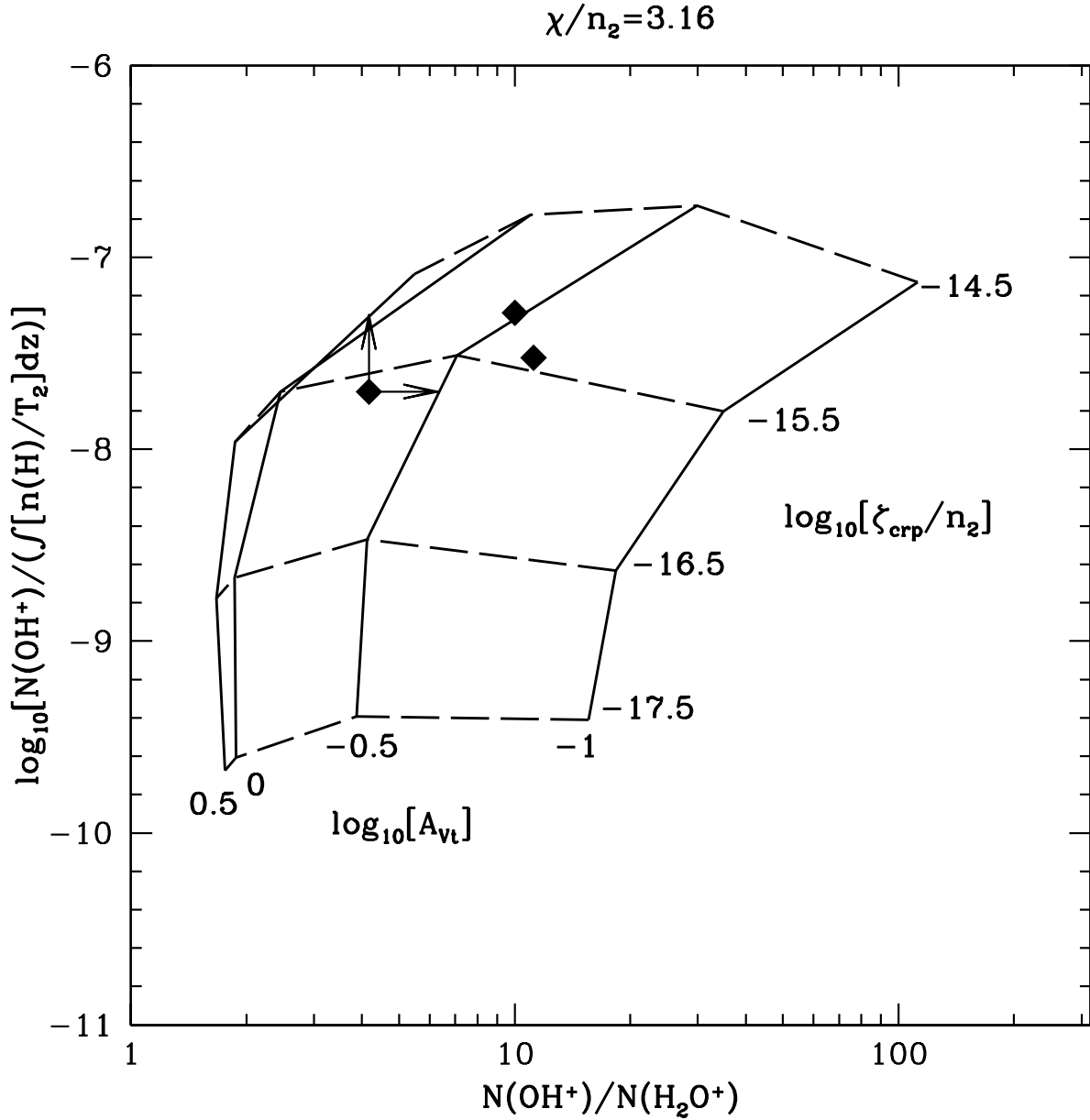


Fig. 14.— $\log_{10} [N(\text{OH}^+)/\int[n(\text{H})/T_2] dz]$ is plotted on the vertical axis and $N(\text{OH}^+)/N(\text{H}_2\text{O}^+)$ on the horizontal axis for the case $\chi/n_2 = 3.16$. Plotted as solid lines are constant values of $\log_{10}[A_{\text{vt}}]$, labelled on the bottom of these lines. Plotted as dashed lines are contours of constant $\log_{10}[\zeta_{\text{crp}}/n_2]$, labelled on the left, and in units of s^{-1} . The two data points at right are two velocity components (diffuse clouds) toward W49N. The lower limit data point is toward W31C (see text).

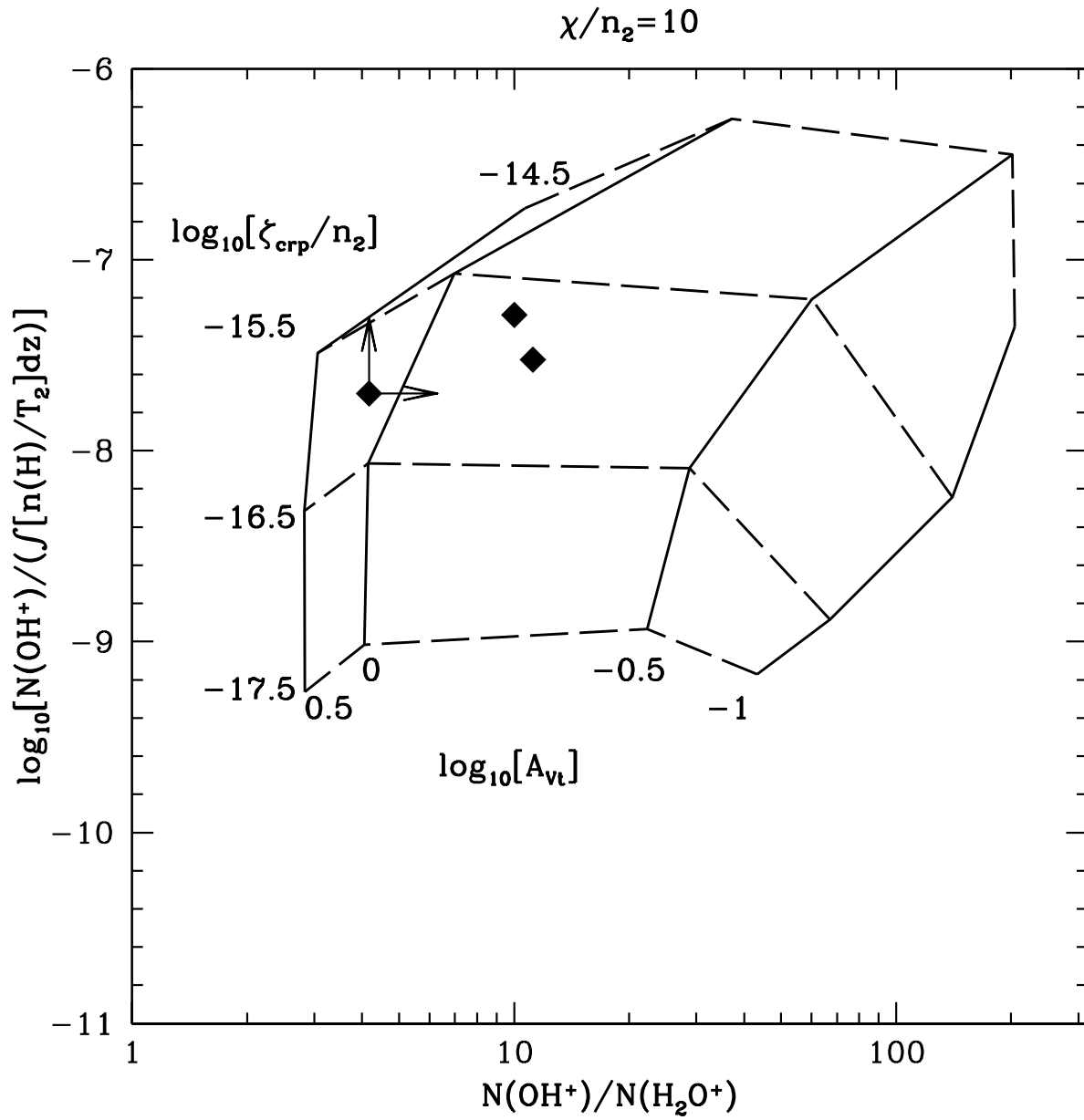


Fig. 15.— This figure is identical to Figure 14 except that $\chi/n_2 = 10$.

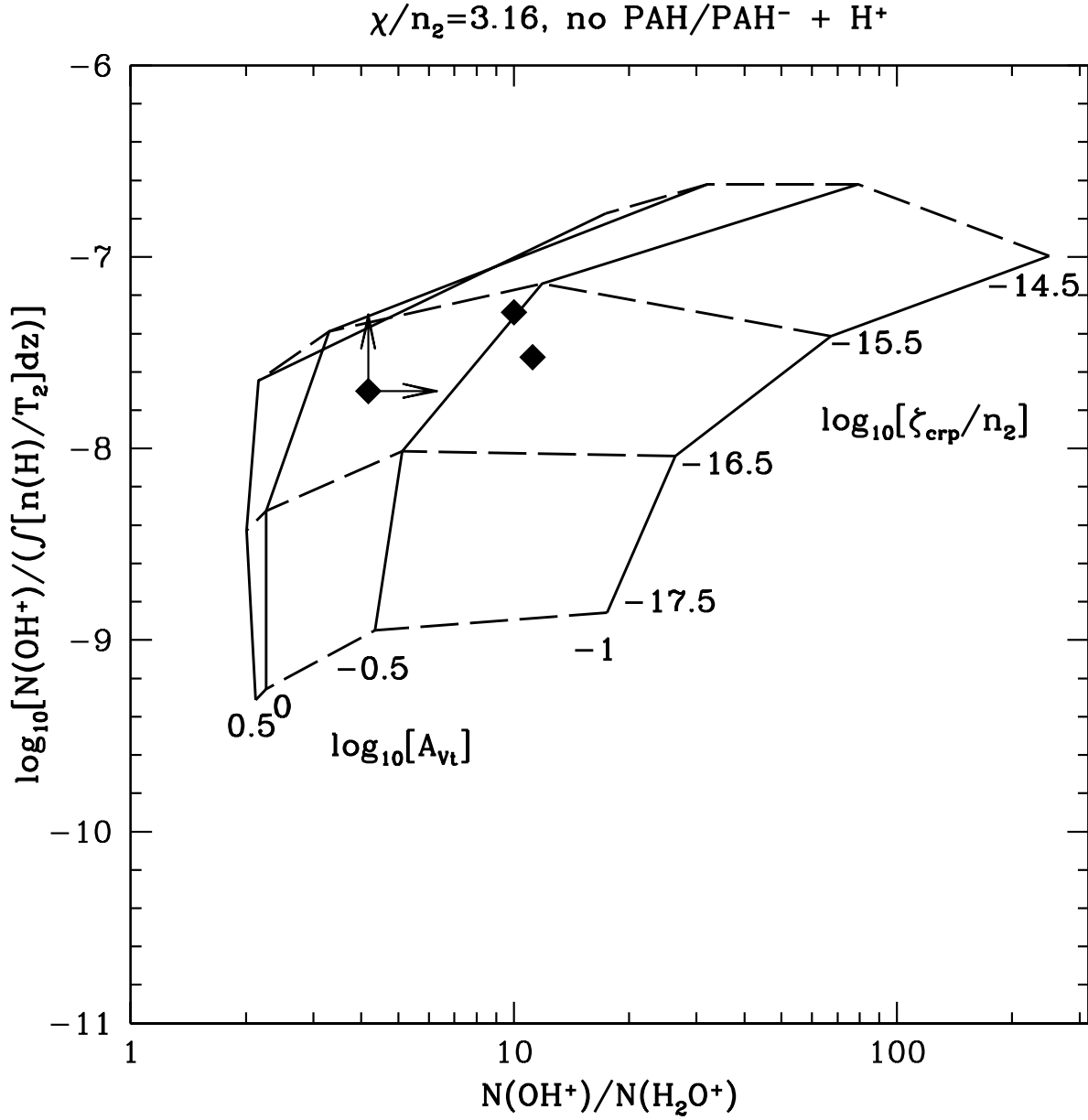


Fig. 16.— This figure is identical to Figure 14 ($\chi/n_2 = 3.16$) except that the PAH and PAH⁻ rates with H⁺ have been reduced by $\gtrsim 4$ so that H⁺ is mainly destroyed by electrons or by forming O⁺ which then reacts with H₂ to form OH⁺. Note that the inferred ζ_{crp}/n_2 values decrease compared to the case with PAHs.

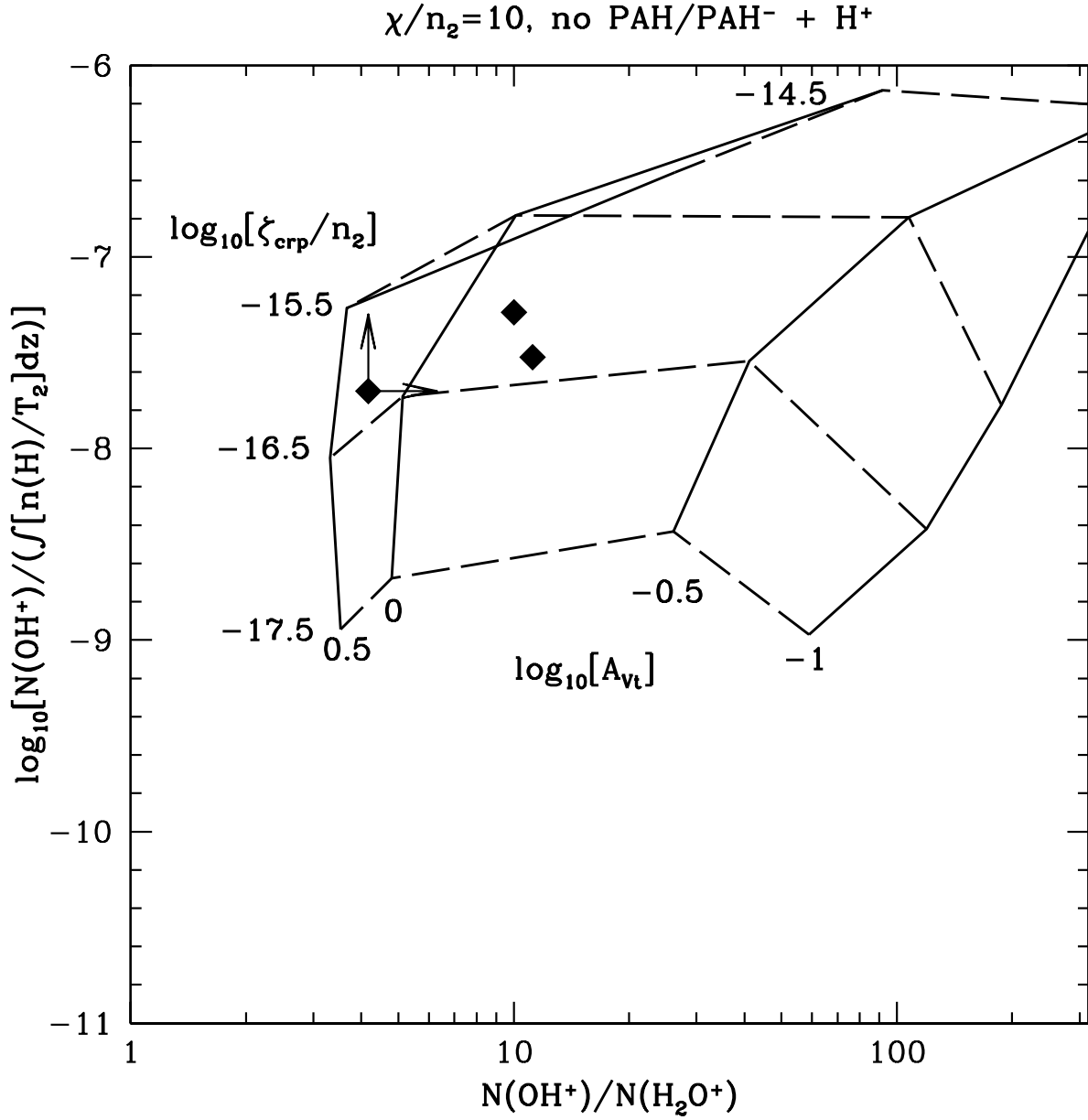


Fig. 17.— This figure is identical to Figure 15 ($\chi/n_2 = 10$) except that the PAH and PAH⁻ rates with H⁺ have been reduced by $\gtrsim 4$ so that H⁺ is mainly destroyed by electrons or by forming O⁺ which then reacts with H₂ to form OH⁺. Note that the inferred ζ_{crp}/n_2 values decrease compared to the case with PAHs.